

University of Windsor

## Scholarship at UWindor

---

Electronic Theses and Dissertations

Theses, Dissertations, and Major Papers

---

2010

# Correlation between the Microstructure of Dual Phase Steel and Industrial Tube Bending Performance

Chongzhi Chang  
*University of Windsor*

Follow this and additional works at: <https://scholar.uwindsor.ca/etd>

---

### Recommended Citation

Chang, Chongzhi, "Correlation between the Microstructure of Dual Phase Steel and Industrial Tube Bending Performance" (2010). *Electronic Theses and Dissertations*. 178.  
<https://scholar.uwindsor.ca/etd/178>

This online database contains the full-text of PhD dissertations and Masters' theses of University of Windsor students from 1954 forward. These documents are made available for personal study and research purposes only, in accordance with the Canadian Copyright Act and the Creative Commons license—CC BY-NC-ND (Attribution, Non-Commercial, No Derivative Works). Under this license, works must always be attributed to the copyright holder (original author), cannot be used for any commercial purposes, and may not be altered. Any other use would require the permission of the copyright holder. Students may inquire about withdrawing their dissertation and/or thesis from this database. For additional inquiries, please contact the repository administrator via email ([scholarship@uwindsor.ca](mailto:scholarship@uwindsor.ca)) or by telephone at 519-253-3000ext. 3208.

CORRELATION BETWEEN THE MICROSTRUCTURE OF DUAL PHASE STEEL  
AND INDUSTRIAL TUBE BENDING PERFORMANCE

by  
Chongzhi Chang

A Thesis  
Submitted to the Faculty of Graduate Studies  
through Mechanical Engineering  
in Partial Fulfillment of the Requirements for  
the Degree of Master of Applied Science  
at the University of Windsor

Windsor, Ontario, Canada

2010

© 2010 Chongzhi Chang

## **AUTHOR'S DECLARATION OF ORIGINALITY**

I hereby certify that I am the sole author of this thesis and that no part of this thesis has been published or submitted for publication.

I certify that, to the best of my knowledge, my thesis does not infringe upon anyone's copyright nor violate any proprietary rights and that any ideas, techniques, quotations, or any other material from the work of other people included in my thesis, published or otherwise, are fully acknowledged in accordance with the standard referencing practices. Furthermore, to the extent that I have included copyrighted material that surpasses the bounds of fair dealing within the meaning of the Canada Copyright Act, I certify that I have obtained a written permission from the copyright owner(s) to include such material(s) in my thesis and have included copies of such copyright clearances to my appendix.

I declare that this is a true copy of my thesis, including any final revisions, as approved by my thesis committee and the Graduate Studies office, and that this thesis has not been submitted for a higher degree to any other University or Institution.

## **ABSTRACT**

Dual phase (DP) steels, are currently one of the choice automotive materials in terms of potential for weight reduction and cost. More specifically, DP steel tubes are increasingly being used to produce automotive structural components.

In this study, tensile tests, rotary draw bending tests and microstructural analyses were conducted in order to identify which mechanical properties and microstructural features have an influence on the onset of failure in bent DP steel tubes. Several important microstructural features, such as martensite banding and non-metallic inclusions, were investigated with a view to understanding their effect on the deformation behaviour of DP steels.

The analysis of experimental data and microstructures established various correlations between DP steel properties and the onset of failure in tube bending. As a result, several empirical equations were proposed to evaluate the correlation of void area fraction and estimate the critical bending ratio of C-Mn DP steel tubes.

## **ACKNOWLEDGEMENTS**

First and foremost, I would like to sincerely thank my advisor Dr. Daniel Green for his support, advice and the opportunity to complete my Master's degree under his supervision.

I would also like to thank my committee members, Dr. Randy Bowers and Dr. William Altenhof for their patience and guidance.

Thanks are also due to Mr. Blair Longhouse and Dr. Ghafoor Khodayari at VariForm for their invaluable support throughout this project.

I would also like to thank John Robinson for his help with the preparation of samples and with the electron microscope.

Finally, particular appreciation is expressed to Chad Oliver, Honggang An, Qiang Zhang, Dillon Fuerth, Junfeng Su and all the other people I have met at the University of Windsor for their help, encouragement and friendship.

*Dedicated to my parents and my wife.*

# TABLE OF CONTENTS

AUTHOR'S DECLARATION OF ORIGINALITY .....	iii
ABSTRACT .....	iv
ACKNOWLEDGEMENTS.....	v
DEDICATION .....	vi
LIST OF FIGURES .....	xii
LIST OF TABLES .....	xvii
LIST OF SYMBOLS .....	xx
CHAPTER 1 INTRODUCTION.....	1
1.1 Introduction .....	1
1.2 Background information .....	2
1.3 Objective .....	5
CHAPTER 2 LITERATURE REVIEW .....	7
2.1 Overview of DP steels .....	7
2.1.1 Methods of producing DP steels .....	7
2.1.2 Theory of DP steel production .....	10

2.1.3	Deformation behaviour .....	15
2.2	Martensite banding caused by Mn segregation .....	17
2.3	Types of fracture .....	22
2.4	Overview of tube bending .....	24
2.4.1	Tube making .....	24
2.4.2	Tube bending .....	27
2.4.2.1	Bend ratio and axial strain .....	30
CHAPTER 3	EXPERIMENTAL PROCEDURES AND MATERIALS .....	32
3.1	Materials .....	32
3.2	Mechanical testing .....	33
3.2.1	Tensile tests .....	33
3.2.2	Tube bending test .....	34
3.2.2.1	Tube preparation .....	34
3.2.2.2	Rotary draw bending .....	36
3.2.2.3	Strain and thickness measurements .....	37
3.3	Microstructural analysis .....	39
3.3.1	Specimen preparation .....	39



3.3.2	SEM and optical microscopy .....	40
3.3.3	Metallographic analysis .....	41
3.3.3.1	Measurement of grain size .....	41
3.3.3.2	Measurement of martensite volume fraction and void area fraction .....	41
3.3.3.3	Measurement of martensite and ferrite deformation .....	42
3.3.3.4	Estimation of martensite carbon content .....	42
3.4	Correlation and regression analysis .....	43
CHAPTER 4 RESULTS AND DISCUSSION .....		46
4.1	Mechanical testing results .....	46
4.1.1	Tensile testing results .....	46
4.1.2	Rotary draw bending results .....	49
4.2	Effect of martensite banding and possible solutions .....	53
4.2.1	Quantitative measure of martensite banding .....	54
4.2.2	Effect of martensite banding on tensile properties .....	57
4.2.3	Possible solutions .....	62
4.3	Failure analysis .....	64
4.3.1	Non-metallic inclusions .....	64

4.3.1.1	Ductile sulfide inclusions (stringers) .....	65
4.3.1.2	Oxide inclusions (globular) .....	68
4.3.1.3	Sources of inclusions and possible solution .....	69
4.3.2	Damage mechanisms and void formation .....	71
4.3.2.1	Fractographs of the failures in tube bending tests .....	71
4.3.2.2	Observation of void nucleation and propagation in bent tubes .....	73
4.3.2.3	Minimum bend ratio for various DP steel grades .....	76
4.3.2.4	Void formation and mechanical properties .....	79
4.3.2.5	Evaluation and prediction of the minimum bend ratio (maximum axial strain) in rotary draw bending .....	86
4.4	Deformation behaviour of DP steels in tube bending .....	91
4.4.1	Background of DP steels deformation behavior (analysis of stress-strain curves for C-Mn DP steels) .....	91
4.4.2	Ferrite and martensite deformation behaviour .....	94
CHAPTER 5	CONCLUSIONS .....	99
CHAPTER 6	RECOMMENDATIONS FOR FUTURE WORK .....	101

REFERENCES ..... 103

APPENDIX

A. Effective strain calculation ..... 113

## LIST OF FIGURES

Figure 1: Strength-elongation relationships for different steel grades .....	2
Figure 2: ULSAB-AVC with significant claims of improvement performance with AHSS .....	3
Figure 3: Comparison of different AHSS .....	4
Figure 4: Hot rolling mill (Photograph courtesy of ArcelorMittal) .....	8
Figure 5: Cold rolling mill (Photograph courtesy of ArcelorMittal) .....	8
Figure 6: Typical thermal treatment for DP steels .....	9
Figure 7: A portion of the Iron-Carbon phase diagram .....	11
Figure 8: Continuous cooling transformation diagram (CTT) of DP steel .....	11
Figure 9: Morphology of different grades of DP steel .....	14
Figure 10: A) Lath martensite, B) Twinned martensite .....	14
Figure 11: Comparison of sheet stretchability for various grades of steel (measured by a hole expansion test) .....	16
Figure 12: Martensite banding in DP steel .....	18
Figure 13: Solidification process .....	18

Figure 14: Typical SEM fractographs:	
a). Ductile Fracture in 1020 steel	
b). Brittle Fracture in Niobium-Alloy steel	..... 23
Figure 15: Quasi-Cleavage fracture of high alloy steel	..... 24
Figure 16: Tube rolling mill	..... 25
Figure 17: Strength of DP steel after each forming stage	..... 27
Figure 18: Schematic of a rotary draw bender	..... 28
Figure 19: Forces in the tube wall during bending	..... 29
Figure 20: Thickness distribution around the tube circumference after bending (63.5mm outside diameter, 1.2mm wall thickness, R/D=3.1)	..... 29
Figure 21: Longitudinal cross section of bent tube and displacement of neutral axis	..... 31
Figure 22: ASTM E8-08 Standard tension test sheet-type specimens	..... 33
Figure 23: Locations around circumference of tube where tensile tests were taken	..... 34
Figure 24: A tube electro etched with circle grids	..... 35
Figure 25: Electro etching apparatus and grid pattern sheet	..... 35
Figure 26: Rotary draw bender at VariForm	..... 36
Figure 27: Strain measurement system	..... 37

Figure 28: Sections of tube sample and measurement points .....	38
Figure 29: Schematic illustration of the main experiments and analysis .....	45
Figure 30: Typical engineering stress-strain curve of DP steel sheets .....	46
Figure 31: The Influence of martensite volume fraction and martensite carbon content on total elongation of C-Mn DP steels .....	48
Figure 32: Axial and thickness strain distributions along the outside of bent tubes (Bend ratio - 3.1) .....	50
Figure 33: Axial and thickness strain distributions along the outside of bent tubes (DP780) .....	51
Figure 34: Axial and thickness strain distributions around the circumference of bent tubes (DP780) .....	51
Figure 35: Martensite banding in different DP steel grades (Optical micrographs of sheet samples) .....	53
Figure 36: Effect of Mn content on martensite banding .....	56
Figure 37: Total elongation of each steel grade in different orientation .....	57
Figure 38: Yield and tensile strength of each steel grade in different orientation .....	58
Figure 39: Typical engineering stress-strain curves for DP780 and DP980 steel sheet .....	58

Figure 40: Optical micrographs of martensite banding distribution in cross-section direction of a DP steels sample (Thickness: 1.2mm) .....	62
Figure 41: Microvoids caused by sulfide Inclusions (after bending) .....	65
Figure 42: The EDS analysis graph (area of analysis indicated by the arrow in Figure 41) .....	65
Figure 43: Surface crack on a bent tube .....	67
Figure 44: Fractograph of the surface crack .....	67
Figure 45: The EDS analysis graph (area of analysis indicated by the rectangle in Figure 44) .....	67
Figure 46: Oxide inclusion in C-Mn DP steels (after Bending) .....	68
Figure 47: The EDS Analysis graph (area of analysis indicated by cross in Figure 46) .....	68
Figure 48: SEM fractographs for the three steel grades of DP steel .....	71
Figure 49: Void nucleation and propagation (Samples from bent tube) A: Void nucleation and coalescence in the ferrite matrix; B: Martensite decohesion C: Voids caused by Inclusions (sulfide); D: Crack is blocked by martensite .....	74
Figure 50: The low magnification fractograph (the sample taken from the outside wall of a bent tube) .....	76

Figure 51: Forming limit diagram (FLD) of C-Mn DP steels for bending trials .	78
Figure 52: Void area fraction in bent tubes for different steel grades .....	79
Figure 53: Average void radius in bent tubes for different steel grades .....	81
Figure 54: Comparison of elongation values for three grades of DP steel .....	86
Figure 55: Actual bend ratio vs. calculated bend ratio .....	89
Figure 56: Hollomon relation $\ln\sigma$ vs. $\ln\epsilon$ .....	92
Figure 57: Ludwik relation $\ln(d\sigma/d\epsilon)$ vs. $\ln\epsilon$ .....	93
Figure 58: Martensite and ferrite strains .....	95
Figure 59: Axial strain of ferrite and martensite vs. martensite volume fraction for a 3.1 bend ratio .....	96
Figure 60: Evolution of the ratio of ferrite to martensite strain ( $\epsilon_F/\epsilon_M$ ) with bending strain .....	97



## LIST OF TABLES

Table 1: Equilibrium partition ratios for various alloying elements in steel .....	10
Table 2: Classification of fractures in terms of various characteristics of metals .....	22
Table 3: Appearance of brittle and ductile fracture at various scales .....	23
Table 4: Deformation of ERW tube during the tube making process .....	26
Table 5: Composition of the investigated steels (Source: ArcelorMittal) .....	33
Table 6: Tensile tests results of DP steel sheet and tube .....	47
Table 7: The microstructural parameters and main chemical composition of DP steels .....	48
Table 8: Results of rotary draw bending tests at VariForm .....	49
Table 9: True axial strain of bent tubes of different DP steel grades .....	52
Table 10: Measures of martensite banding in each DP steel .....	55
Table 11: Average mechanical properties for C-Mn DP steel sheet .....	57
Table 12: Mean free path of ferrite grains and martensite volume fraction of C-Mn DP steels in different steel grades .....	60
Table 13: Chemical composition of a sulfide inclusion (area of analysis is indicated by the arrow in Figure 41) .....	66

Table 14: Chemical composition of an aluminum-oxide inclusion (area of analysis is indicated by the cross in Figure 46) .....	69
Table 15: The fractographic characteristic description .....	72
Table 16: Main factors which may influence the mechanical properties .....	82
Table 17: List of correlation coefficients .....	83
Table 18: Effect of void area fraction on post-uniform elongation.....	85
Table 19: Effective strain in critical bend ratio for various C-Mn DP steel grades .....	87
Table 20: Analytical representations of strain - stress curves .....	91

## LIST OF SYMBOLS

$\epsilon_1$	Axial Strain along the outside of bent tubes
$\epsilon_2$	Hoop Strain along the outside of bent tubes
$\epsilon_3$	Thickness Strain along the outside of bent tubes
$\epsilon_{e1}$	Effective Strain along the outside of bent tubes (hoop strain=0)
$\epsilon_{e2}$	Effective Strain along the outside of bent tubes (hoop strain $\neq$ 0)
$\epsilon_u$	Uniform elongation
$\epsilon_t$	Total elongation
$\epsilon_f$	Strain of ferrite
$\epsilon_m$	Strain of martensite
$\sigma_\alpha$	Strength of ferrite
$\sigma_m$	Strength of martensite
$\sigma_{UTS}$	Tensile strength
$r$	r-value of the steel sheet
$C_0$	Carbon content of steel
$C_m$	Carbon content of martensite
$C_\alpha$	Carbon content of ferrite
$Mn$	Manganese content of the steel
$f_m$	Volume fraction of martensite
$f_v$	Void area fraction
$l_1$	Length of an ellipse along major axis
$l_2$	Length of an ellipse along minor axis
$l_0$	Initial diameter of circles

$t_0$	Initial wall thickness of the tube
$t$	Final wall thickness of the tube
$D$	Outer diameter of tube
$R$	Centre-line radius of bent tube
$\delta$	Neutral axis displacement
$AI$	Anisotropy index
$\rho_L$	Banding length density

# CHAPTER 1

## INTRODUCTION

### 1.1 Introduction

In view of growing environmental concerns, there have been rapid technological developments in the automotive industry to improve fuel economy and reduce vehicle emissions. Efforts have been made to produce lightweight vehicles without losing structural integrity and crash resistance. Steels with strength-ductility combinations were sought to enable the fabrication of complex shaped automotive components using the same techniques that were developed for plain carbon steel.

Figure 1 is a diagram that relates the ductility to the strength of the most common grades of steel. Considering their strength, formability, weldability and cost, dual phase (DP) steel, as one kind of advanced high strength steel (AHSS), can meet the requirement of the automotive industry. Its special microstructural features, hard martensite embedded in a soft ferrite matrix, enables the steel to possess both good formability and high strength.

The first patent for DP steel was submitted in the United States in 1968 [1], but the advantages and potential applications of this grade of steel were not fully understood until Hayami and Furukawa [2] systematically and fully depicted their microstructural features, chemical composition, formability and mechanical properties. Since then, DP steels have been used increasingly because of their combination of strength and formability. In the past 30 years, numerous papers and investigations [4-12] have focused on the potential applications of DP steel.

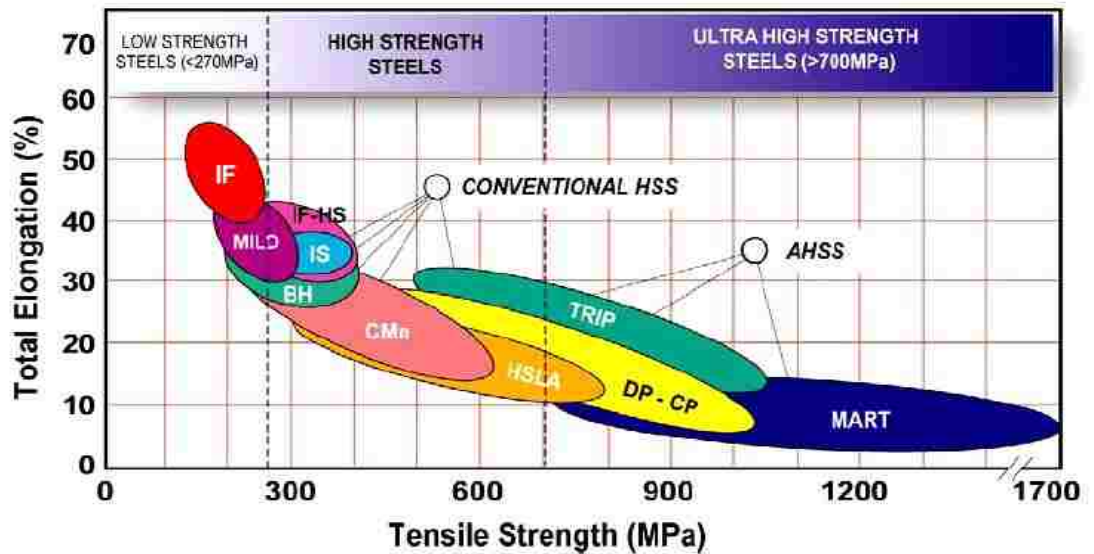


Figure 1: Strength-elongation relationships for different steel grade [3]

## 1.2 Background information

The utilization of advanced high strength steels (AHSS) for automotive body-in-white applications has been steadily increasing over the last few years. In the future, some predict that DP steels may comprise up to 70-80% of AHSS applications in passenger vehicles as shown in Figure 2. Dinda et al. [12] have reported that decreasing an average car weight from 1750kg to 1500kg can improve the fuel consumption by up to 2km/l.

DP steels, with their hard phase islands (martensite) embedded in a soft phase (ferrite), have unique properties such as high strength, low yield-to-tensile strength ratio, high initial work hardening rate, continuous yielding behaviour, bake hardenability, and no room temperature aging effects. These properties

mainly depend on the size, volume fraction, distribution and carbon content of the martensite phase. Compared to conventional high strength steels ( Figure 3) and mild steel, the strength of DP steels is significantly greater without any loss of formability. Therefore DP steels allow enhanced design flexibility and provide a significant thickness and weight reduction in structural components.

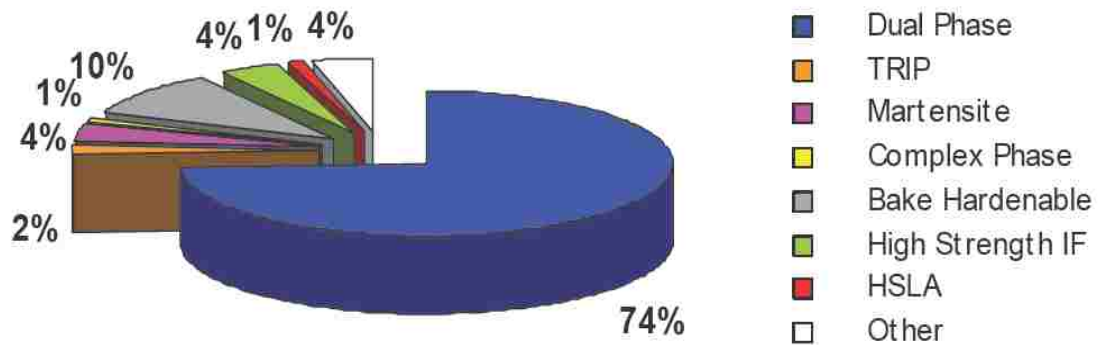


Figure 2: ULSAB-AVC with significant claims of improvement performance with AHSS [13]

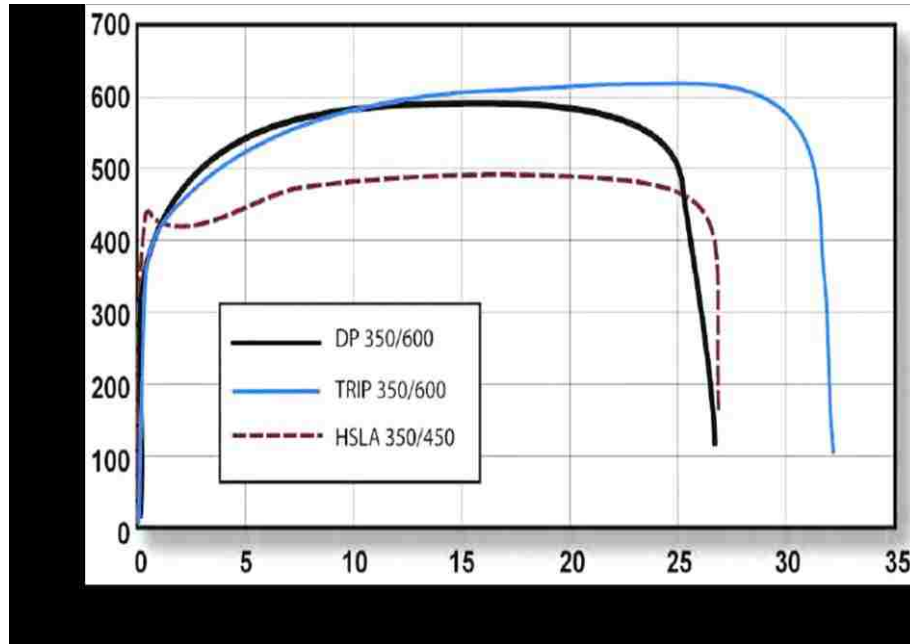


Figure 3: Comparison of different AHSS [15]

In many automotive applications, tube bending and hydroforming have shown good potential for manufacturing high-quality parts with lower production cost and high productivity in comparison with conventional stamping and welding processes. The purpose of bending is to reach a centreline-geometry close to that of the final part to be manufactured by hydroforming, thereby enabling the tube to fit the die cavity [14]. Tube hydroforming is a forming process in which tubes (straight or pre-bent) are formed into complex shapes inside a die using simultaneous application of internal pressure and axial compressive forces from one or both ends [15]. As a result, due to the advantage of a better combination of strength and formability, DP steel tubes, which are welded by electrical resistance welding (ERW) or laser welding, are widely used in the automotive industry.



### 1.3 Objective

VariForm, a Tier 1 automotive part supplier, routinely bends DP steel tubes in a rotary draw bending machine prior to hydroforming. VariForm personnel found that DP steel tubes with similar mechanical properties can behave very differently during rotary draw bending. Some batches of DP steel tubes yield high scrap rates whereas other batches with similar specifications yield few or no failures. It is thought that microstructure, chemical composition and processing of DP steel may explain the differences in tube behaviour during the bending process

At present, considerable research has been done to characterize the deformation mechanisms and structure-properties relationships in DP steels. But little work has been concerned with the effects of the microstructural features and deformation behaviour on the onset of the failure in the bending process.

The aim of this work is to identify the parameters, such as mechanical properties, chemical composition, microstructural features, and strain distribution between martensite and ferrite, which affect the onset of failure in bent DP steel tubes, by using tensile tests, special bending tests and microstructural analysis at VariForm and the University of Windsor.

The objective of this project was completed by considering:

- The effect of martensite banding on mechanical properties
- Failure analysis
- The deformation behaviour of DP steels in tube bending

Following the analysis of experimental data, efforts were made to establish a correlation between material parameters and the onset of failure in tube bending. Moreover, predictive empirical equations were established based on this data, and, finally, assistance was provided to VariForm with a view to improving the tube bending process.

## **CHAPTER 2**

### **Literature Review**

#### **2.1 Overview of DP steels**

Since the 1970s, DP steels, due to their unique properties, have been widely applied in the industry on a large scale, particularly in the automotive industry. A brief overview of C-Mn DP steels and their production process, especially those applicable to this project, is first provided.

##### **2.1.1 Methods of producing DP steels**

Various developments [6,7,16-18] have demonstrated that a C-Mn DP steel, which is essentially a plain carbon steel with or without alloying elements, does not automatically guarantee good formability by itself. The objective of good formability combined with high strength, which is different from those of ferrite-pearlite steels such as plain carbon steels or micro-alloyed, high strength low alloy (HSLA) steels, can be accomplished by innovative process control.

Molten DP steel is produced in an oxygen top blowing process in the converter, and undergoes an alloy treatment in the secondary metallurgy phase. The resulting product is aluminum-killed steel, with a high tensile strength achieved by addition of manganese, chromium and silicon [19].

In general, there are three ways to produce DP steel:

- **Hot rolling**

Hot rolled DP steel has the obvious advantage of saving energy cost by eliminating a heat-treatment step. Also balanced against these advantages are the disadvantages of higher alloy cost, more variability in properties [6,7, 20] and thicker gauge [8]. Hot rolled DP steel strip is mainly used to make automotive wheels [21]. Figure 4 shows the schematic illustration of hot rolling mill.

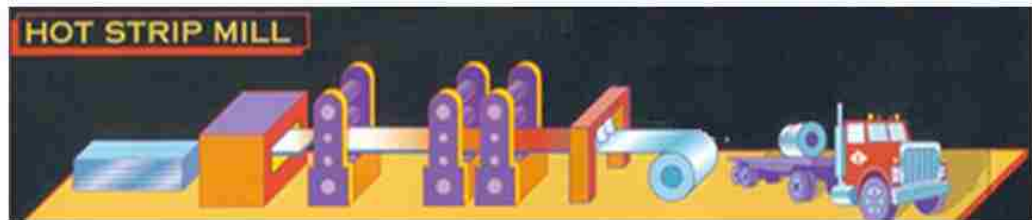


Figure 4: Hot rolling mill (Photograph courtesy of Arcelor-Mittal)

- **Hot rolling → Cold rolling → Continuous annealing**



Figure 5: Cold rolling mill (Photograph courtesy of Arcelor-Mittal)

A considerable amount of research and production activity has been reported for the hot rolling, cold rolling (Figure 5) and continuous annealing process [6,8, 22-24]. This is due to the low production costs, high productivity and ultra-thin gauges which can be reached, compared to hot rolled or batch annealed DP strip.

The first application of continuous annealing was by Armco Steel Corporation in the US for hot dip galvanized steel in 1936. Early in the 1970s, Japanese steel-makers incorporated an overaging treatment in the continuous annealing process to improve the mechanical properties (Figure 6) [8]. Since then, non-microalloyed C-Mn DP steels can be produced by cold rolling, followed by a continuous annealing heat treatment. Thus, at present C-Mn DP steels are widely used in the automotive industry.

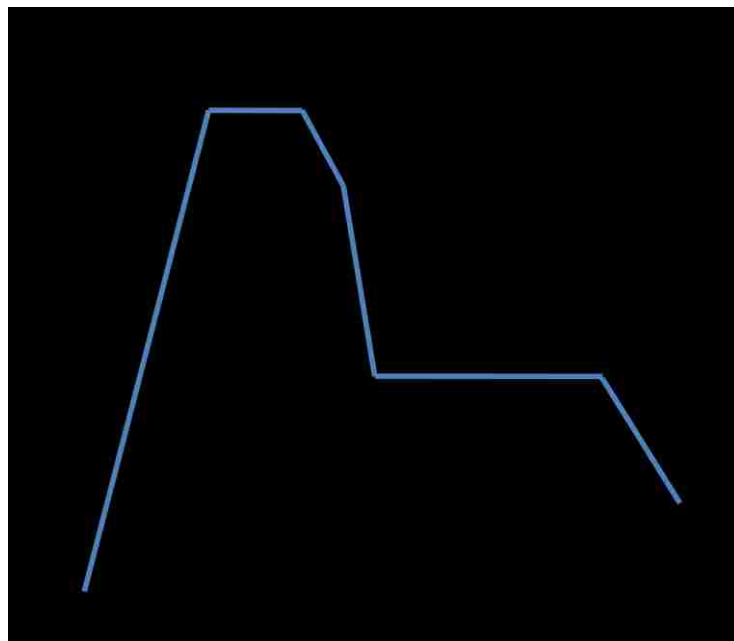


Figure 6: Typical thermal treatment for DP steels [22]

- **Hot rolling → Cold rolling → Batch annealing**

In the batch annealing process, a similar heat treatment is performed, but the annealing time is much longer and the cooling rate is much slower. Therefore some researchers also call batch annealing an isothermal reaction treatment [9]. Because of the slow cooling rate, alloying elements (molybdenum and chromium)

are added to the steel, in order to achieve the desired hardenability of the austenite, and to obtain the required DP microstructure [7-9].

The austenite transformation mechanisms are similar to those observed during continuous annealing but the grain size and substructure are characteristic of much slower cooling rates involved [8].

Slower cooling rates produce a better strength-ductility combination and are generally preferred because they result in less lattice defects and residual stresses in the ferrite. Higher cooling rates may also reduce ductility slightly [25]. However, the lower productivity and higher production cost of batch annealing have limited the range of applications of batch annealed DP steels.

### **2.1.2 Theory of DP steel production**

The microstructure of most DP steels prior to rolling or heat treatment consists of ferrite, pearlite, and grain boundary iron carbides [8,9,26]. Regardless of the production process, whether hot or cold rolling, batch or continuous annealing, the cooling method remains the same. DP steels are heated within the intercritical temperature range which is in the field  $\alpha+\gamma$  of the Fe-C phase diagram shown in Figure 7. Subsequently, through rapid cooling, austenite begins to transform to martensite when the temperature reaches the  $M_s$  temperature. As shown in Figure 8, the black curve represents the typical cooling path of C-Mn DP steels.

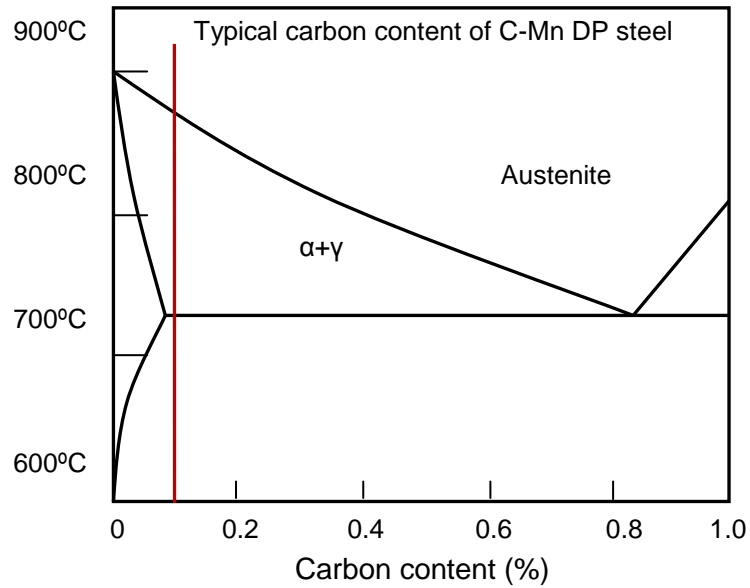
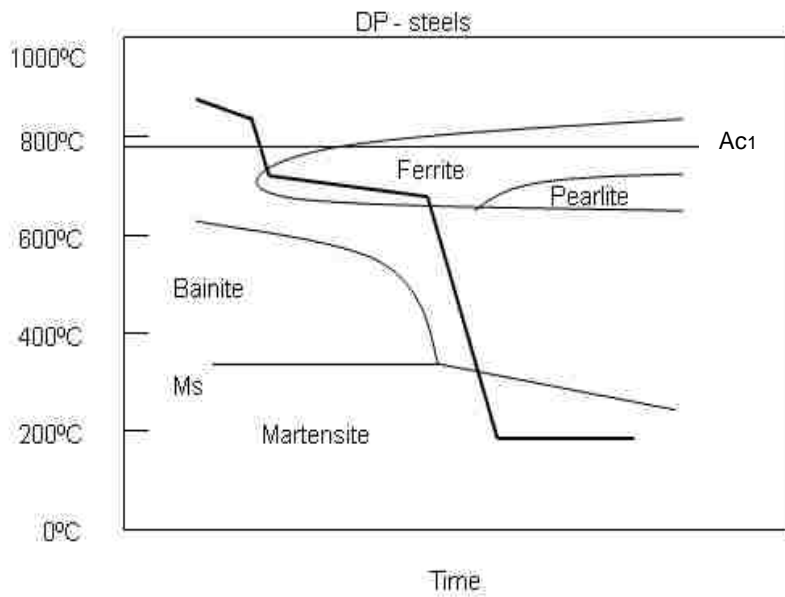


Figure 7: A portion of the Iron-Carbon phase diagram



Note: Ac1 - austenite transformation start temperature on heating  
 Ms - martensitic transformation start temperature

Figure 8: Continuous cooling transformation diagram (CTT) of DP steel [22]

All reported theories of producing DP steels have three common stages [8, 9, 27, 28]:

1. Heating above the lower intercritical temperature and holding for a short time. This determines the volume fraction of austenite.
2. Cooling below the martensite start temperature ( $M_s$ ), which promotes the transformation of the austenite into martensite. The cooling rate must be fast enough to obtain martensite from the austenite transformation. Sometimes, before rapid cooling, slow cooling is used to purify the ferrite (epitaxial ferrite growth) and to increase the carbon concentration in the austenite and thereby increase its hardenability.
3. After cooling from the intercritical annealing temperature, some processes also include an overaging stage below the martensite start temperature to improve the ductility and toughness of the steel at the expense of tensile strength.

Research and development shows [6-9] that the DP microstructure cannot guarantee an excellent combination of strength and formability without a proper control of the chemical composition and processing parameters.

In the production process, parameters such as annealing temperature, soaking time and cooling rate control the volume fraction and composition of the ferrite and austenite [8,9]. For C-Mn DP steels, the presence of Si in the ferrite promotes carbon migration from the ferrite to the austenite, while Mn diffuses preferentially to the austenite and increases its hardenability [29,30].



Some empirical equations were developed in order to determine the transformation temperature as a function of the chemical composition of DP steels [31].

$$Ac1 = 723 - 10.7Mn - 16.9Ni + 29.1Si + 16.9Cr \quad (2-1)$$

$$Ms = 539 - 423C - 30.4Mn - 17.7Ni - 12.1Cr - 7.5Mo \quad (2-2)$$

where the element content is specified in percent. Therefore, as a result of the different chemical composition and processing parameters, DP steels develop different mechanical properties which mainly depend on microstructural features, such as martensite volume fraction, grain size of the ferrite and martensite, and martensite distribution. As shown in Figure 9, the microstructure of DP steels varies significantly with the ultimate strength.

In addition, the martensite transformation substructure in DP steels, which plays an important role in the mechanical behaviour, can vary from a lath martensite substructure typical of low-carbon martensite (Figure 10A), to internally twinned substructures typical of high carbon martensite (Figure 10B). These changes in morphology reflect the effect of the intercritical annealing temperature and chemical composition on the carbon content of the austenite phase, and in turn this affects the Ms temperature [32].

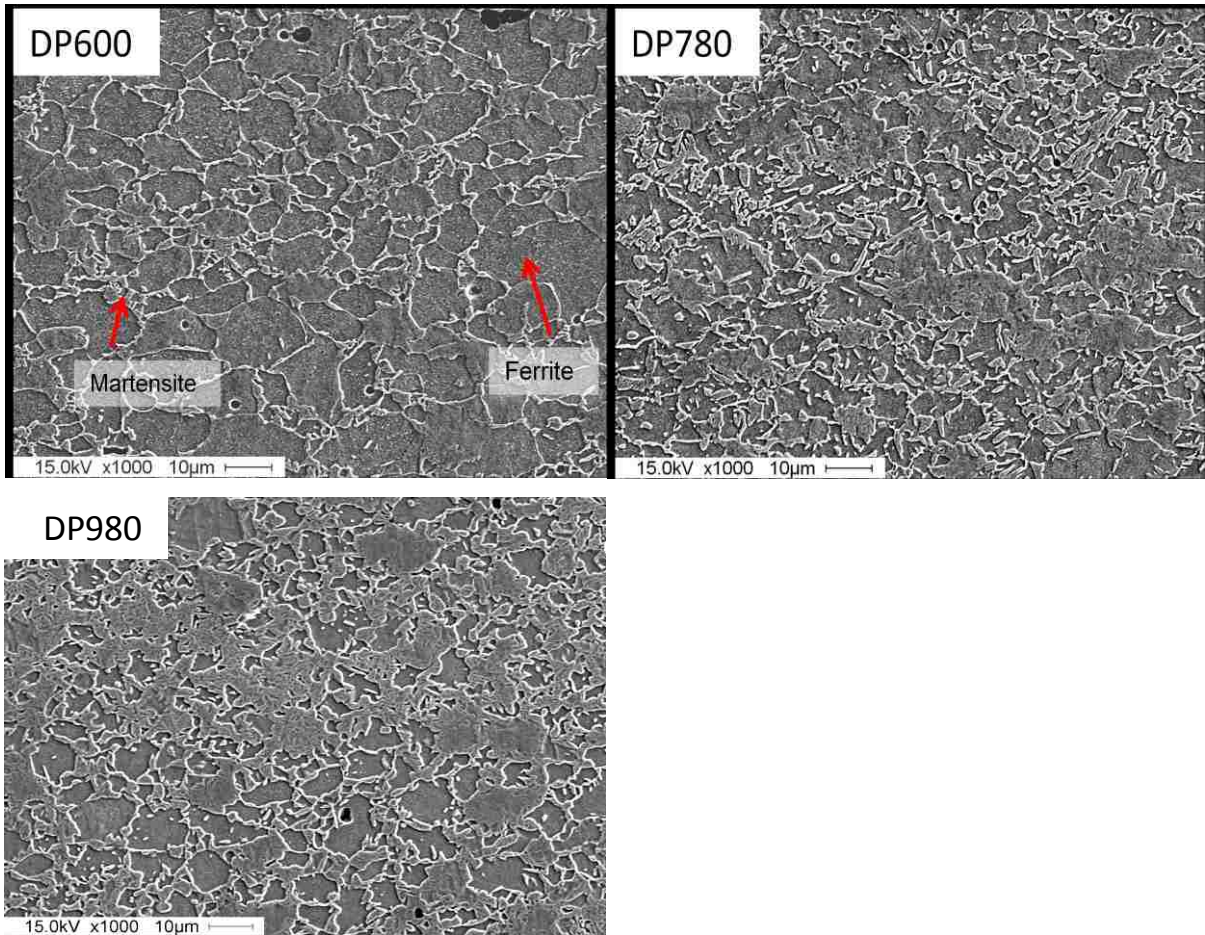


Figure 9: Morphology of different grades of DP steel

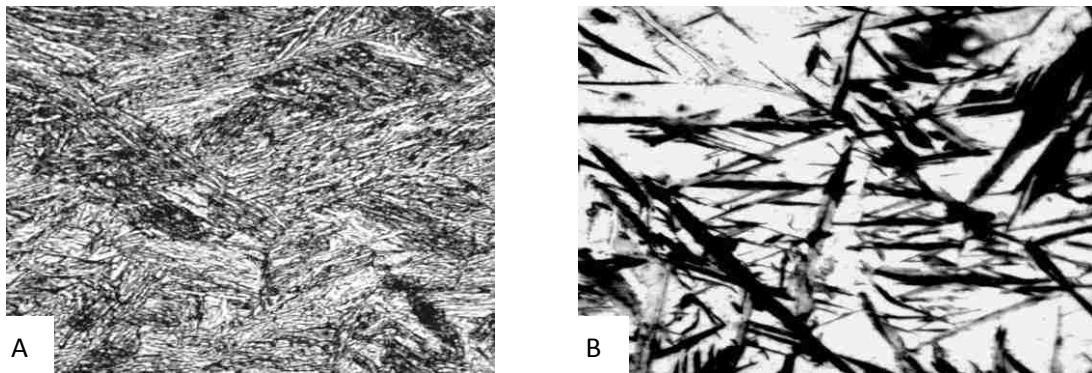


Figure 10: A) Lath martensite B) Twinned martensite [33]

### 2.1.3 Deformation behaviour

The stress-strain behaviour of DP steels is characteristically different from that of high strength low alloy (HSLA) steels as shown in Figure 3. The composite microstructure is the main reason for the excellent deformation behaviour of DP steels. During the austenitic transformation, the expansion of the martensite results in disorder in the neighbouring ferrite. Therefore, DP steels display a low yield stress and no yield point elongation because of high residual stresses and highly mobile dislocations [34].

Compared to HSLA steel, DP steels have some advantages which are listed below:

- Low yield strength
- High tensile strength
- Good uniform elongation
- High initial work hardening rate
- Continuous yield behaviour
- No room temperature aging effect

However, due to the low local elongation, referring to Figure 11, the stretchability of DP steels is worse than that of HSLA steel.

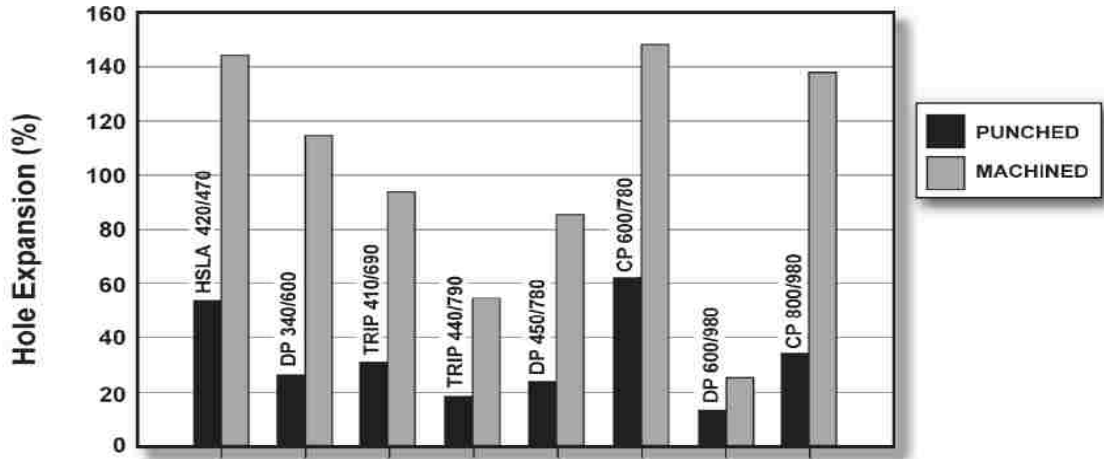


Figure 11: Comparison of sheet stretchability for various grades of steel (measured by a hole expansion test) [2]

The deformation behaviour of DP steels is quite complex due to the composite microstructure. Hollomon's stress-strain relation, which is suitable for most steels, is not adequate for DP steels [35]. So far, a thorough understanding of the interactions between the various microconstituents discussed and their influence on mechanical properties is lacking [9].

There have been many attempts [36-45] to rationalize the mechanical properties of DP steels in terms of the micro-mechanics of the two phase system. Until now, many of them [41-45] are based on the rule of mixtures which is valid for fibre-reinforced polymeric composite materials.

$$\sigma = (1 - f_m)\sigma_\alpha + f_m\sigma_m \quad (2-3)$$

$$\varepsilon = (1 - f_m)\varepsilon_\alpha + f_m\varepsilon_m \quad (2-4)$$

where

$\sigma_{\alpha}$  – Strength of ferrite

$\sigma_m$  – Strength of martensite

$\epsilon_{\alpha}$  – Strain of ferrite

$\epsilon_m$  – Strain of martensite

$f_m$  – Volume fraction of martensite

The problem with the law of mixtures is that it is difficult to accurately predict the stress and strain distribution in each of the phases during deformation for different DP steels with various chemical compositions and processing parameters. However, the rule of mixtures may be suitable to establish an equation to predict the strength of DP steels with similar chemical compositions and processing parameters [8].

## **2.2 Martensite banding caused by Mn segregation**

During the modern steel making process, molten steel is essentially uniform in chemistry. Following casting, macroscopic and microscopic segregation of chemical elements between the parent liquid and growing solid crystals, produces non-uniformity in the distribution of chemical elements which is inherent to solidified cast products [46]. Macroscopic segregation of alloying elements occurs in different cross-sectional positions in cast steels depending on the casting equipment. Microscopic segregation occurs between dendrites throughout a solidified section. Further deformation, such as hot rolling, aligns the microscopic

segregation of alloying elements into longitudinal bands. This is referred to as banding (Figure 12). Some degree of banding is found in all types of steel [47].

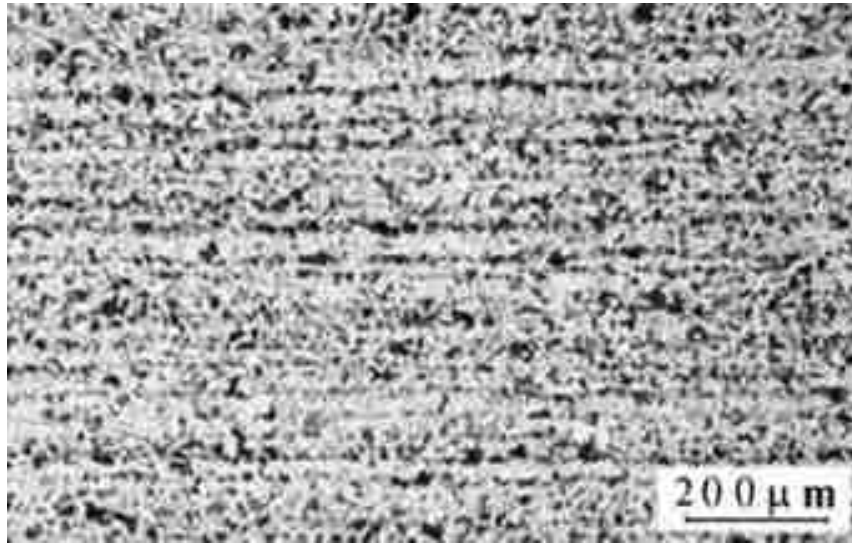


Figure 12: Martensite banding in DP steel [48]

Banding is initiated during the steel solidifying process. According to certain studies [8,47-50], the steel slab solidification process can be divided into three stages (Figure 13) as depicted below:

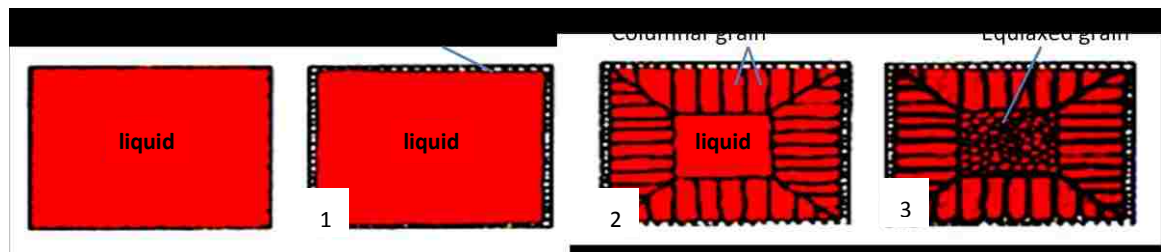


Figure 13: Solidification process

1. The supercooled grains in the surface zone are produced by a high rate of nucleation of fine, randomly oriented, equiaxed crystals in the highly supercooled liquid adjacent to a mold wall.
2. As solidification progresses, columnar crystals develop. Constitutional supercooling at the tips and edges of growing crystals promotes the elongated grain shape of the columnar zone.
3. The central zone of a cast product consists of equiaxed crystals. The equiaxed crystals are produced by nucleation in the highly constitutionally supercooled interior liquid.

The high and low solute regions are elongated into parallel bands during rolling and forming operation.

During the solidification process, solute atom redistribution during dendritic solidification is driven by equilibrium partitioning of chemical elements within the liquid-solid phase field [51]. Because of the difference in solute concentration of the solid and liquid, the dendrite cores solidify as relatively pure metal while the interdendritic spaces become rich in solute. The redistribution or partitioning of solute can be described as the equilibrium partition ratio,  $k$ ,

$$k = C_s / C_L \quad (2-5)$$

$C_s$  – Solute concentration of the solid

$C_L$  – Solute concentration of the liquid

Element	$k$
P	0.14
Nb	0.23
Cr	0.33
Mn	0.71
Ni	0.83



Table 1: Equilibrium partition ratios for various alloying elements in steel [52]

Table 1 lists  $k$  values, assumed to be independent of temperature, of some common alloying elements in steel. Solute elements with low values of  $k$  have the greatest tendency to segregate. Therefore, phosphorus has a very strong tendency to segregate during solidification. However, the amount of alloying element present is also a factor. Therefore, Mn, generally present in much higher concentrations than P, plays a more important role in segregation and banding than P in spite of its higher value of  $k$ . For a 1.0% Mn steel, Mn would vary from 0.70% at the beginning of solidification to 1.60% at the end of solidification [48].

Moreover, since the Mn diffusion rate in ferrite is much greater than in austenite and martensite, the Mn is enriched in the austenite, especially the rim of the austenite. This has been observed by several researchers [6,7,32]. The Mn enrichment of the austenite may increase hardenability near the austenite and ferrite interface, so that martensite is formed around the austenite particle. The centre of the austenite particle may transform to a ferrite carbide aggregate. This means that the martensite composition is usually nonhomogeneous and concentration gradients exist.



Reheating and hot rolling cast slabs or ingots can reduce chemical segregation, but further microstructural partitioning occurs during diffusion-controlled austenite transformations [20, 32]. Residual segregation can be estimated from:

$$C = C_0 \exp\left(-\frac{dt\pi^2}{l^2}\right) \quad (2-6)$$

$d$  – Diffusion coefficient at temperature

$t$  – Time

$l$  – One-half dendrite spacing

$C_0$  – Solute content difference in as-solidified structure

$C$  – Solute content difference after some time

Equation 2-6 shows that banding can be determined by temperature, time, dendrite spacing and solute content. However, according to this equation, the uniform diffusion of Mn would require many hours. Fisher *et al.* [52] point out that for a dendrite arm spacing of 300  $\mu\text{m}$  at a temperature of 1250 °C, 35 hours would be required to reduce the segregation of a typical substitutional element by 50%. Therefore, the time for complete homogenizing of chemistry are too long for modern steel mill productivity. In other words, it is impossible to eliminate element segregation for most steels.

## 2.3 Types of fracture

An analysis of a steel fracture may help to determine and describe the factors responsible for the onset of failure. Gensamer [53] summarized the terms commonly used to classify fractures based on their microstructure, appearance and deformation behaviour, as listed in Table 2.

Behaviour described	Terms used	
Crystallographic mode	Shear	Cleavage
Appearance of fracture	Fibrous	Granular
Strain to fracture	Ductile	Brittle

Table 2: Classification of fractures in terms of various characteristics of metals

Generally, the categories of ductile and brittle fracture (Figure 14) have already been broadly used to distinguish fractures.

Brittle fracture involves little or no plastic deformation and always occurs at stresses far below the yield strength. Brittle fractures are usually associated with flaws, are often catastrophic, and usually occur without warning [34].

Ductile fractures are high-energy fractures which occur in metals which have the ability to deform plastically prior to fracture. Unlike brittle fractures, they are characterized by stable crack propagation. If the applied load that causes a crack to propagate is removed, the crack stops [54].

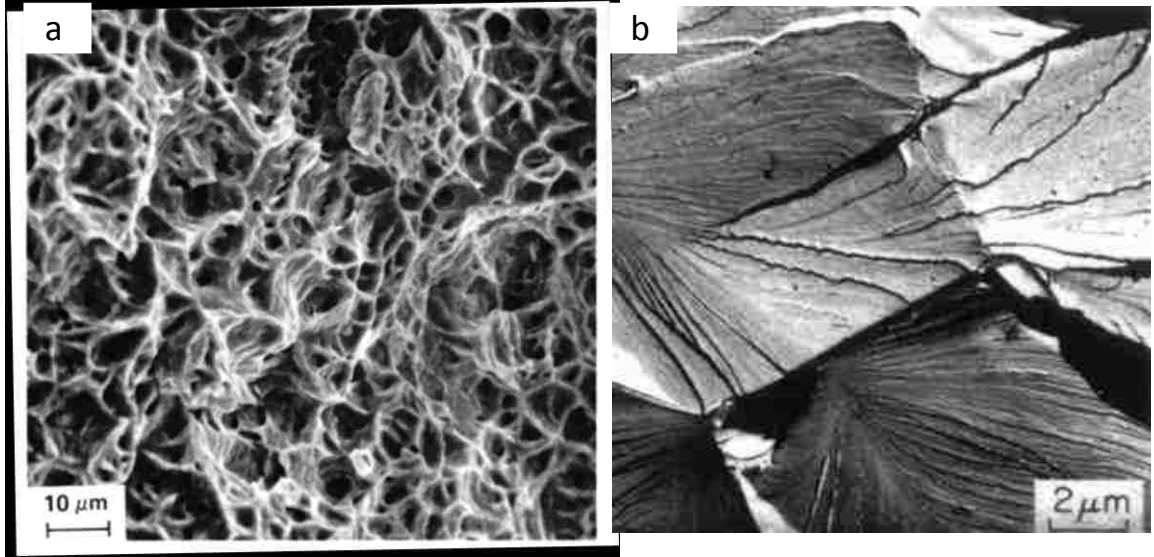


Figure 14: Typical SEM fractographs a) Ductile Fracture in 1020 steel [55]  
 b) Brittle Fracture in Niobium-Alloy steel [56]

To summarize, ductile and brittle fractures have various appearances as shown in Table 3.

Appearance	Brittle	Ductile
Gross	No plastic deformation	Gross plasticity, large deformation at fracture
Macroscopic	Flat	Shear (shear lips)
Fractographic	Cleavage	Dimples

Table 3: Appearance of brittle and ductile fracture at various scales [54]

In addition, martensite fails in a brittle manner, but does not cleave. Such fractures are identified as quasi-cleavage (Figure 15). Some researchers [57] interpret the quasi-cleavage fracture as a transition fracture mechanism between

cleavage and plastic fractures, or between brittle and ductile fractures. Therefore, it should be noted that the boundary between a ductile and brittle fracture is not always clearly defined.

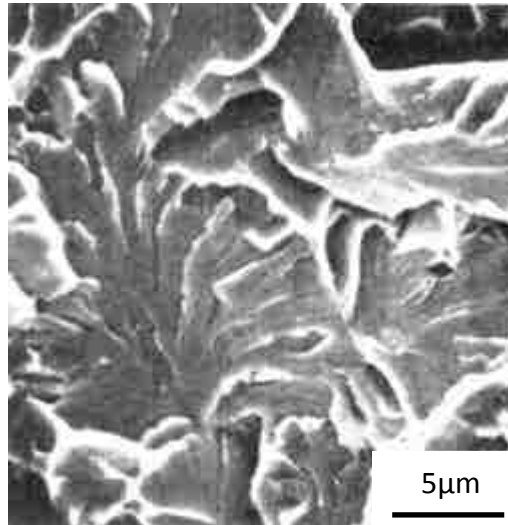


Figure 15: Quasi-Cleavage fracture of high alloy steel [57]

## 2.4 Overview of tube bending

### 2.4.1 Tube making

Depending on the manufacturing process, tubes can be divided into three categories: seamless, UOE and roll-formed tubes. Until now, the most common method of producing large quantities of tubes for automotive applications has been by roll-forming in a continuous tube-mill with electrical resistance welding (ERW) or laser welding (Figure 16) [58,59]. ERW tubing is produced from flat-rolled coils to ASTM A 513 specifications, either hot rolled or cold rolled. After

tube rolling and welding, the tube is sized to the final dimensions, diameter, ovality and required tolerances [58].

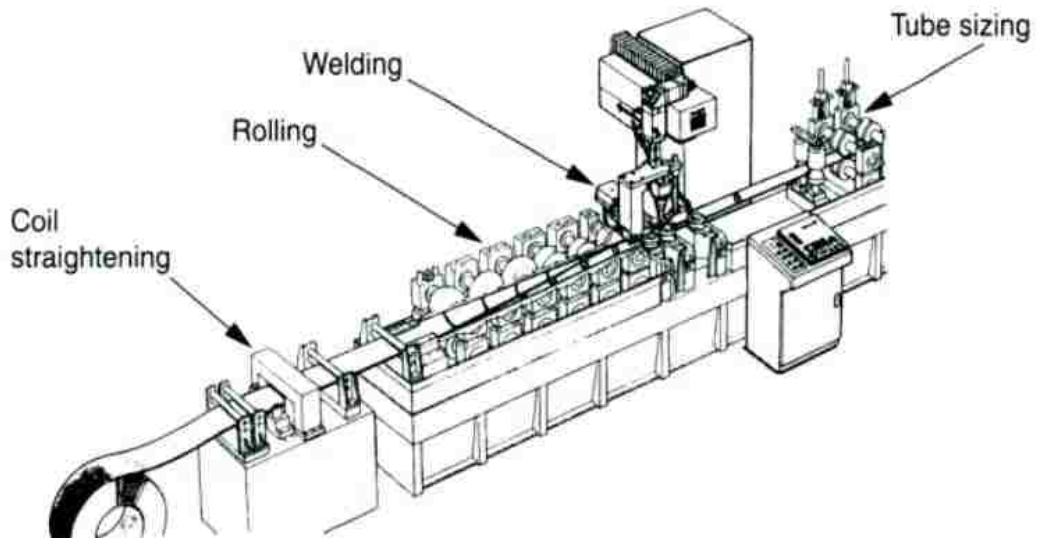
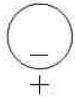
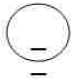


Figure 16: Tube rolling mill [56]

Laser welding can also be applied instead of electrical-resistance welding to give higher quality welds in which the heat-affected zone is much smaller. Products that require very high expansion ratios generally benefit by being laser-welded [58].

The weld seam in a tube results in an obvious non-homogeneity in material properties, and the formability of the weld seam and its heat-affected zone is usually lower than that of the parent material. However, tube failures rarely occur on or near the weld seam, because welding technology is well understood and some special measures are taken during tube production [60].

In the roll-forming and sizing operations, the deformation of the tube wall is minimized (Table 4). However, there is an inevitable loss of formability due to work hardening in spite of the small strain. For DP steel, because of its high initial work hardening rate, the DP steel tube wall is significantly work hardened during tube making as shown in Figure 17. Therefore it is necessary to minimize work hardening at this stage in order to maximize the remaining formability that will be required for subsequent processes.

Stage of process	Strain at the inside surface	Strain at the outside surface	Deformation of tube wall	Average strain	Schematic
Roll Forming	Compression	Tension	Bending	Bending: $t/2D$	
Sizing	Compression	Compression	Compression	Compression: 0.4-0.8%	

- Compression, + Tension,  $t$  - Tube wall thickness,  $D$  - Outer diameter

Table 4: Deformation of ERW tube during the tube making process [61]

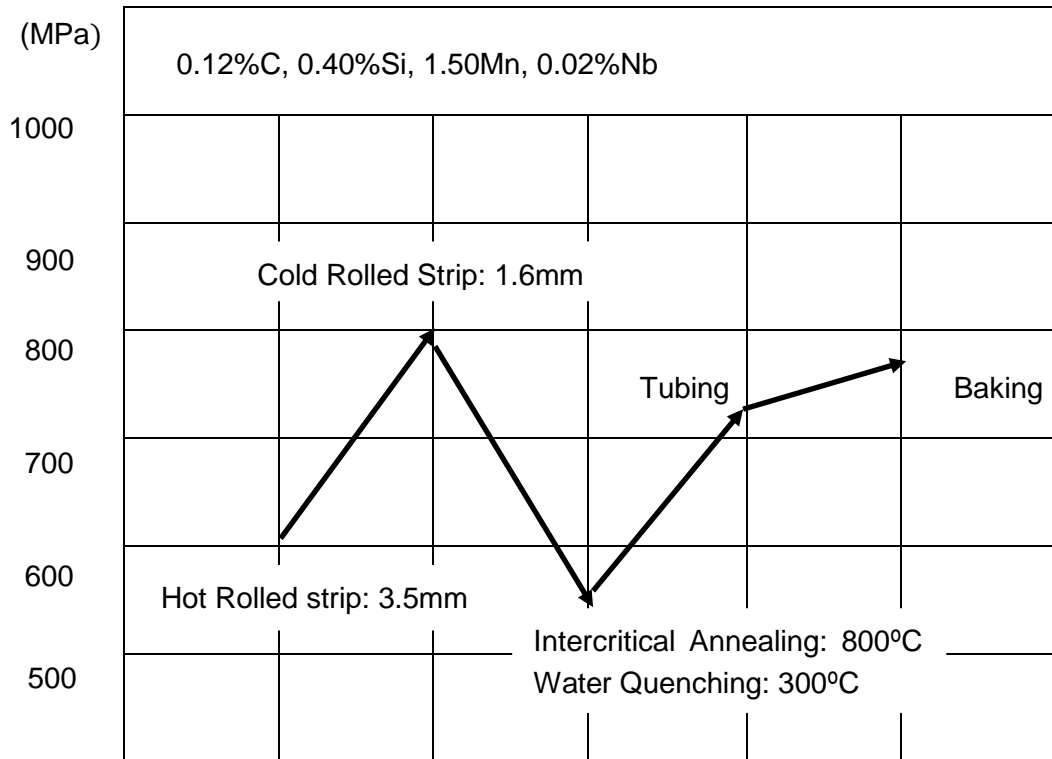


Figure 17: Strength of DP steel after each forming stage [62]

### 2.4.2 Tube bending

The manufacture of complex tubular products generally requires one or more forming operations prior to hydroforming. Bending is one of the most frequently applied pre-forming operations in the tube hydroforming industry [63].

Tube bending has long been considered as a craft, in which work was largely done by skilled labourers who had honed their skills over a period of many years [63]. At present, the demand for bent tubes has promoted a stronger knowledge base and more advanced technology in the tube bending industry.

The most popular, cost-effective and advantageous tube bending method is CNC rotary draw bending. Its major benefits are speed, accuracy, repeatability and relatively good control of wall thickness. Rotary draw bending applies both a bending moment and transverse loads on a straight tube [64,65]. Figure 18 shows a schematic of a rotary draw bender.

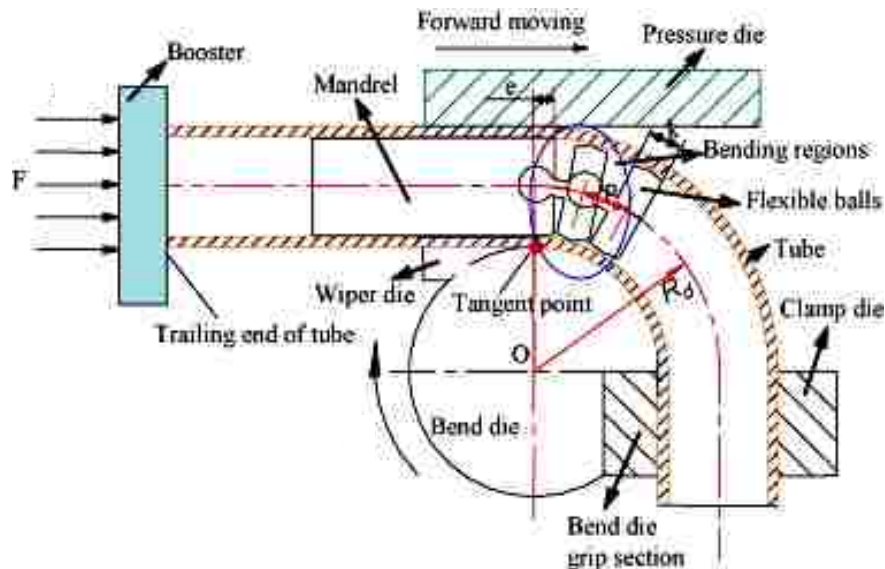


Figure 18: Schematic of a rotary draw bender [66]

During the bending operation, the tension loads on the outside of the bent tube and the compression loads on the inside of the bend (Figure 19) lead to a thickness reduction on the outside and a thickness increase on the inside of the bent tube (Figure 20).

As a result of the bending, the work hardening and non-uniform distribution of forces in the wall around the tube circumference influence the mechanical properties of the tube in the forming zone. This causes a substantial reduction in formability in subsequent hydroforming processes and also affects the uniformity of the wall thickness of final product [67].



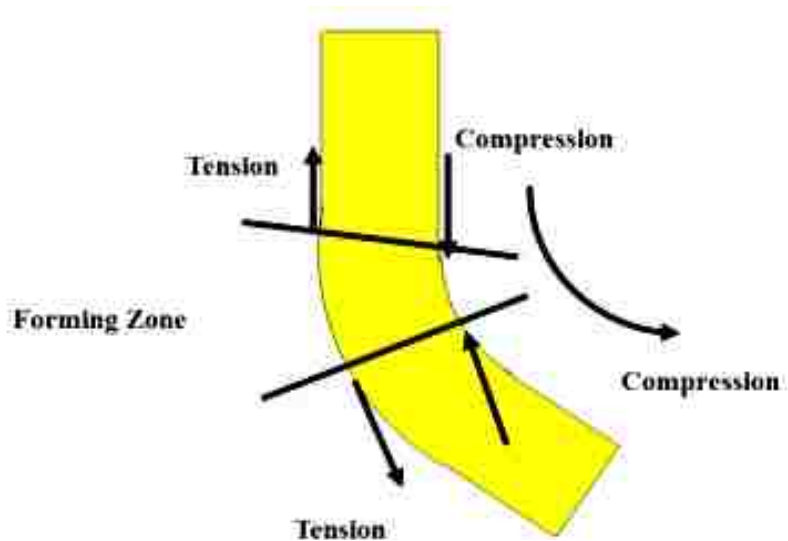


Figure 19: Forces in the tube wall during bending

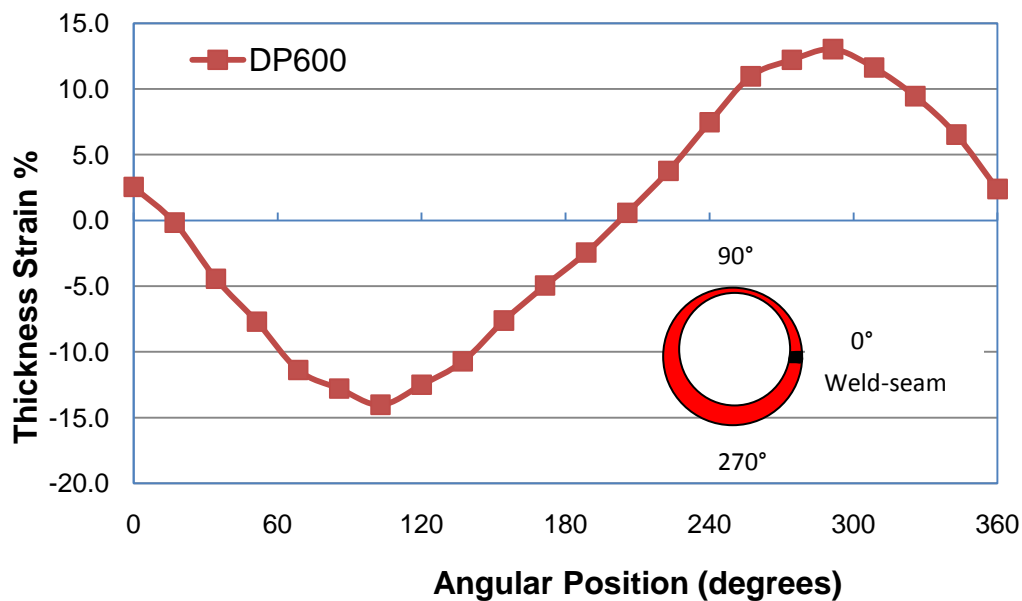


Figure 20: Thickness distribution around the tube circumference after bending (63.5mm outside diameter, 1.2mm wall thickness, R/D=3.1)

### 2.4.2.1 Bend ratio and axial strain

In tube bending, the bend ratio ( $R/D$ ), which is a measure of bend severity [67], represents the ratio of the centre-line radius of the tube to the outside diameter as shown in Equation (2-8). The bend ratio is one of the most important factors that affect tube deformation and process parameters during rotary draw tube bending. In 1979, Inoue and Mellor [68] showed that for steel tubes, a decrease in  $R/D$  ratio causes an increase of the major tensile axial strain (Equation 2-9) and leads to thinning around the outside of the bend region. The smaller the bend ratio, the higher the bending severity. Therefore, more severe bending results in higher work hardening and lower formability of the material, which affects subsequent deformation processes such as crushing and hydroforming.

$$\text{Bend ratio} = \frac{R}{D} \quad (2-7)$$

$R$  – Centre-line radius of bent tube

$D$  – tube outer diameter

Furthermore, during the deformation, the initial neutral axis experiences an elongation, which in-turn leads to the elongation of tube in the forming zone. As a result, the axis between the initial neutral axis and tube inside surface becomes the actual neutral axis, which has exactly same length and thickness as the initial neutral axis, as shown in Figure 21. The displacement of the neutral axis can be calculated with the following equation [69]:

$$\delta = \frac{D^2}{4R} \quad (2-8)$$

$\delta$  – Neutral axis displacement

Thus, considering the neutral axis displacement, the axial strain of bent tubes is obtained using the equation:

$$\varepsilon_1 = \ln\left[\left(1 + \frac{D}{2R}\right) / \left(1 - \frac{D^2}{4R^2}\right)\right] \quad (2-9)$$

$\varepsilon_1$  – Axial strain

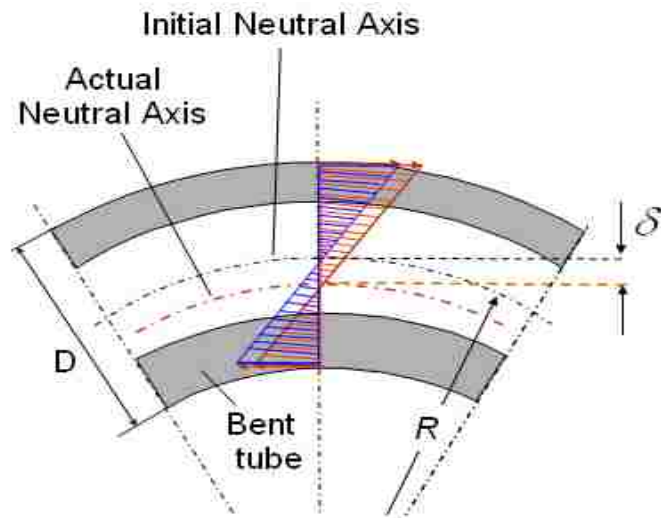


Figure 21: Longitudinal cross section of bent tube and displacement of neutral axis

This literature review of the metallurgy of DP steels and of tube bending was provided as a basis for further research. The effect of martensite banding will be studied in section 4.2. In addition, failure analysis and the strain distribution in each phase of DP steels will be presented in sections 4.3 and 4.4.

## **CHAPTER 3**

### **Experimental procedures and materials**

This chapter presents the experimental procedures, materials and analysis methods which were used to investigate the correlation between the microstructure of DP steels and rotary draw bending.

#### **3.1 Materials**

In this research project, three commercial grades of cold rolled C-Mn DP steels DP600, DP780, DP980, were selected and supplied by Arcelor-Mittal and SSAB. The DP steels were received in the form of 1.2 mm gauge coils of sheet, and were then roll-formed and seam welded using an electrical resistance welding (ERW) process to produce tubes which were 63.5 mm (2.5 in) in outside diameter. Due to their higher strength, DP980 tubes were laser welded.

The chemical composition of the steels is listed in Table 5. The three DP steels primarily differ in the level of manganese. Impurity levels of phosphorus and sulphur are very low. The carbon level of DP980 was higher than that of DP600 and P780, in order to obtain higher martensite volume fraction.

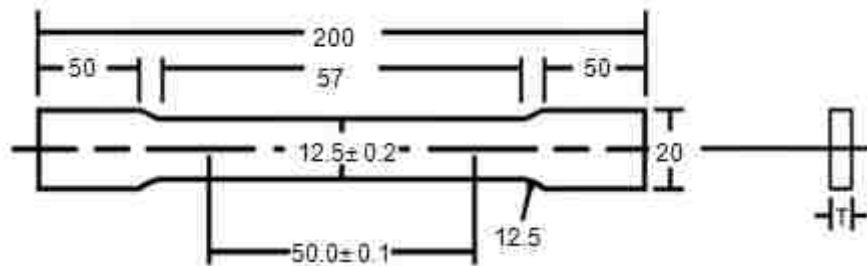
Material	C %	Mn %	P %	S %	Si %	Al %
DP600	0.091	1.01	0.006	0.005	0.309	0.045
DP780	0.104	1.76	0.008	0.004	0.308	0.049
DP980	0.155	1.46	0.007	0.007	0.303	0.045

Table 5: Composition of the investigated steels (Source: Arcelor-Mittal)

## 3.2 Mechanical testing

### 3.2.1 Tensile tests

Tensile specimens were prepared from as-rolled sheets in accordance to ASTM E8-08 as shown in Figure 22. The tensile tests were performed using an ADMET 2613 universal testing machine with a 50kN load-cell capacity. For each grade of steel, the longitudinal, transverse and 45° tensile specimens were pulled at room temperature with a crosshead speed of 0.1mm/sec.



T – Thickness of sheet = 1.2 mm

Figure 22: ASTM E8-08 Standard tension test sheet-type specimens (units in mm)

In addition, due to the significant work hardening in the tube making process, it was necessary to carry out tensile tests on tube specimens. The tube tensile specimens were taken from the tube wall at three locations, i.e. 90°, 180°, and 270°, from the weld seam, as shown in Figure 23. The samples were oriented so that the applied loading axis was parallel with the tube axis, namely, along the rolling direction of the sheet. Tests were performed using traditional flat grips.

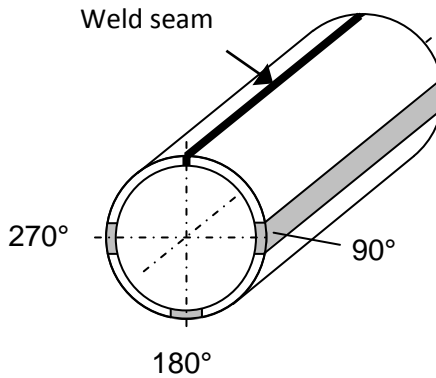


Figure 23: Locations around circumference of tube where tensile tests were taken [69]

### 3.2.2 Tube bending

#### 3.2.2.1 Tube preparation

Prior to the bending process, tubes were cut to the desired length, and electrochemically etched with circle grids (Figure 24), using an in-house electro etching apparatus (Figure 25), for subsequent strain and thickness measurement. The original diameter of each circle was 2.54 mm.



Figure 24: A tube electro-etched with circle grids



Figure 25: Electro-etching apparatus and grid pattern sheet

### 3.2.2.2 Rotary draw bending

At VariForm, an Eagle Precision Technologies electro-hydraulically driven mandrel-rotary draw tube bender (Figure 26), with digital adjustments for different bending parameters, was used to perform all the bending experiments for the investigation. Tubes were bent using standard tools: a bending die, a clamping die and a pressure die. A wiper die was used to avoid wrinkling on the inside of the bend and a flexible 5-ball mandrel was used to minimize the ovality of the tube cross-section during the bending operation [61].

In this work, tubes of each grade of DP steel were bent using three bend ratios (3.1, 2.0, and 1.73). The target bend angle was  $90^\circ$ , and in order to compensate for springback, the actual bending angle on the bender was set higher than  $90^\circ$ . Bending was carried out with a boost pressure of approximately 12.4 MPa and the pressure applied by the pressure die was about 9.0 MPa.



Figure 26: Rotary draw bender



### 3.2.2.3 Strain and thickness measurements

During the bending process, the outside of the bent tube develops tensile stresses and the inside of the bend develops compressive stresses. Upon bending, the circles on the tube surface become elliptical. In order to measure the strain and thickness variation around the tube due to the bending process and evaluate the deformation behaviour, measurement locations were selected in the most deformed region and strains were measured using the Leica MZ8 stereomicroscope as shown in Figure 27.

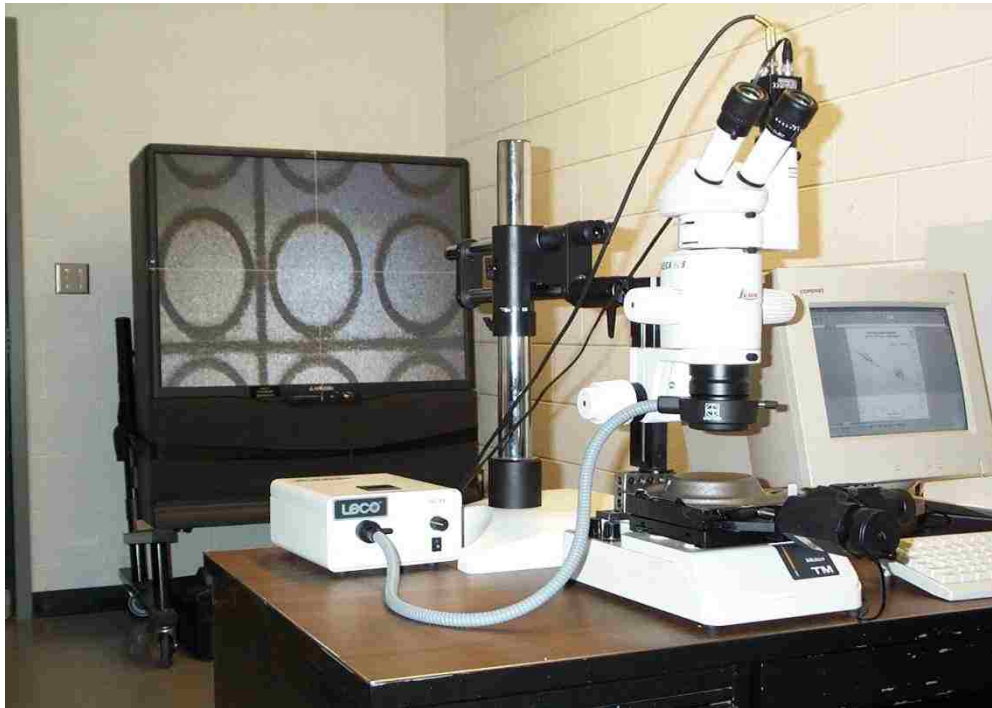


Figure 27: Strain measurement system

Prior to strain and thickness measurements, the tubes were cut into manageable sections (Figure 28). These samples were more easily placed under the microscope used for strain measurement (see Figure 27) and also allowed the tube micrometre to reach all the measurement points.

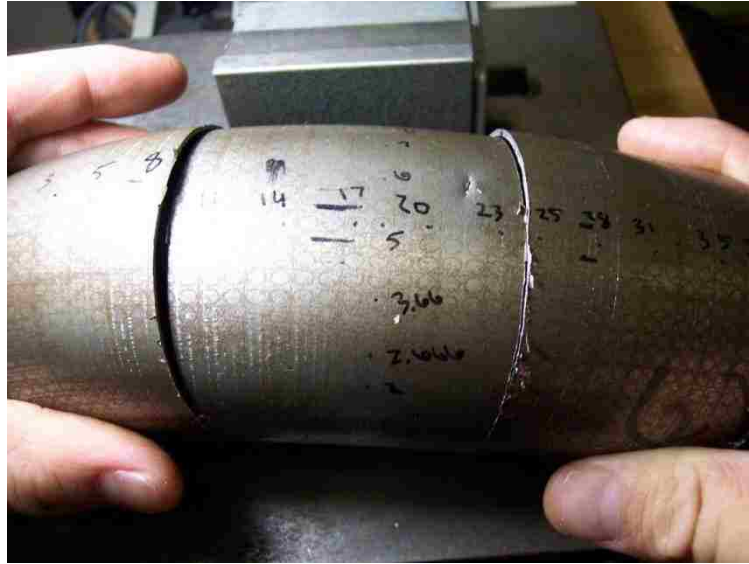


Figure 28: Sections of tube sample and measurement points

After bending, the true strains in the tube wall were determined by measuring the dimension of the distorted grid under a microscope, and the true principal strains were calculated as follows:

$$\varepsilon_1 = \ln \frac{l_1}{l_0} \quad (3-1)$$

$$\varepsilon_2 = \ln \frac{l_2}{l_0} \quad (3-2)$$

$$\varepsilon_3 = \ln \frac{t}{t_0} \quad (3-3)$$

$l_1$  – Length of an ellipse along major axis

$l_2$  – Length of an ellipse along minor axis

$l_0$  – Initial diameter of circles (2.54mm)

$t_0$  – Initial wall thickness of the tube

$t$  – Final wall thickness of the tube

### **3.3 Microstructural analysis**

#### **3.3.1 Specimen preparation**

The specimens, which were approximately 20 mm in length and 12 mm in width, were cut in the rolling direction from various DP steel sheets, straight tubes and bent tubes. They were observed under an optical microscope and the scanning electron microscope (SEM).

Since the specimens were too thin to grip for polishing, they were hot - mounted using a Buehler hot mounting compound in 38.1 mm diameter molds. In general, the hot mounting process takes around 15 minutes at 120-150°C. For each grade of DP steel, specimens in all three-dimensional planes were mounted.

The subsequent metallographic polishing work was divided into three steps in sequence:

1. Specimens were ground using successively finer sand papers (from coarse to fine: 200, 600, 800 and 1200 grit).

2. Specimens were polished using a diamond paste abrasive (9 $\mu$ m) on a nylon-cloth wheel.
3. Specimens were polished with 1 $\mu$ m and 0.05 $\mu$ m alumina powder on micro-cloth wheels.

After polishing, the specimens to be viewed in the optical microscope and SEM were etched with a 2% Nital solution to reveal ferrite grains and martensite islands.

The fracture samples from tensile tests and bending tests were cleaned using an ultrasonic cleaning apparatus.

### **3.3.2 SEM and optical microscopy**

Microstructural characterization of the specimens prior to and after tube bending was done under both an optical microscope and a scanning electron microscope (SEM).

The optical microscope used was a ZEISS AXIOVERT-25 optical microscope which was also used to examine the quality of the polished surface of specimens. The SEM examination and energy dispersive spectrometer (EDS) analysis was conducted using a JEOL JSM-5800LV field emission scanning electronic microscope.

Some specimens with a small examined area, such as the weld seam samples, had to be sputter coated with gold to reduce charging of the mount compound within the SEM.

Fracture specimens were primarily observed on a scanning electron microscope.

### **3.3.3 Metallographic analysis**

#### **3.3.3.1 Measurement of grain size**

Ferrite grain size and length of martensite islands were measured by the lineal intercept method according to ASTM E112-96 (2004).

Considering the greater resolution and magnification, the SEM digital micrographs were mainly used for grain size measurement. These measurements were made using the image analysis software- Image Pro-Plus.

In this study, the microstructure image analysis was performed using the software - Image Pro-Plus, which can be used for image processing, enhancement, and analysis with measurement, threshold, segmentation and customization tools.

#### **3.3.3.2 Measurement of martensite volume fraction and void area fraction**

The martensite volume fraction, the void area fraction and the average void radius were all determined using the analysis software - Image Pro-Plus.

For each DP steel grade, approximately 3 specimens were selected for the measurement of martensite volume fraction using point count methods (ASTM E562-08).

### 3.3.3.3 Measurement of martensite and ferrite deformation

The ferrite grain size and mean length of martensite islands were measured before and after each tube bending test. Thus, the dimensional change of the martensite in each tube bending test was obtained.

By comparing the mean ferrite grain size and the mean length of martensite islands in sheet specimens with those of bent tubes, the martensite and ferrite strain in each test can be calculated. This method was used to estimate the strain in each phase of the DP steels.

### 3.3.3.4 Estimation of martensite carbon content

Prior to evaluating the strength of martensite, it was necessary to estimate the carbon content of martensite.

The carbon content of austenite can be calculated using the lever rule. According to current production methods of DP steels, there is very limited diffusion that takes place during the austenitic transformation. Therefore, the carbon content of the martensite can also be approximately calculated by the lever rule:

$$f_m = \frac{C_0 - C_\alpha}{C_m - C_\alpha} \approx \frac{C_0}{C_m} \quad (3-4)$$

$f_m$  – Martensite volume fraction

$C_0$  – Carbon content of steel

$C_m$  – Carbon content of martensite

$C_\alpha$  – Carbon content of ferrite

(assumed to be 0%, due to the extremely small value)

### 3.4 Correlation and regression analysis [70, 71]

In this investigation, correlation and regression analysis were used to analyze the factors which may affect the deformation behaviour of DP steels.

**Correlation** (often measured as a correlation coefficient, R) indicates the strength and direction of a linear relationship between two random variables. The correlation coefficient between two random variables X and Y, may be shown as:

$$R = \frac{E(XY) - E(X)E(Y)}{\sqrt{E(X^2) - E^2(X)}\sqrt{E(Y^2) - E^2(Y)}} \quad (3-5)$$

E - the expected value operator

The value of R can range from -1 to +1 and is independent of the units of measurement. The correlation is 1 in the case of a positive correlation, -1 in the case of a negative correlation. The closer the coefficient is to either -1 or 1, the stronger the correlation between the variables. If a correlation coefficient is 0, then X and Y are not correlated. They do not have an apparent linear relationship. However, this does not mean that X and Y are statistically independent.

**Regression analysis** refers to techniques for modeling and analyzing several variables when the focus is on the relationship between a dependent variable and one or more independent variables. The regression model is represented by the following equation:

$$y = \sum_{i=1}^n a_i x_i \quad i = 1, \dots, n \quad (3-6)$$

x – The independent variables

y – The dependent variable

a – The unknown parameters

In this research project, based on the experiments and analytical methods described above, further discussion of analysis results will be presented in the next chapter. Figure 29 is a schematic illustration that provides an overview of the main experiments that were carried out and analysis methods used in this project.



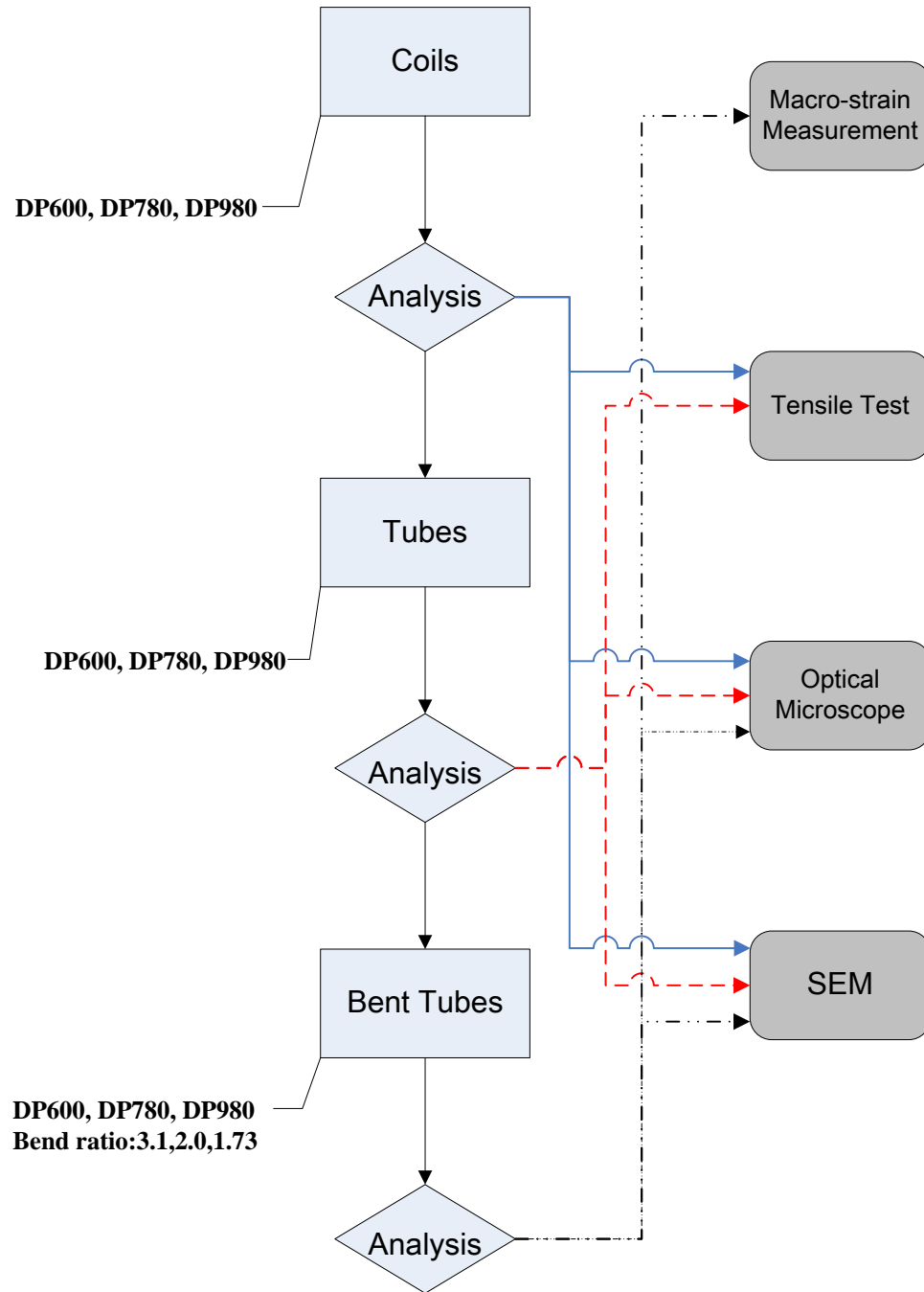


Figure 29: Schematic illustration of the main experiments and analysis

## CHAPTER 4

### RESULTS AND DISCUSSION

#### 4.1 Mechanical testing results

In this investigation, two mechanical tests, tensile tests and rotary draw bending tests, were conducted in order to characterize the deformation behaviour of DP steels.

##### 4.1.1 Tensile testing results

As a common analytical method, tensile tests were performed on as-received flat sheets and on the tubes. The typical engineering stress-strain diagrams for the three DP steel sheets studied are shown in Figure 30 and the mechanical properties of both steel sheets and tubes are listed in Table 6, for comparison.

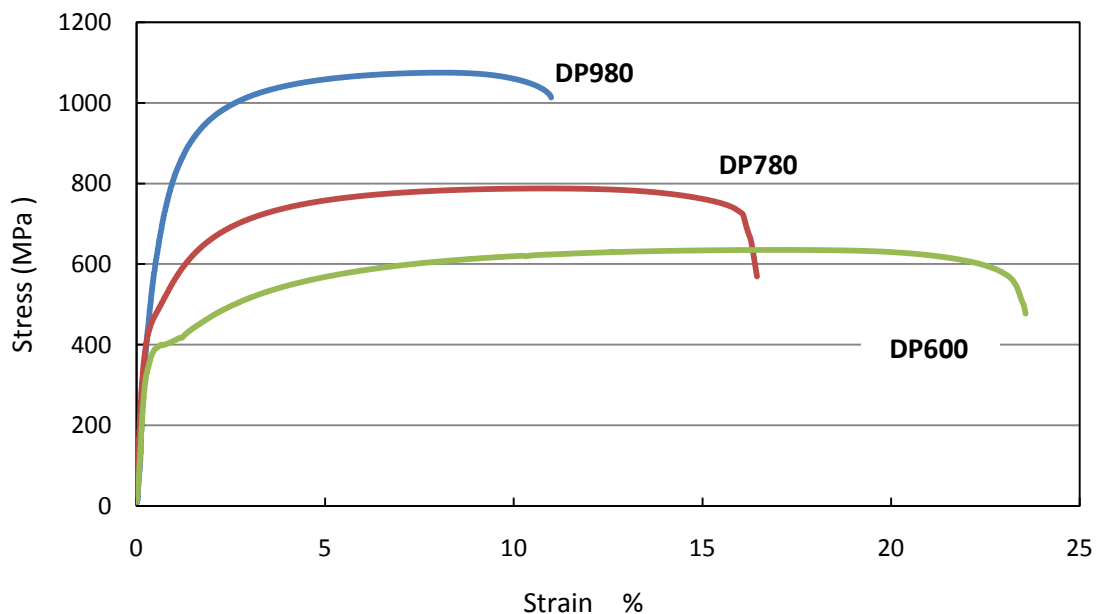


Figure 30: Typical engineering stress-strain curves of DP steel sheets

Material		Number of Samples Tested	Yield Stress MPa	UTS MPa	Yield/UTS	Total Elongation %	n-value (5-10)%	r-value
DP600	Sheet	13	383.6	638.9	0.60	22.0	0.190	1.20
	Tube	6	483.4	661.1	0.70	20.1	0.126	-
DP780	Sheet	13	465.2	795.9	0.58	18.6	0.130	1.00
	Tube	6	606.7	808.9	0.75	17.4	0.094	-
DP980	Sheet	13	622.2	1086.5	0.57	10.8	0.100	0.73
	Tube	6	790.1	1140.2	0.70	8.4	0.075	-

Yield stresses were determined after 0.2% plastic offset

Table 6: Tensile test results of DP steel sheet and tube

Since the volume expansion during phase transformation from austenite to martensite results in many mobile dislocations, in general, DP steels may exhibit deformation behaviour without yield point elongation. As shown in Figure 30, the DP600 steel exhibits yield point elongation like mild steel, due to its microstructure and low martensite volume fraction compared with DP780 and DP980 steels (Table 7).

As shown in Table 7, for the three steel grades, the main differences are the carbon and manganese contents. Since the carbon content controls the hardness of the martensite and the manganese content controls the hardenability of austenite, these two elements can determine the martensite volume fraction of C-Mn DP steels, and thus determine the strength and formability. As described in sections 3.3.3.2 and 3.3.3.4, the martensite volume fraction was measured and the martensite carbon content was estimated and both are recorded in Table 7.

Figure 31 indicates how the martensite volume fraction and the martensite carbon content correlate with the elongation of the three steel grades in this investigation.

Material	C %	Mn %	$f_m$ %	$C_m$ %
DP600	0.091	1.01	<b>12.3</b>	<b>0.74</b>
DP780	0.104	1.76	<b>17.2</b>	<b>0.60</b>
DP980	0.150	1.46	<b>29.2</b>	<b>0.51</b>

Table 7: The microstructural parameters and main chemical composition of DP steels

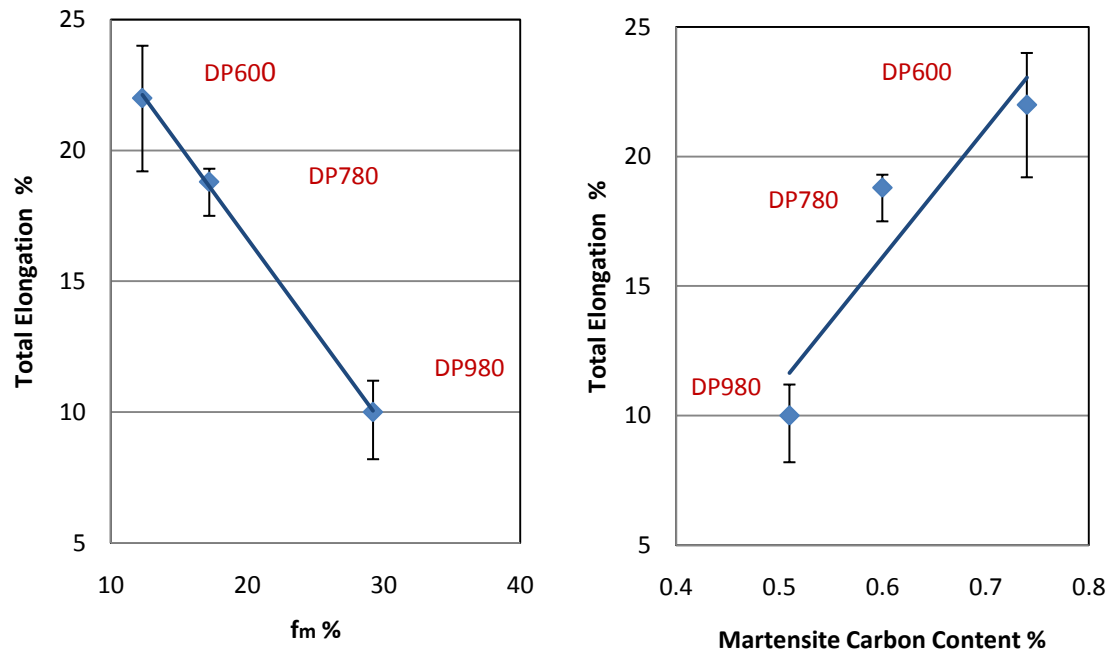


Figure 31: The Influence of martensite volume fraction and martensite carbon content on total elongation of C-Mn DP steels.

#### 4.1.2 Rotary draw bending results

In this study, for each steel grade, tube bending trials using different bend ratios were conducted at VariForm. Table 8 describes the bending test results. Due to the strength and bendability of the three steel grades, each steel grade has a minimum bend ratio in the rotary draw bending process as shown in Table 8.

Steel Grade	Wall Thickness (mm)	Outer Diameter (mm)	Bend Ratio (R/D) 3.1		Bend Ratio (R/D) 2.0		Bend Ratio (R/D) 1.73	
			Number of Tubes Bent	Results	Number of Tubes Bent	Results	Number of Tubes Bent	Results
DP600	1.2	63.5	12	Success	8	Success	<b>8</b>	<b>1 Failed</b>
DP780	1.2	63.5	12	Success	<b>8</b>	<b>5 Necked</b>	6	5 Failed
DP980	1.2	63.5	<b>8</b>	<b>Success</b>	6	5 Failed	-	-

Table 8: Results of rotary draw bending tests at VariForm

In the rotary draw bending tests, axial, hoop and thickness strains, which are defined as shown in Figure 32, were measured. As mentioned in Appendix A, since the hoop strain  $\varepsilon_2$  is small compared with the axial strain  $\varepsilon_1$  and thickness strain  $\varepsilon_3$ , hoop strain  $\varepsilon_2$  can be neglected. Figure 32 shows the axial and thickness strain distributions along the outside of the bend for the three steel grades and for the same bend ratio. The higher curves represent the axial strain distribution and the lower curves represent the thickness strain distribution along the outside of the bent tube. Figure 32 indicates that for the same bend ratio, the axial strains are practically the same for all steel grades. The maximum strain occurs at the clamp side of the tube, since this is where the first bending impulse

is applied to activate the bending process. The maximum axial strain in a rotary draw bending process depends on bending process parameters such as lubrication, bending speed and mandrel position etc. In Figure 32, the strains in the steady state region are considered to be the average strain of the bent tube. Figure 33 displays typical axial and thickness strain distributions of the same steel grades (DP780) along the outside of the bend for different bend ratios. It can be seen that the axial strains, which represent the deformation of DP steel tube, increase with decreasing bend ratio.

As shown in Figure 34, since the bent tube exhibits tensile strains along the outside of the bend in the axial and thickness directions, the axial and thickness strains at this location are considered the critical or limiting strain when analyzing the deformation behaviour of bent tubes and predicting the onset of failure. Figure 34 shows the strain distribution around the circumference.

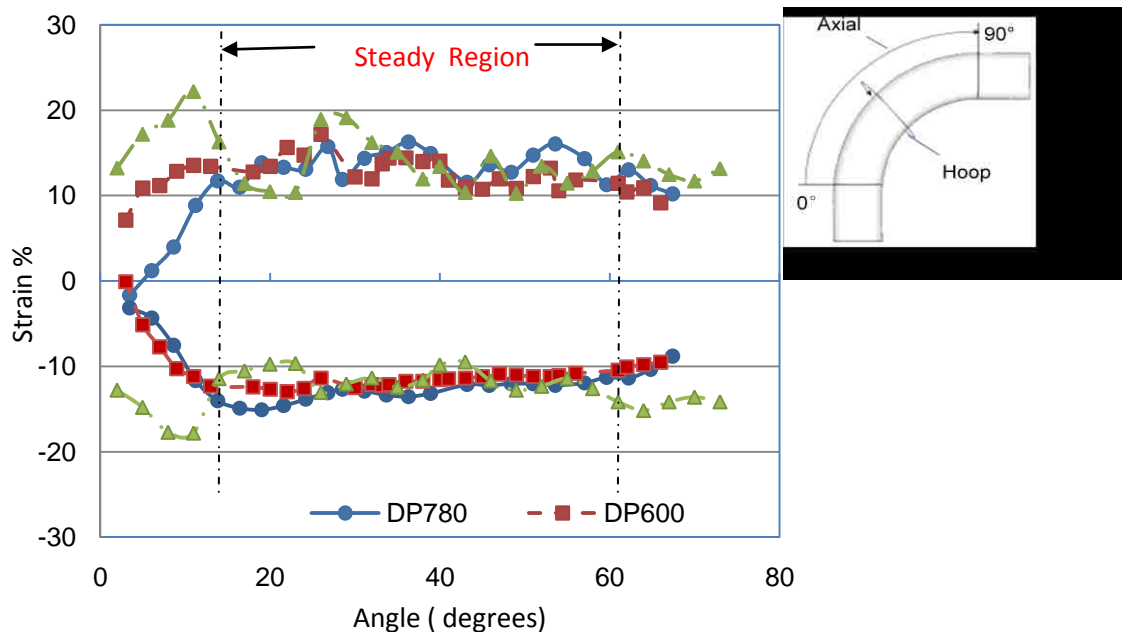


Figure 32: Axial and thickness strain distributions along the outside of bent tubes (bend ratio = 3.1)

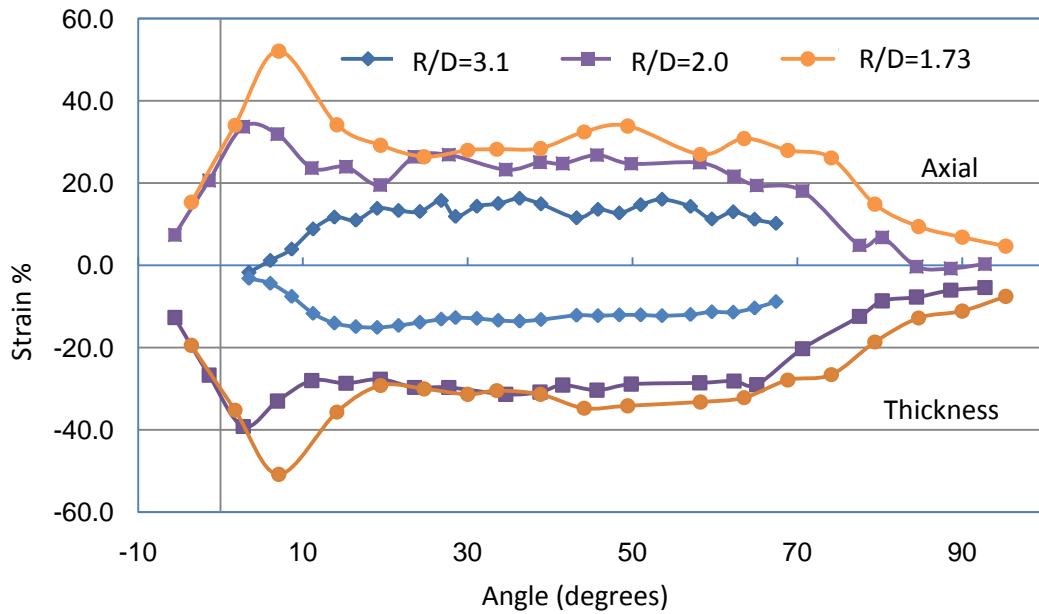


Figure 33: Axial and thickness strain distributions along the outside of bent tubes (DP780)

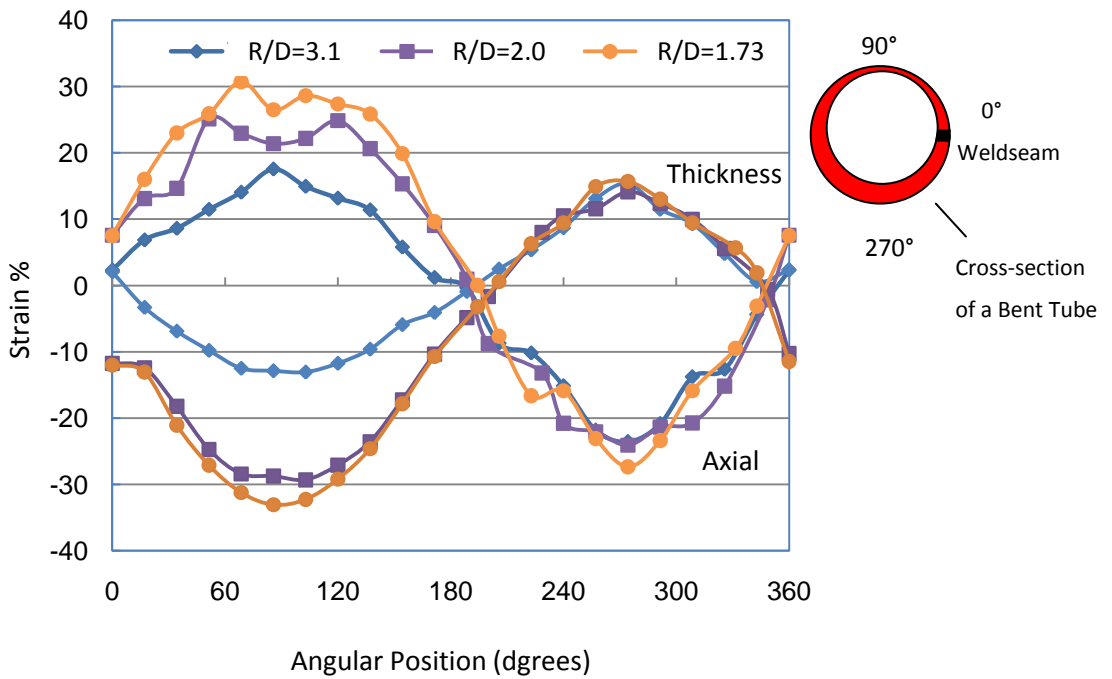


Figure 34: Axial and thickness strain distributions around the circumference of bent tubes (DP780)

Table 9 lists the measured average axial strain (in the steady state region) and the calculated strain along the outside of the bend of C-Mn DP steel tubes bent with different bend ratios. The calculated strain was determined using Equation (2-9).

Steel Grade	Axial Strain (True Strain)								
	Bend ratio 3.1			Bend ratio 2.0			Bend ratio 1.73		
	Number of Bent Tubes Measured	Average	Calculated	Number of Bent Tubes Measured	Average	Calculated	Number of Bent Tubes Measured	Average	Calculated
DP600	6	0.146		4	0.252		<b>3</b>	<b>0.316</b>	
DP780	6	0.152	0.176	<b>3</b>	<b>0.267</b>	0.288	1	0.328	0.341
DP980	<b>2</b>	<b>0.157</b>		-	-		-	-	

Table 9: True axial strain of bent tubes of different DP steel grades



## 4.2 Effect of martensite banding and possible solutions

As mentioned in Chapter 2, martensite banding (Figure 35) of C-Mn DP steels is caused by manganese segregation during dendritic solidification. The banding is then stretched along the rolling direction by subsequent deformation. As a result, martensite banding is one of the most important microstructural features that influence the deformation behaviour of DP steels. In this chapter, the effects of martensite banding are discussed in terms of the tensile test results and microstructural analysis, and some possible solutions for reducing extent of martensite banding are presented.

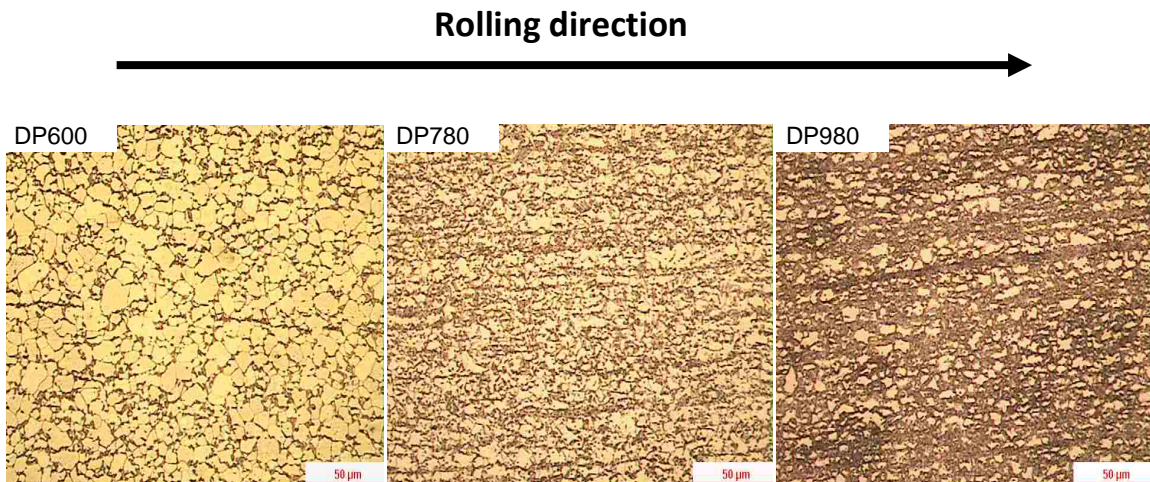


Figure 35: Martensite banding in different DP steel grades  
(optical micrographs of sheet samples)

#### 4.2.1 Quantitative measure of martensite banding

To describe and characterize the extent of martensite banding in DP steels, the ASTM E1268-01 standard was used. In order to compare and confirm the results, another method was also used: banding length density. The longitudinal view micrographs (Figure 35) of the samples for all steel grades were used to measure and estimate the severity of martensite banding.

- **ASTM E1268-01**

$$AI = NL_{\perp} / NL_{\parallel} \quad (4-1)$$

$$NL_{\perp} = N_{\perp} / L \quad (4-2)$$

$$NL_{\parallel} = N_{\parallel} / L_t \quad (4-3)$$

AI – Anisotropy index, for a non-banded structure, AI has a value of one,

$N_{\perp}$  – Number of feature interceptions with test lines perpendicular to the rolling direction

$L_t$  – Test line length in mm

$N_{\parallel}$  – Number of feature interceptions with test parallel to the rolling direction lines

- **Banding length density [72]**

$$\rho_L = \frac{\sum_{i=1}^N L_i}{S} \quad (4-4)$$

$\rho_L$  – Banding length density

$L_i$  – Martensite banding length ( $L_i \geq 50 \mu\text{m}$ )

S – Area of measured field

Both indices, the anisotropy index (AI) and the banding length density ( $\rho_L$ ) provide a quantified measure of martensite banding. These are shown in Table 10 for each steel grade.

Steel Grade	NL $\perp$ (No./mm)	NL// (No./mm)	AI (NL $\perp$ /NL//)	$\rho_L$ ( $\mu\text{m}/\mu\text{m}^2$ )	Mn (%)
DP600	162.0	141.1	<b>1.15</b>	<b>0.004889</b>	1.01
DP780	174.6	125.4	<b>1.39</b>	<b>0.059519</b>	1.76
DP980	150.3	117.0	<b>1.28</b>	<b>0.054073</b>	1.46

Table 10: Measures of martensite banding in each DP steel

As shown in Table 5 (Section 3.1), the three C-Mn DP steels mainly differ in their manganese and carbon content. The phosphorus and sulphur contents are very low. Since the carbon diffusion rate is several orders of magnitude higher than the manganese diffusion rate [8, 9, 73, 74], the carbon diffusion in C-Mn DP steels reaches equilibrium almost immediately in the intercritical annealing process, while the manganese diffusion may take more than twenty hours to reach equilibrium [75]. Thus, manganese segregation in Austenite cannot be eliminated during the normal C-Mn DP steel production process. Since manganese lowers the A3 temperature and suppresses ferrite growth in the intercritical annealing process for C-Mn DP steels, martensite formation is promoted in Mn-rich regions. Therefore, as shown in Table 10 and Figure 36, the

extent of martensite banding in C-Mn DP steels is primarily influenced by the manganese content.

From Table 10, it is evident that martensite banding increases with the manganese content of DP steels. Figure 36 also shows these same observations. Both measurement techniques - anisotropy index and banding length density show the same tendency, and this has also been observed by other researchers [76,77]. It is therefore not surprising that DP780 steel has more severe martensite banding than DP980 steel due to its higher manganese content.

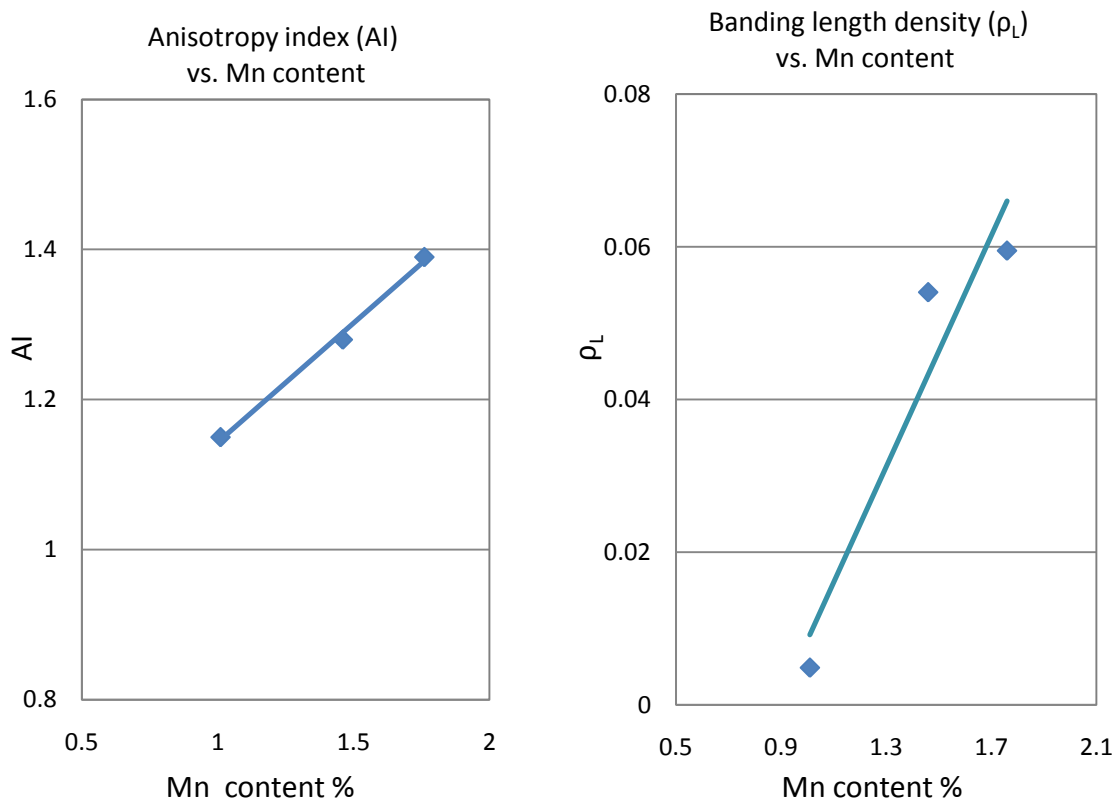


Figure 36: Effect of Mn content on martensite banding

#### 4.2.2 Effect of martensite banding on tensile properties

In this research, tensile tests were conducted in the longitudinal (rolling) and transverse directions for each grade of DP steel. The average mechanical properties are listed in Table 11.

Steel Grade	Orientation	Number of Samples Tested	0.2% Yield MPa (Average)	UTS MPa (Average)	Total Elongation % (Average)
DP600	Longitudinal	5	370.9	630.1	23.2
	Transverse	5	379.6	640.4	22.6
DP780	Longitudinal	5	468.8	799.1	18.5
	Transverse	5	475.8	796.9	17.5
DP980	Longitudinal	4	585.5	1088.5	11.3
	Transverse	4	642.9	1087.0	8.6

Table 11: Average mechanical properties for C-Mn DP steel sheets

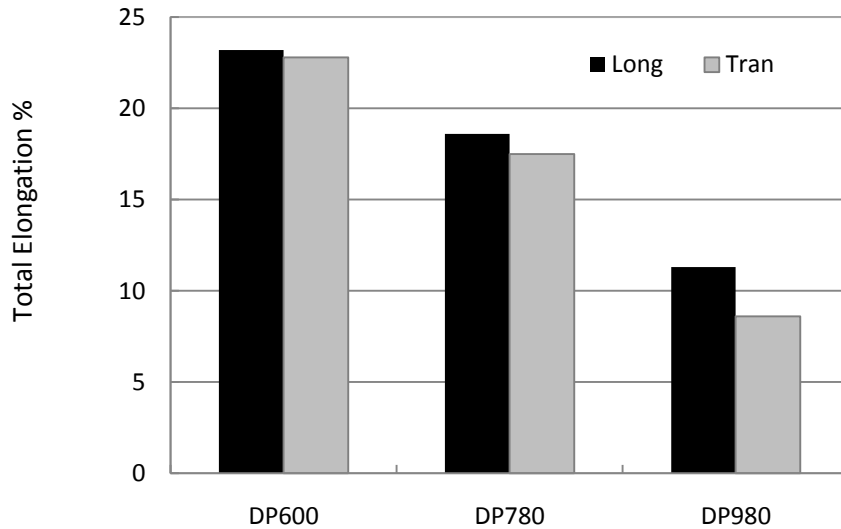


Figure 37: Total elongation of each steel grade in different orientations

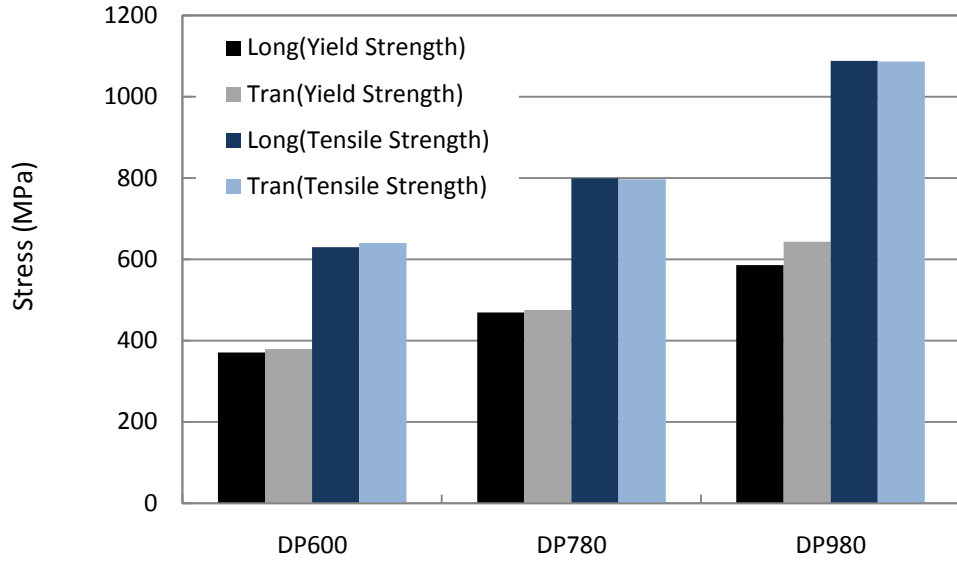


Figure 38: Yield and tensile strength of each steel grade in different orientations

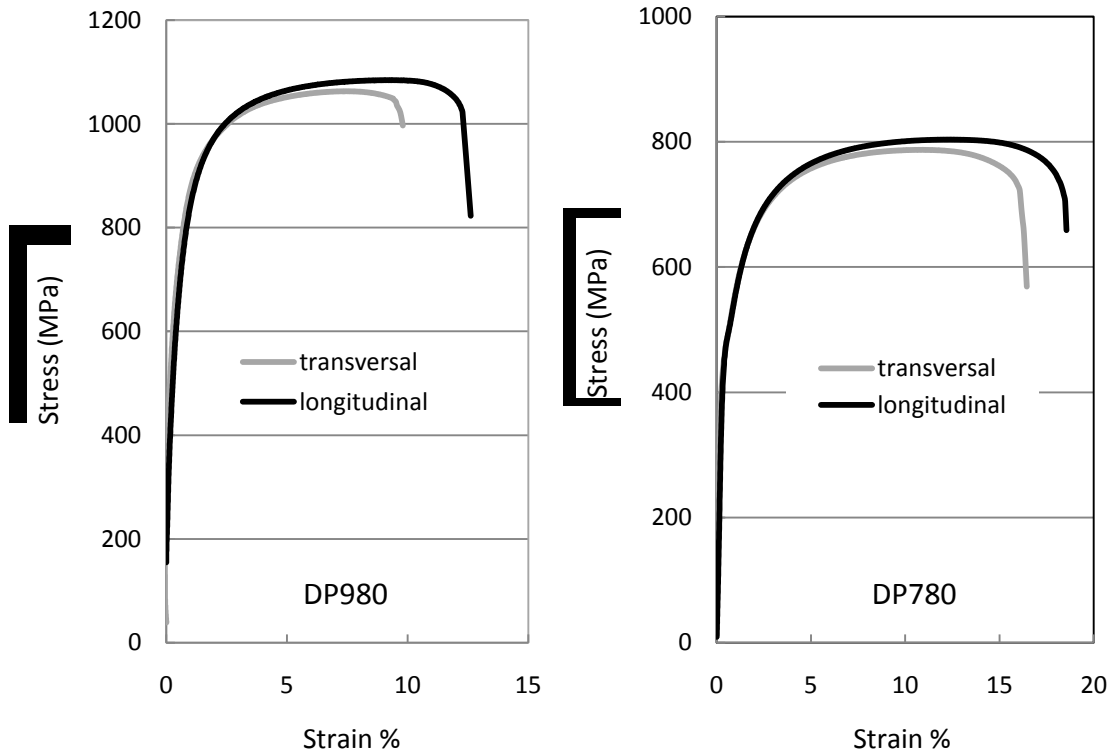


Figure 39: Typical engineering stress-strain curves for DP780 and DP980 steel sheets

As shown in Table 11, Figure 37 and Figure 38, in DP780 and DP980, the strength properties in both directions are almost identical except that, for the DP980, the yield stress and the total elongation in the rolling direction are greater than in the transverse direction. For DP600, the difference in strength and elongation between the longitudinal and transverse directions is also modest. Figure 39 shows the engineering stress-strain curves for DP780 and DP980 in both the longitudinal and transverse directions.

In terms of the tensile testing results in this project, there is no evidence that martensite banding influences the strength of the steel, but it appears to have some effect on elongation. The exception is that the yield strength of DP980 in the transverse direction is much greater than in the longitudinal direction. Because the higher martensite volume fraction (MVF) of DP980 results in a smaller ferrite mean free path (MFP), i.e. the mean distance between ferrite/martensite phase boundaries measured in the ferrite, in the transverse direction (Table 12), the ferrite grains of DP980 in the transverse direction require more energy to be deformed during yielding than those in the longitudinal direction. In addition, the strength and elongation of DP600 in both directions is nearly the same, due to the limited extent of martensite banding compared with the other two steel grades, and the similar mean free path in the longitudinal and transverse directions as shown in Table 12.

In Table 12, the ratio of the longitudinal to transverse mean free path (L/T-MFP) correlates very well with the equivalent yield stress or elongation ratios and appears to characterize the anisotropy of these materials. Because the ratio of mean free path in C-Mn DP steels is affected by many factors, such as metallurgical production parameters and microstructural features, the deformation

behaviour of DP steels is also influenced by these factors, and not solely by martensite banding. This may explain why DP980 exhibits more anisotropy in mechanical properties than DP780 although the anisotropy index of DP780 is higher than that of DP980.

Steel Grade	MFP in Longitudinal Direction ( $\mu\text{m}$ )	MFP in Transverse Direction ( $\mu\text{m}$ )	L/T (MFP)	$f_m$ %	AI	L/T (Elongation)	L/T (Yielding strength)
DP600	6.05	5.89	<b>1.03</b>	12.3	1.15	<b>1.02</b>	<b>0.98</b>
DP780	5.87	5.04	<b>1.16</b>	17.2	1.39	<b>1.06</b>	<b>0.99</b>
DP980	6.38	4.68	<b>1.36</b>	29.2	1.28	<b>1.31</b>	<b>0.91</b>

Note: L - Longitudinal direction      T - Transverse direction      MFP - Mean free path

Table 12: Mean free path of ferrite grains and martensite volume fraction of C-Mn DP steels in different steel grades

Even though severe banding may affect the anisotropy of tensile properties and enable cracks to propagate without being blunted by the surrounding ferrite matrix and martensite islands, it should be noted that anisotropy of mechanical properties in C-Mn DP steels are also related to two other microstructural features: crystallographic texture and elongated inclusions. Texture is the non-random distribution of crystal orientations in a polycrystalline material. However, texture has little effect on the onset of the failure during the deformation, nor does it create



sites for void nucleation as does the presence of banding and inclusions. Therefore, the effect of texture was not considered in this investigation. Deformed inclusions seem to exhibit more incompatibility with the ferrite matrix than with the martensite in DP steels. Thus elongated inclusions may play a more important role in the anisotropy of mechanical properties in C-Mn DP steels, as will be described in more detail in section 4.3. However, since different batches of DP steels may have different amounts and types of inclusions, it is difficult to identify whether the elongated inclusions or the martensite banding, plays a greater role in the anisotropy of DP steel. Some researchers [72] have found that banding can significantly affect the anisotropy of mechanical properties, while others [78] insist that banding has very little effect on anisotropy of tensile properties. Therefore, the severity of martensite banding may just be one of the microstructural features that can influence the anisotropy of mechanical properties in C-Mn DP steels.

Furthermore, unlike elongated inclusions which may be distributed uniformly throughout steel sheets, martensite banding of C-Mn DP steels mainly affects the central region (i.e. the centre of the sheet in relation to the through-thickness direction: Figure 40) due to dendritic solidification. Thus, elongated inclusions, rather than martensite banding, may be responsible for surface cracks during further deformation such as tube bending.

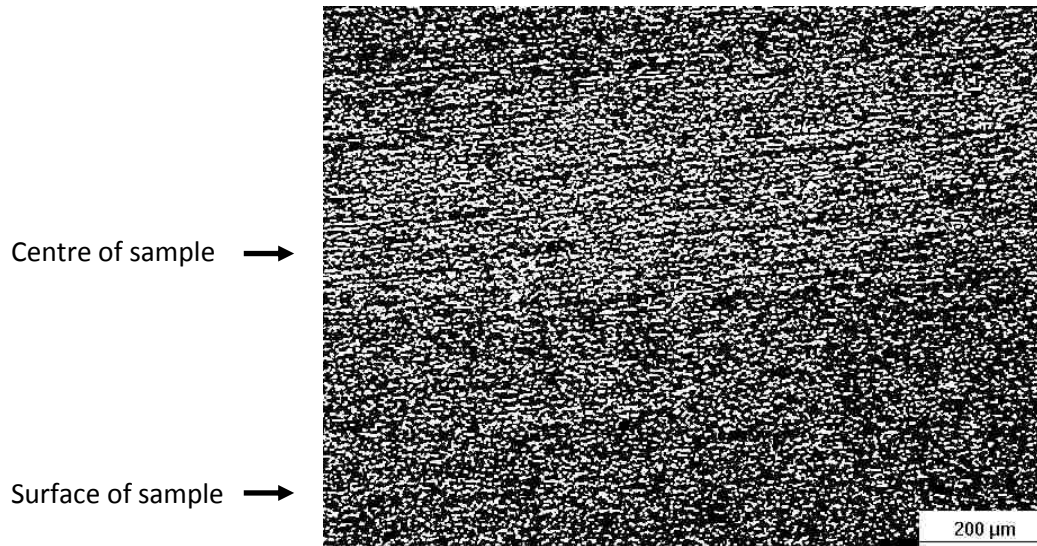


Figure 40: Optical micrographs of martensite banding distribution in cross-section direction of a DP steels sample (thickness: 1.2mm)

#### 4.2.3 Possible solutions

The morphology of martensite banding appears to primarily influence the total elongation of C-Mn DP steels, since cracks can easily propagate along the martensite/ferrite boundaries and lead to decohesion of the martensite/ferrite interface. Measures to avoid or reduce martensite banding during the strip production process are effective to increase the formability of C-Mn DP steels.

- **Casting**

Maintaining a low superheat casting and increasing the cooling rate of the secondary cooling system may reduce alloy segregation, namely the gradients in alloy content, during dendritic solidification.

- **Rolling**

1. In the soaking furnace, increasing the heating time and temperature as much as possible can help to promote manganese diffusion, although it will be far from the time required for austenite to reach equilibrium.
2. In the hot rolling mill, increasing the thickness reduction, i.e. increasing slab thickness or decreasing sheet thickness, can reduce the space between Mn-rich zone and Mn-lean zone, and then the austenite may be more uniform.
3. In the cooling area of the hot rolling or continuous annealing process, increasing the cooling rate can suppress carbon diffusion, and reduce, or even eliminate, martensite or pearlite banding. Nevertheless, the chemical composition segregation still exists. Subsequent heat treatment with slow cooling rate may result in the reappearance of microstructural banding.

In summary, it is difficult to eliminate all martensite banding in the normal C-Mn DP steel producing process, but the above measures may help to reduce it. Moreover, thin slab continuous casting and rolling plants lead to less alloy segregation compared with conventional casting and rolling plants [79]. Therefore, selecting DP steel coils, which are produced from thin slabs, may increase the quality and formability in further deformation processes, such as bending and hydroforming.

### **4.3 Failure analysis**

In terms of the microstructure and failure analysis results, the effects of inclusions and void nucleation and propagation on DP steel tube bending are presented in this section.

#### **4.3.1 Non- metallic inclusions**

By definition, non-metallic inclusions are chemical compounds which are present in the steel and create inhomogeneities in the microstructure [80]. In general, non-metallic inclusions have an adverse effect on the mechanical properties of the steel, because they promote void formation, and cause material defects, and fractures.

In this investigation, many inclusions were found in the C-Mn DP steel samples using scanning electronic microscope (SEM). Results from the energy dispersive spectrometer (EDS) analyse show that the inclusions are mainly composed of sulfides, and oxides, and include the following elements: Al, Mn, Si, S, Ca, N, O. Depending on their chemical composition, deformation behaviour and shape, the non-metallic inclusions that were observed in this work can be divided into two types:

- Ductile sulfide inclusions (stringers)
- Hard oxide inclusions (globular)

#### 4.3.1.1 Ductile sulfide inclusions (stringers)

Compared with other non-metallic inclusions, sulfide inclusions, especially manganese sulfide and calcium sulfide, are elongated along the rolling direction during hot and cold rolling. The incompatibility of mechanical properties and the weak interface between the matrix and the inclusion promote void nucleation and propagation. Furthermore, the sulfide inclusions elongated in stringer shapes supply additional spaces where microvoids may nucleate.

In subsequent deformation processes (bending, hydroforming), sulfide inclusions develop into a series of microvoids that look like a dotted line (Figure 41) along the rolling direction. The sample in Figure 41 was taken from the outside of the bend of a DP780 steel tube. Figure 42 and Table 13 show, respectively, the EDS analysis and the chemical composition of the area indicated by the arrow in Figure 41. The EDS analysis indicates that the inclusions are mainly sulfides.

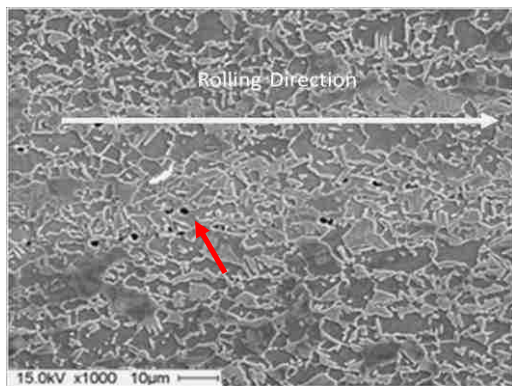


Figure 41: Microvoids caused by sulfide Inclusions (after bending)

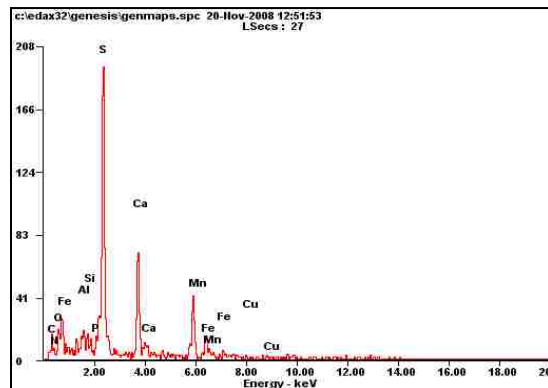


Figure 42: The EDS analysis graph (area of analysis indicated by the arrow in Figure 41)

With an increase in strain during further deformation, these microvoids may grow, coalesce and form cracks along the rolling direction, and ultimately, lead to failure.

<b>Element</b>	<b>Weight%</b>	<b>Atom%</b>
<b>C</b>	08.22	21.94
<b>O</b>	05.13	10.28
<b>Al</b>	02.27	02.70
<b>Si</b>	00.65	00.75
<b>P</b>	01.18	01.22
<b>S</b>	27.40	27.39
<b>Ca</b>	16.91	13.53
<b>Mn</b>	26.08	15.22
<b>Fe</b>	12.15	06.98

Table 13: Chemical composition of a sulfide inclusion  
(area of analysis indicated by the arrow in Figure 41)

In the tube bending trials, a surface crack was found (Figure 43). The fracture surface was observed under the scanning electron microscope (Figure 44), and the EDS analysis (Figure 45) revealed that the area inside the rectangle (see Figure 44) has a high sulfur concentration. As mentioned in section 4.2, elongated sulfide inclusions rather than martensite banding may be one of the primary causes of surface cracks in DP steels due to their random distribution.



Figure 43: Surface crack on a bent tube

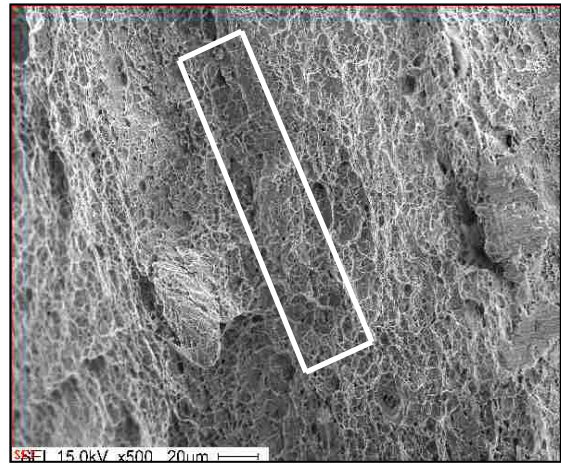


Figure 44: Fractograph of the surface crack

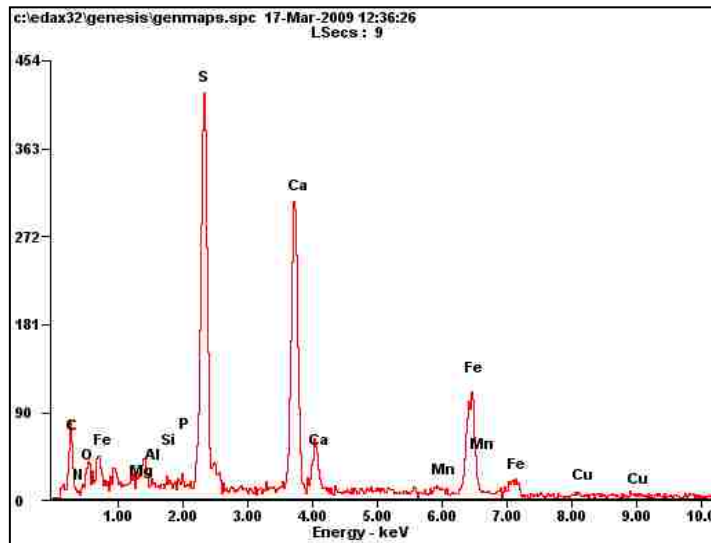


Figure 45: The EDS analysis graph  
(area of analysis indicated by the rectangle in Figure 44)

#### 4.3.1.2 Oxide inclusions (globular)

In C-Mn DP steels, oxide inclusions are mainly aluminum and calcium oxides. Because of their hardness these oxides break apart into several smaller particles or keep their original size and globular shape (Figure 46) after hot and cold rolling. Figure 47 and Table 14 display the EDS analysis results for the globular inclusion shown in Figure 46 and show that it is an aluminum oxide.

In the bending and hydroforming processes, with an increase in strain, oxide inclusions can cause decohesion cracks around the inclusion particles, due to the dissimilar elongations between the ferrite matrix and inclusions. However, compared to sulfide stringers, globular oxide inclusions cause comparatively few microvoids to nucleate. As a result, the limited quantity of oxide inclusions only has a modest effect on DP steel properties compared with sulfide inclusions.

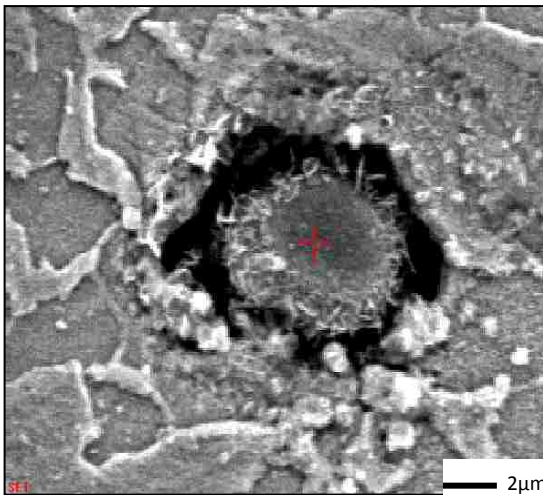


Figure 46: Oxide inclusion in C-Mn DP steels  
(after Bending)

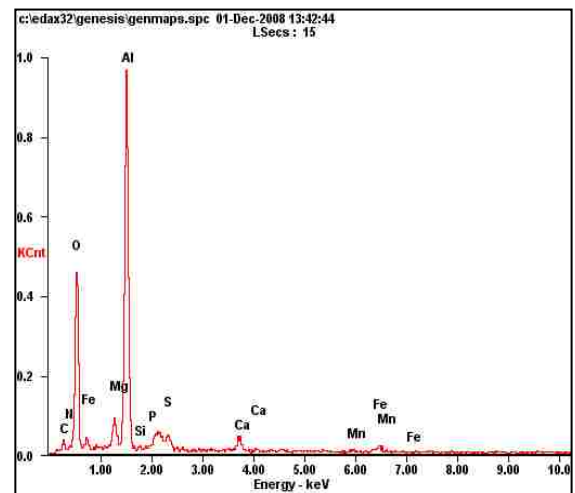


Figure 47: The EDS analysis graph (area of analysis indicated by the cross in Figure 46)



<b>Element</b>	<b>Weight%</b>	<b>Atom%</b>
<b>C</b>	06.17	10.63
<b>N</b>	03.11	04.59
<b>O</b>	35.46	45.83
<b>Mg</b>	02.89	02.46
<b>Al</b>	39.47	30.26
<b>Si</b>	00.00	00.00
<b>P</b>	01.86	01.24
<b>S</b>	01.90	01.22
<b>Ca</b>	02.57	01.33
<b>Mn</b>	01.50	00.57
<b>Fe</b>	05.06	01.88

Table 14: Chemical composition of an aluminum-oxide inclusion  
(area of analysis indicated by the cross in Figure 46)

#### 4.3.1.3 Sources of inclusions and possible solution

All steels contain non-metallic inclusions to a greater or lesser extent. Since sulfide and oxide inclusions negatively affect the forming behaviour of DP steel, it is critical that the steel making and casting plant determine the source of inclusions and reduce them. Although the optimization of steel making is outside the scope of this research, the present EDS analyses and published investigations [81-83] indicate that these inclusions may originate from three non-metallic sources:

- Refractory materials
- Slag
- Deoxidation products

Obviously, all the inclusions were formed during the processing before the soaking furnace and there are many factors that can affect the inclusion content in the final rolled product. This may explain why different tubes from the same batch of C-Mn DP steel can exhibit very different deformation behaviour during rotary draw bending even though they have very similar mechanical properties.

Generally, manufacturers have virtually no information about the steel production process, and consequently, it is difficult to determine the quantity of inclusions in a particular coil or tube.

However, fabricators of steel products can still minimize the risks that inclusions present. Because the first and last slab in a heat are cast in unstable conditions, it is therefore prudent to avoid selecting these coils. This may reduce the down-stream risk of using coils with higher levels of inclusions.

### 4.3.2 Damage mechanisms and void formation

#### 4.3.2.1 Fractographs of the failures in tube bending tests

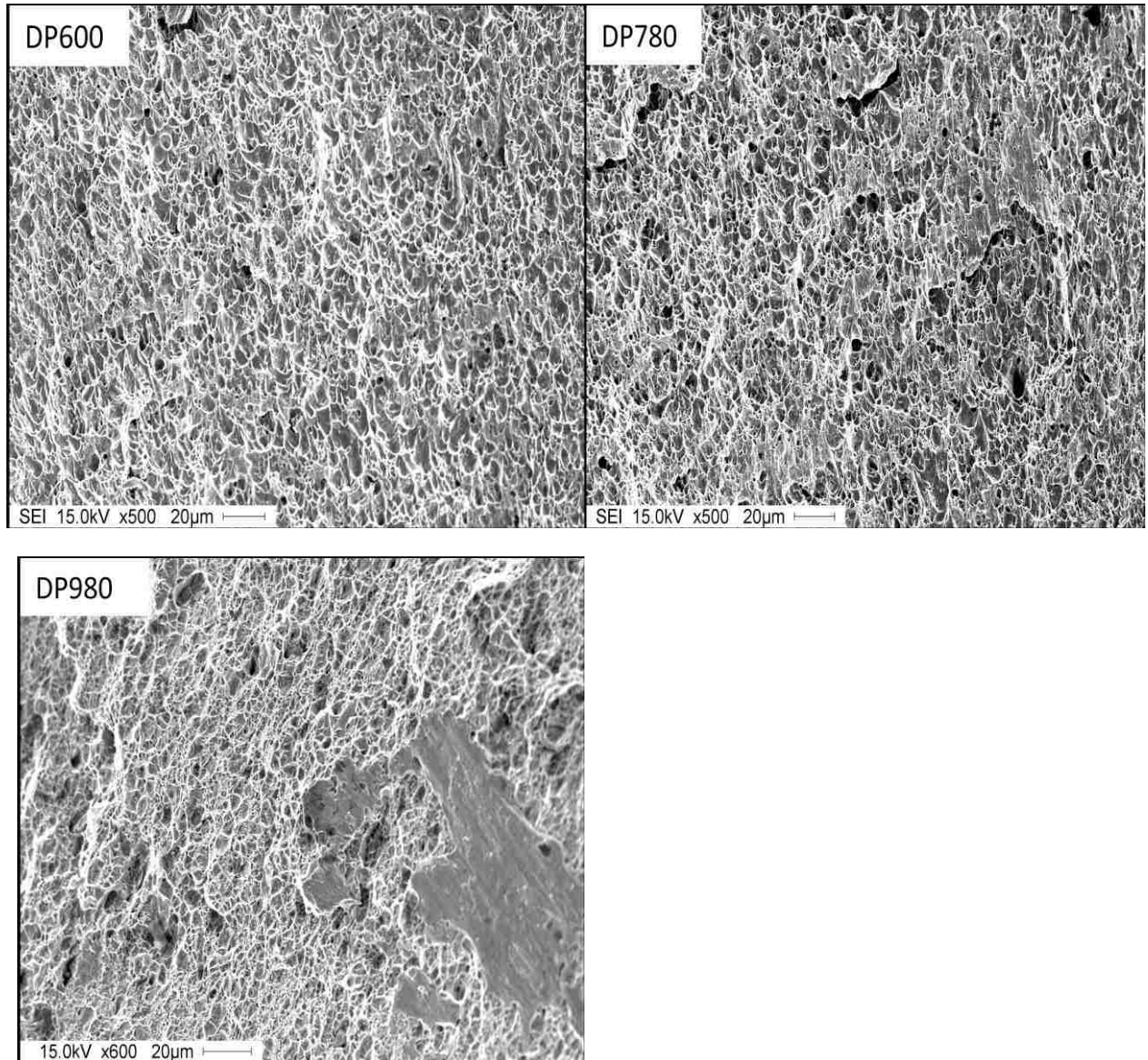


Figure 48: SEM fractographs for the three grades of DP steel

As shown in Figure 48, the fracture mechanism appears to change from ductile fracture to mixed fracture (i.e. quasi-cleavage and ductile fracture) with an increase in tensile strength (from DP600 to DP980).

According to the fractographs of C-Mn DP steel (Figure 48), the appearance of fractures can be described as follows:

Steel Grade	Dimples		Cleavage Facets		Fracture Behaviour
	Amount	Size	Amount	Size	
DP600	Many	Big	Very Few	Small	Ductile
DP780	Few	Big	Few	big	Ductile
DP980	Very Few	Relatively small	Many	Very big	Ductile and quasi-cleavage

Table 15: Description of fracture surfaces for the three grades of DP steel

Ductile fracture is preceded by substantial plastic deformation. Because DP steels contain a hard phase (martensite) and inclusions that do not deform at the same rate as the ferrite matrix, voids are nucleated to accommodate the incompatibility. The nucleation, growth and coalescence of voids may lead to fracture of the martensite or inclusion, or decohesion at the ferrite/martensite interface or the inclusion/ferrite interface. At the fracture surface, most areas have the appearance of 'dimples', and each dimple corresponds to a void that existed prior to failure. Inclusions that are responsible for nucleating a void can frequently

be observed at the bottom of the dimples. As a result, a greater martensite volume fraction and inclusion content causes smaller dimples due to the restricted void growth and coalescence. As described in Table 15, with the increase of martensite volume fraction in the three grades of DP steels, the decrease of ductility is accompanied with larger and more cleavage facets, and consequently the number of dimples decreases.

As mentioned before, the quasi-cleavage fracture can be interpreted as a transition fracture mechanism between ductile and brittle fracture (see section 2.3), therefore, it is not surprising to find quasi-cleavage fracture in DP980 samples.

#### **4.3.2.2 Observation of void nucleation and propagation in bent tubes**

As reported in others investigations [84-87], ductile fracture occurs in five sequential stages: void nucleation, void growth, void coalescence, crack formation and failure. In this investigation, C-Mn DP steel tubes deformed in bending trials exhibited mainly ductile fracture behaviour, as shown in the previous section. The micrographs of bent tube samples display the same evolution of microstructural damage, as shown in Figure 49.

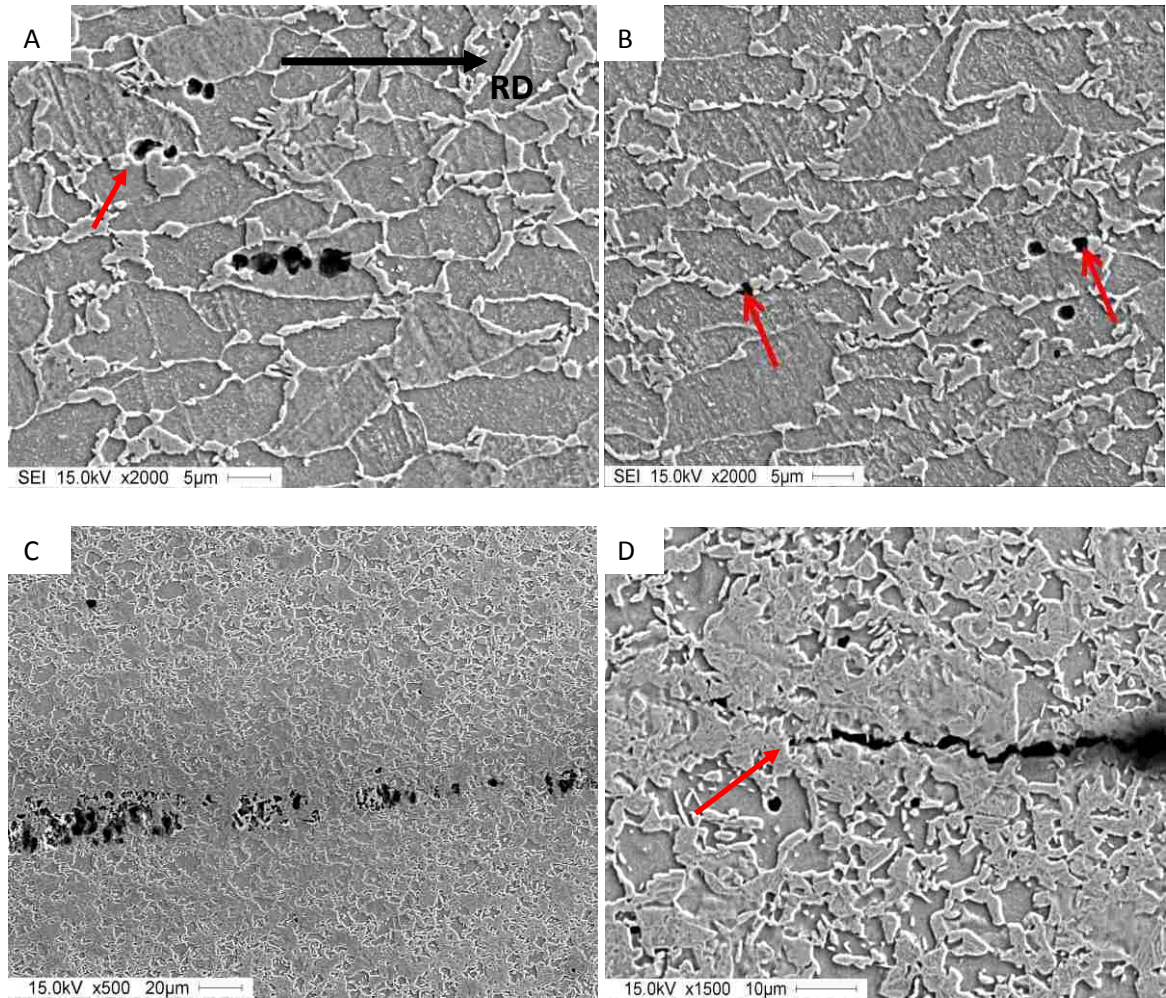


Figure 49: Void nucleation and propagation (samples from bent tube)

- A:** Void nucleation and coalescence in the ferrite matrix;    **B:** Martensite decohesion  
**C:** Voids caused by Inclusions (sulfide);                      **D:** Crack is blocked by martensite

Figure 49 A shows voids that nucleated at the interface between the martensite and the ferrite. Voids can initiate in the low strain stage because of the incompatibility between martensite and ferrite. Subsequently, the voids grow and coalesce as shown in the centre of Figure 49 A. In spite of its high strength and

low elongation, martensite also participates in the plastic deformation through decohesion. Cingara et al. [88] show that martensite decohesion can occur at low strain at an early stage of deformation. Voids resulting from martensite decohesion are seen in Figure 49 B. As a result, martensite cracking promotes void nucleation and propagation. The extent and amount of martensite cracking is related to the carbon content and strength ratio of the martensite in DP steels. During void growth and coalescence, cracks are formed and may cause failure. During crack propagation, a crack may be blocked by martensite, as shown in Figure 49 D.

In addition to the microstructural damage described above, a large number of voids caused by sulfide inclusions were also observed after the bending tests (Figure 49 C). Comparing the numbers and concentration of voids in Figure 49 C with those in other figures, the elongated sulfide inclusions are seen to cause void coalescence and crack formation more quickly.

In a bent tube that fractured (Figure 50), voids were concentrated in the centre of the strip where martensite banding occurs. Inclusions were not found in the dimples. This is consistent with the analysis that severe martensite banding can cause increased void nucleation and promote void coalescence along the martensite/ferrite interface as discussed in section 4.2.

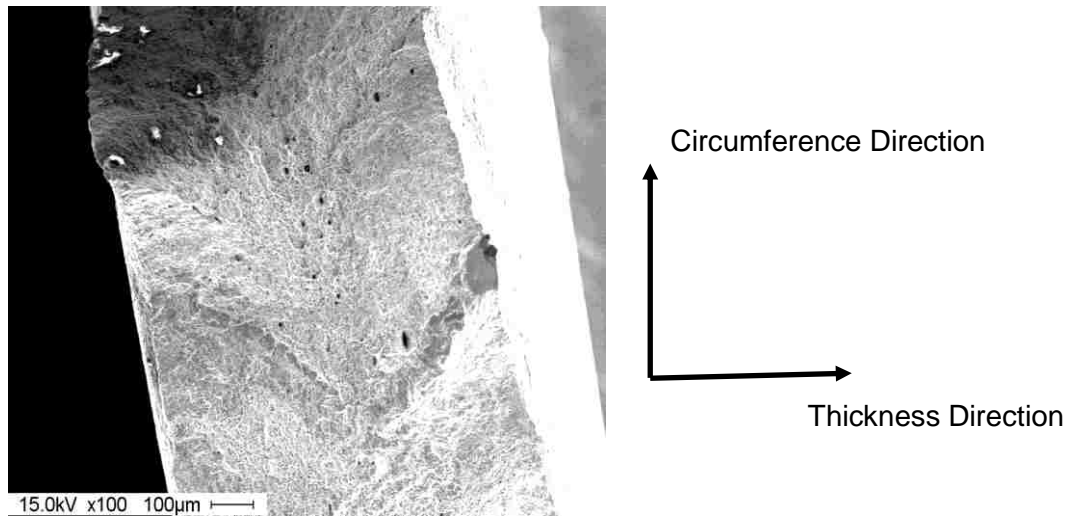


Figure 50: The low magnification fractograph  
(the sample taken from the outside wall of a bent tube)

#### 4.3.2.3 Minimum bend ratio for various DP steel grades

During the experimental work at VariForm, three rotary draw bending tests with different bend ratios were conducted as shown in Table 8. This would seem to indicate that each steel grade has a minimum bend ratio; so that beyond the minimum bend ratio, failure is likely to occur during bending. In these bending trials, DP600 tubes exhibited good bendability even at a 1.73 bend ratio. Failures in DP780 tubes occurred at the 1.73 bend ratio and through-thickness necking in the tube wall was observed at a 2.0 bend ratio. Most DP980 tubes failed at the 2.0 bend ratio, but could be bent at the 3.1 bend ratio.

The forming limit diagrams (FLD) were established according to the Keeler-Brazier equation [89]. According to this empirical equation, it may be possible to qualitatively estimate the bendability of DP steels. As illustrated in



Figure 51, DP600 steel shows the best formability of all three grades of DP steel and the bending trials at a 1.73 bend ratio leads to strains that lie in the marginal zone of the FLD. For DP780 steel, the bending tests at a bend ratio of 2.0 generated strains in the marginal zone, and most tests at the 1.73 bend ratio lead to strains that are above the forming limit. Similarly, the bending tests on DP980 steel tubes at a 3.1 bend ratio induced strains that lie in the marginal zone. Evidently, the FLD are in agreement with the qualitative results described in Table 8. Therefore, from an observation of Table 8 and Figure 51, the minimum bend ratio can be approximately determined as follows:  $R/D = 1.73$  for DP600,  $R/D = 2.0$  for DP780 and  $R/D = 3.1$  for DP980 tubes.

It should be noted that this conventional forming limit diagram is not really suitable to accurately predict the bendability of tubes in rotary draw bending. According to Khodayari [90], because of the residual strains resulting from the tubing process, this conventional forming limit diagram often results in under-utilization of tube material. In other words, if this conventional forming limit diagram predicts a failure for a tubular material, the failure often does not occur and even rarely exhibits any necking. Therefore, in this investigation, combined with the actual bending results, the forming limit diagram provides a qualitative assessment of the minimum bend ratio for various DP steel grades.

Knowing the minimum bend ratio, the maximum (critical) strain in a bent tube can be measured or calculated. It may also help to understand the effect of void formation on deformation behaviour of C-Mn DP steels in bending trials.

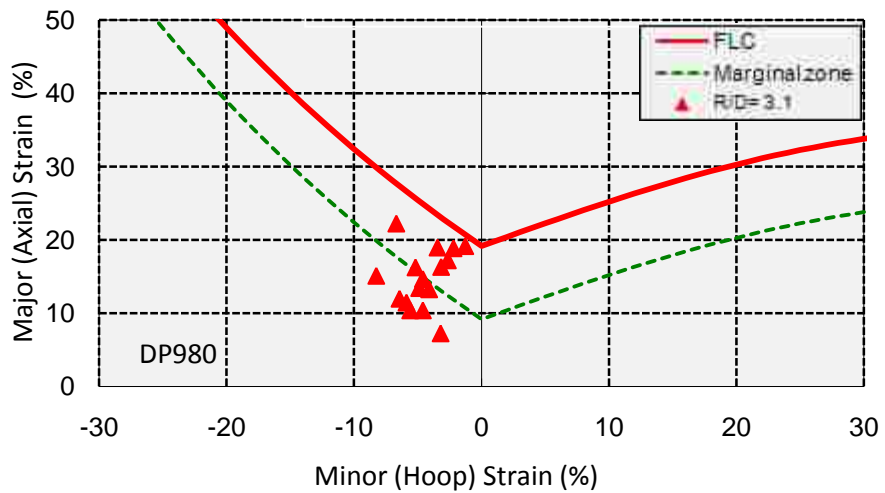
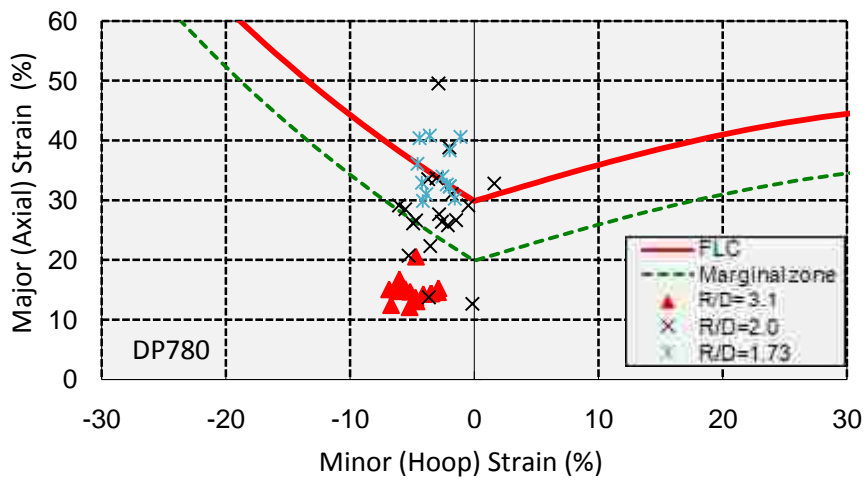
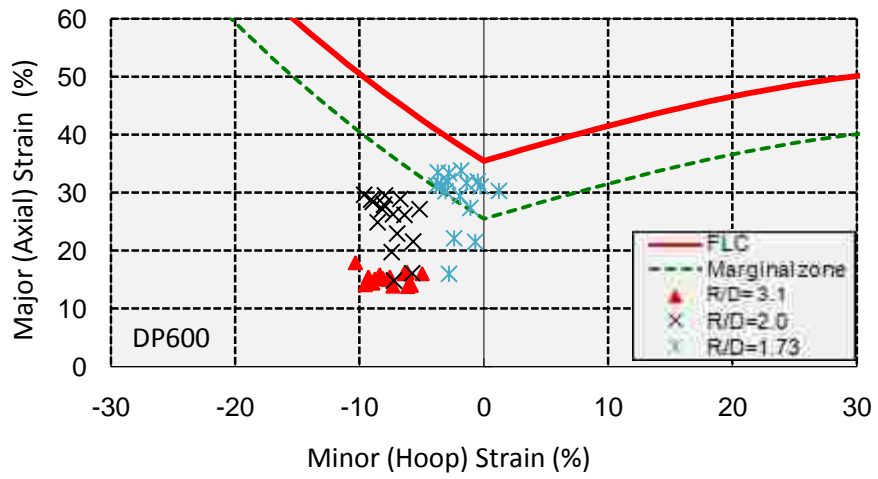


Figure 51: Forming limit diagram (FLD) of C-Mn DP steels for bending trials

#### 4.3.2.4 Void formation and mechanical properties

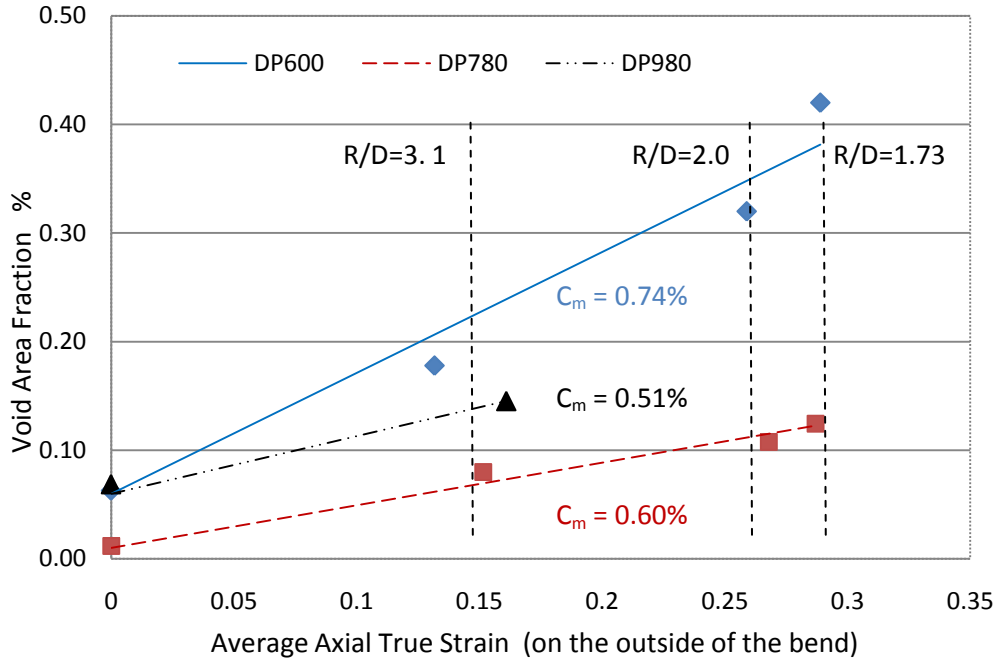


Figure 52: Void area fraction in bent tubes for different steel grades

The void area fraction and void radius were measured for each grade of DP steel using image analysis software. Figures 52 and 53 illustrate the void area fraction and average void radius of bent tubes as a function of strain in different steel grades. In Figures 52 and 53, average axial strains were measured with circle grids etched on the tube surface. The axial strains represent the maximum deformation in each bending test. The original void area fraction values and the original average void radius (average axial strain = 0) were measured in flat sheet samples. These original values depend on the hot and cold rolling process

parameters such as temperature, rolling schedule and looper tension. Almost all the voids in the flat sheet samples were found in the ferrite.

As shown in Figure 52, it is interesting that the void area fraction of DP600 is consistently higher than that of DP780 and DP980 for a given strain, and the void area fraction of DP780 is lower than that of DP980. Void area fraction is one of the important characteristics which can affect the formability of DP steels, but as shown in Figure 52, the void area fractions of the three steel grades are not proportional with the formability of the three DP steel grades.

The martensite carbon content must also have an influence on the rate at which the void area fraction increases. Because the carbon content of the martensite phase in this DP600 steel is higher than that of DP980 and DP780 steels as shown in Table 7, the strength of the martensite in DP600 steel is greater than that of the DP780 and DP980 steels. Thus, for DP600 steel, the deformation incompatibility between martensite and ferrite is also greater than in the other two steel grades. Obviously, this causes a high void area fraction for DP600 steel in each bending test. Also, because the harder martensite of DP600 steel is easier to crack, void nucleation may increase with strain.

In addition, the martensite volume fraction of DP980 steel is much higher than that of DP780 and DP600 steel. Since the higher martensite volume fraction has more interface area with ferrite, it supplies more area to promote void nucleation. This may explain why the void area fraction of DP780 steel is low compared with that of DP980, although DP980 steel has lower deformation incompatibility.

In a successful bending test, the bent tube remains in the stage of uniform strain distribution. Even though the void area fraction of DP600 steel is greater than that of the other three steels, a maximum value of 0.4% still did not result in necking or failure.

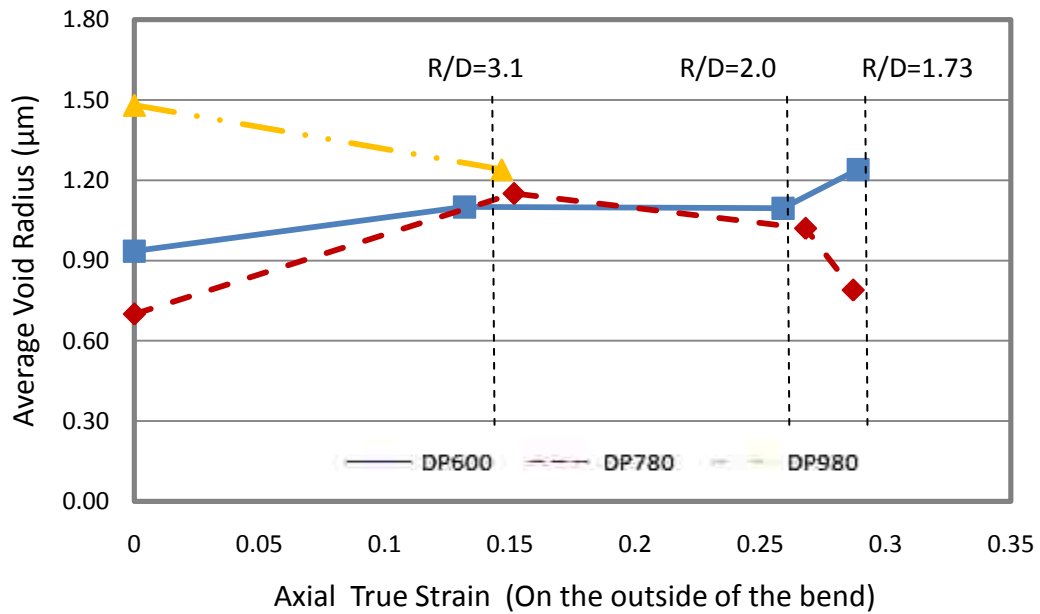


Figure 53: Average void radius in bent tubes for different steel grades

As shown in Figure 53, the average void radius for DP600 steel tubes increases with axial strain. However, the average void radius of DP780 and DP980 decreases with axial strain. This is consistent with the effect of martensite volume fraction on void formation. Since decohesion and void nucleation can occur at the martensite/ferrite interface during plastic deformation, a higher martensite volume fraction provides more interface surface area for void

nucleation. As a result, the average void radius in DP780 and DP980 steel tubes decreases due to the creation of new voids. In contrast, because of the low martensite volume fraction of DP600 steel and high incompatibility deformation (higher martensite carbon content), the average void radius increases with axial strain. However, due to the cracked martensite in DP600 steel, the increase of average void radius seems to take place quite slowly. In Figure 53, since the range of measured average void radius is great, it may only show the tendency of average void radius rather than exactly explain the evolution of void radius in detail for each bending test.

In the previous discussion, it was shown that the microstructural features and chemical composition, such as martensite volume fraction, carbon content of martensite and manganese content, influence the deformation behaviour of C-Mn DP steels. Furthermore, it is expected that there are mutual interactions between these factors. Therefore, it is necessary to estimate which factors may influence mechanical properties using statistical methods. Table 16 lists some of the main factors which play an important role in the behaviour of C-Mn DP steel tubes during a bending operation.

Steel Grade	Void Area Fraction* %	C <sub>m</sub> %	f <sub>m</sub> %	Mn % of Steel	Tensile Strength** MPa	Total Elongation** %	Uniform Elongation** %
DP600	0.42	0.74	12.3	1.01	638.9	22.0	15.9
DP780	0.11	0.60	17.2	1.76	795.9	18.6	11.8
DP980	0.15	0.51	29.2	1.46	1086.5	10.8	8.4

\* The void area fraction was obtained from tubes bent with the minimum bend ratio, which is different for each steel grade.

\*\* These are the sheet tensile properties.

Table 16: Main factors which may influence the mechanical properties

		C <sub>m</sub> %	f <sub>m</sub> %	Mn % of Steel
Correlation Coefficient (Pearson Coefficient)	Uniform Elongation	0.995	-0.966	-0.613
	Total Elongation	0.926	-1.0	-0.367
	Tensile Strength	-0.957	0.998	0.451
	Void Area Fraction %	0.879	-0.637	-0.958

Table 17: List of correlation coefficients

By using linear regression analysis, the correlation coefficients of different important factors (Table 17), which affect the bending behaviour of C-Mn DP steel tubes, were obtained and the extent of correlation with other factors are revealed. As shown in Table 17, the mechanical properties are primarily determined by the

carbon content of the martensite, the martensite volume fraction and the manganese content which determines the severity of martensite banding. And it appears that there is a stronger correlation between void area fraction and manganese content and the carbon content of martensite than with martensite volume fraction. In addition, three linear regression equations ( Equation 4-5, 4-6, 4-7) were established to estimate some mechanical properties and the void area fraction.

$$\varepsilon_u = -0.007 - 0.132f_m + 0.247 C_m \quad (4-5)$$

$$\sigma_{UTS} = 650.062 + 2143.18f_m - 371.3164 C_m \quad (4-6)$$

$$f_v = 0.303 - 0.306Mn + 0.575C_m \quad (4-7)$$

where  $\sigma_{UTS}$  is the tensile strength (MPa),  $\varepsilon_u$  is the uniform elongation (%),  $f_v$  is the void area fraction (%),  $f_m$  is the martensite volume fraction (%),  $C_m$  is the carbon content of the martensite (%) and Mn is the manganese content of the steel (%).

These correlations and equations established between the microstructural features and the mechanical properties are only suitable for the C-Mn DP steel tubes that were bent in this research project. A broader application of these equations would require further validation.

Deformed samples after necking exhibit non-uniform deformation. As shown in Table 18 and Figure 54, DP780 steel, not DP600 steel, exhibits relatively higher post-uniform elongation. Void area fraction and average radius before necking may explain this behaviour. Before necking, as shown in Figures 52 and 53, the void area fraction and the average radius of DP600 are high. After necking, due to the increase in void volume fraction, the DP600 steel fails quickly. In contrast,



before necking, void area fraction of DP780 is low and the average radius is small. With a somewhat softer martensite, more void growth and coalescence can be accommodated before failure. This may explain the higher post-uniform elongation of the DP780 steel.

Good bendability does not ensure suitability for all forming process. Compared with other advanced high strength steels, DP steels exhibit low post-uniform elongation which indicates low stretchability. In response to this problem, some researchers [91,92] have developed a type of DP steel with higher stretchability.

Material	Void Area Fraction* %	Tensile Strength** MPa	Total Elongation** %	Uniform Elongation** %	$\epsilon_f/\epsilon_u$	Post-Uniform Elongation $\epsilon_f - \epsilon_u$
DP600	0.42	638.9	22.0	15.9	<b>1.38</b>	<b>0.061</b>
DP780	0.11	795.9	18.6	11.8	<b>1.58</b>	<b>0.068</b>
DP980	0.15	1086.5	10.8	8.4	<b>1.29</b>	<b>0.024</b>

\* The void area fraction was obtained from tubes bent with the minimum bend ratio, which is different for each steel grade.

\*\* These are the sheet tensile properties.

Table 18: Effect of void area fraction on post-uniform elongation

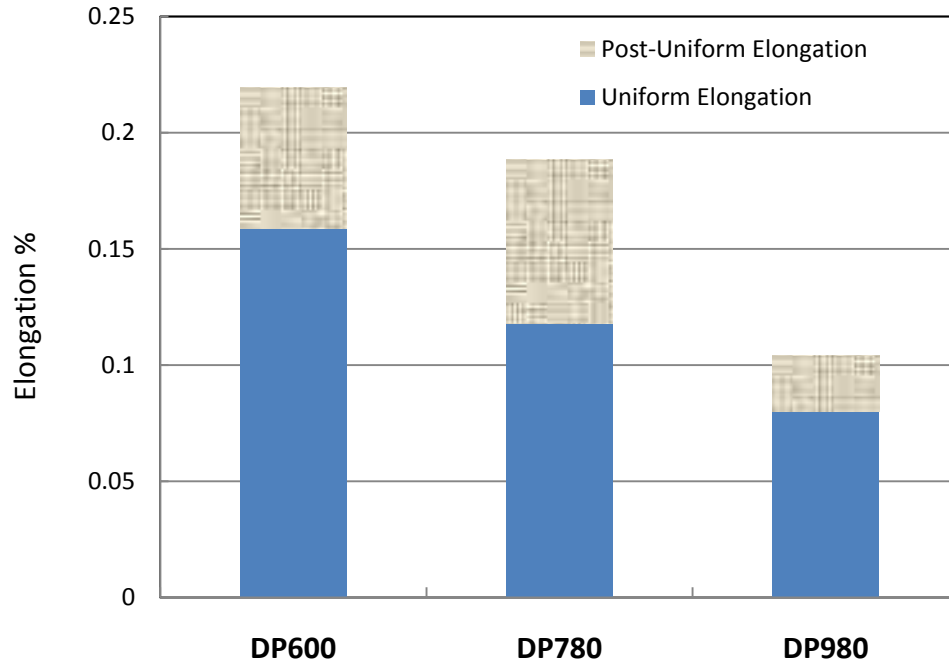


Figure 54: Comparison of elongation values for three grades of DP steel

#### 4.3.2.5 Evaluation and prediction of the minimum bend ratio (maximum axial strain) in rotary draw bending process

The bend ratio is the most important parameter which determines the deformation in rotary draw bending process. Therefore, it is useful and necessary to find a way to predict the minimum (critical) bend ratio for a given grade of DP steel tube.

In section 4.3.2.3, the minimum (critical) bend ratio for each steel grade in this study was approximately taken as follows:  $R/D=1.73$  (DP600);  $R/D=2.0$  (DP780);  $R/D=3.1$  (DP980). The effective strain, the maximum strain on the outside of the bent tube and the tensile properties are listed in Table 19. The

strains listed in Table 19 are the strains along the outside of the bent steel tubes. This is the position where the axial and thickness strains are maximum and critical as discussed in section 4.1.2.

Steel Grade	$\varepsilon_{e1}^*$ $\varepsilon_2=0$	$\varepsilon_{e2}^*$ $\varepsilon_2 \neq 0$	Average Axial Strain	Calculated Axial Strain	Total Elongation** %	C <sub>m</sub> %	R/D (Actual)	R/D (Calculated)
DP600	0.365	0.348	0.316	0.341	22.0	0.74	<b>1.73</b>	<b>1.71</b>
DP780	0.308	0.291	0.267	0.288	18.3	0.60	<b>2.0</b>	<b>1.97</b>
DP980	0.181	0.169	0.157	0.176	10.8	0.51	<b>3.1</b>	<b>3.14</b>

\* Calculated using the measured average axial strain.

\*\* The total elongation of the flat sheets.

Table 19: Effective strain in critical bend ratio  
for various C-Mn DP steel grades

As listed in Table 19, two methods ( $\varepsilon_{e1}$  and  $\varepsilon_{e2}$ ), which are described in detail in Appendix A, can be used to calculate the effective strain of bent tubes in this investigation. If the hoop strain  $\varepsilon_2$  in the bent tube is neglected, the effective strain  $\varepsilon_{e1}$  is calculated with Equation 4-8 (more detail in Appendix A). If the hoop strain in the bent tube is considered, the effective strain  $\varepsilon_{e2}$  can be calculated according to Equation 4-9 (Hill, 1948). Obviously,  $\varepsilon_{e2}$  is a more rigorous representation of the deformation of bent tubes. However, axial strains  $\varepsilon_1$  along the outside of the bent tubes are easy to estimate using Equation 2-9. For the effective strain  $\varepsilon_{e2}$ , the hoop strain  $\varepsilon_2$  is difficult to predict without measurements. In addition, as shown in Table 19, the calculated effective strains using each method are similar. Therefore, the effective strain  $\varepsilon_{e1}$  was selected to establish an empirical equation

for the bend ratio, since the axial strain  $\epsilon_1$  is convenient to verify with actual measurements.

$$\epsilon_{e1} = \frac{2}{\sqrt{3}} \epsilon_1 \quad (4-8)$$

$$\epsilon_{e2} = \sqrt{\frac{r+1}{2r+1} [(r+1)(\epsilon_1^2 + \epsilon_2^2) + 2r\epsilon_1\epsilon_2]} \quad (4-9)$$

where

$\epsilon_{e1}$  - Effective Strain along the outside of bent tubes (hoop strain  $\epsilon_2=0$ )

$\epsilon_{e2}$  - Effective Strain along the outside of bent tubes (hoop strain  $\epsilon_2 \neq 0$ )

$\epsilon_1$  - Axial Strain along the outside of bent tubes

$\epsilon_2$  - Hoop Strain along the outside of bent tubes

$r$  - r-value of the steel sheet

In order to establish an empirical equation to predict the bend ratio in rotary draw bending, the factors comprising the equation must be easy to calculate or measure for manufacturers. Moreover, the factors should reflect the main characteristics and parameters of C-Mn DP steels. Following the discussion in Section 4.3.2.4, the total elongation and the carbon content of the martensite were selected and Equation 4-10 was determined by linear regression to evaluate and predict the maximum effective strain along the outside of the bent tube, i.e. the critical deformation of the studied bent tubes.

$$\varepsilon_{e1} = 0.025 - 0.059C_m + 0.019\varepsilon_t \quad (4-10)$$

where

$\varepsilon_t$  – Total elongation

$C_m$  – Carbon content of martensite

Substituting Equation 2-9 into Equation 4-8, the empirical equation for the bend ratio becomes:

$$\frac{R}{D} = \frac{\exp^{0.866\varepsilon_{e1}}}{-1 + 2\sqrt{0.25 + \exp^{1.732\varepsilon_{e1}} - \exp^{0.866\varepsilon_{e1}}}} \quad (4-11)$$

R – Centre-line radius of bent tube

D – Tube outer diameter

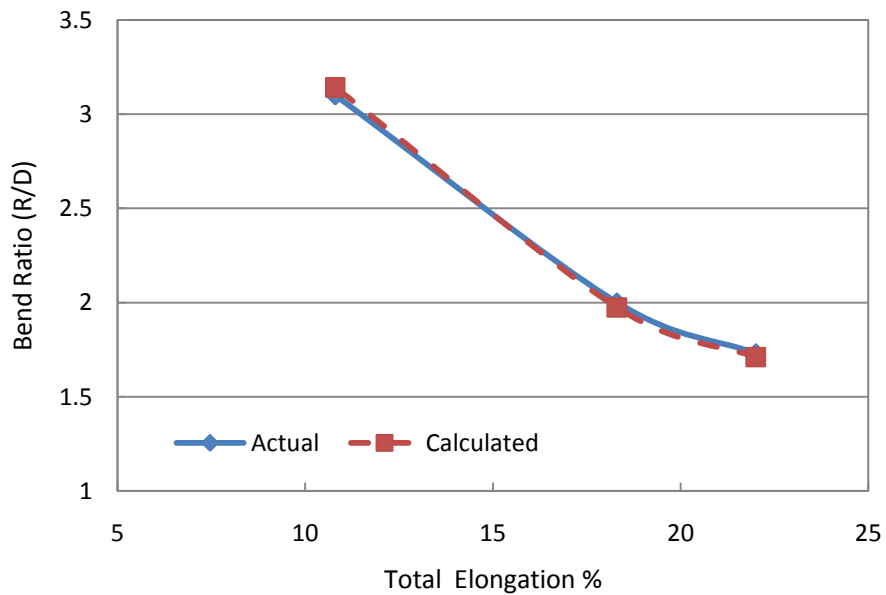


Figure 55: Actual bend ratio vs. calculated bend ratio

As shown in Figure 55, the calculated value through Equation 4-7 is in good agreement with the actual (experimental) value. In the actual rotary draw bending process, this empirical equation may be used to predict the minimum bend ratio that will avoid failures.

It should be noted that Equation 4-7 may only be suitable for C-Mn DP steel tubes, because the dependent variables in the equation involve a microstructural parameter and a tensile property which are specific to these C-Mn DP steels. Extending the application of this expression to other grades of DP steel tubes would require further validation. Moreover, because the bending tests in this project were conducted using only three bend ratios, the accuracy of the bend ratio prediction may not be adequate, particularly, when the target bend ratio is less than 1.73. Therefore, it will be necessary to validate Equation 4-7 as new tube bending data for C-Mn DP steel becomes available.

#### 4.4 Deformation behaviour of DP steels in tube bending

##### 4.4.1 Background of DP steels deformation behaviour (analysis of stress-strain curves for C-Mn DP steels)

In this section, as shown in Table 20, two relationships (Hollomon's power law and Jaoult-Crussard's (J-C) function [8,93,94], were used to represent the stress-strain curve and investigate the deformation behaviour of C-Mn DP steels.

	Constitutive Equation	Analytical Equation	Analytical Method
Hollomon Relation	$\sigma = K\varepsilon_p^n$	$\ln \sigma = \ln K + n \ln \varepsilon_p$	Hollomon's power law
Ludwik Relation	$\sigma = \sigma_0 + K_1 \varepsilon_p^{n_1}$	$\ln \frac{d\sigma}{d\varepsilon} = \ln(K_1 n_1) + (n_1 - 1) \ln \varepsilon_p$	Jaoult-Crussard analysis

Table 20: Analytical representation of stress - strain curves

The deformation behaviour of the microstructural phases of DP steel is more complex than that of single phase steels, because the deformation behaviour of DP steels depends on the deformation of two different phases and on the compatibility between these phases. The Hollomon power law was considered to describe the strain hardening behaviour in this investigation (Figure 56). However, it can be seen from Figure 56 that the strain hardening coefficient is not constant and C-Mn DP steels clearly exhibit two stages of work hardening behaviour. Therefore, the workhardening behaviour of DP steels cannot be properly described by the Hollomon power law as can most other low-carbon steels.

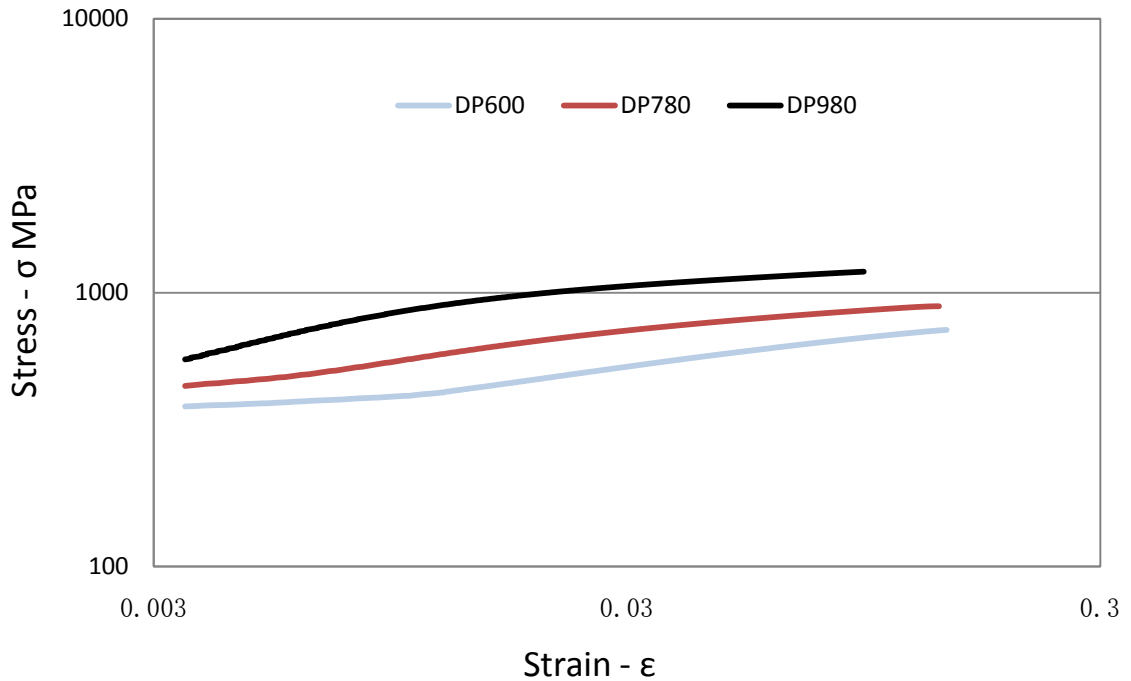


Figure 56: Hollomon relation ( $\ln\sigma$  vs.  $\ln\epsilon$ )

Figure 57 represents the stress-strain data as a Jaoult-Crussard analysis, where the work hardening rate is plotted as a function of strain in a logarithmic scale. At higher strains the rate of strain hardening is similar for the various C-Mn DP steel grades. But at lower strains, the strain hardening behaviour varies from one grade of DP steel to another and shows a transitional behaviour as shown in Figure 57. According to Matlock et al. [95] and Lawson et al. [96], the transition at the beginning of deformation of DP steel, reflects an increase in the degree of inhomogeneity during the deformation and varies for steel grades from DP980 to DP600. As shown in Figure 30, DP600 steels even display some yield point elongation because of the low martensite volume fraction. However, the micro-mechanisms that cause this transitional behaviour are not clear at present, but may be due to interactions between the martensite, the retained austenite and non-uniformly strained ferrite.



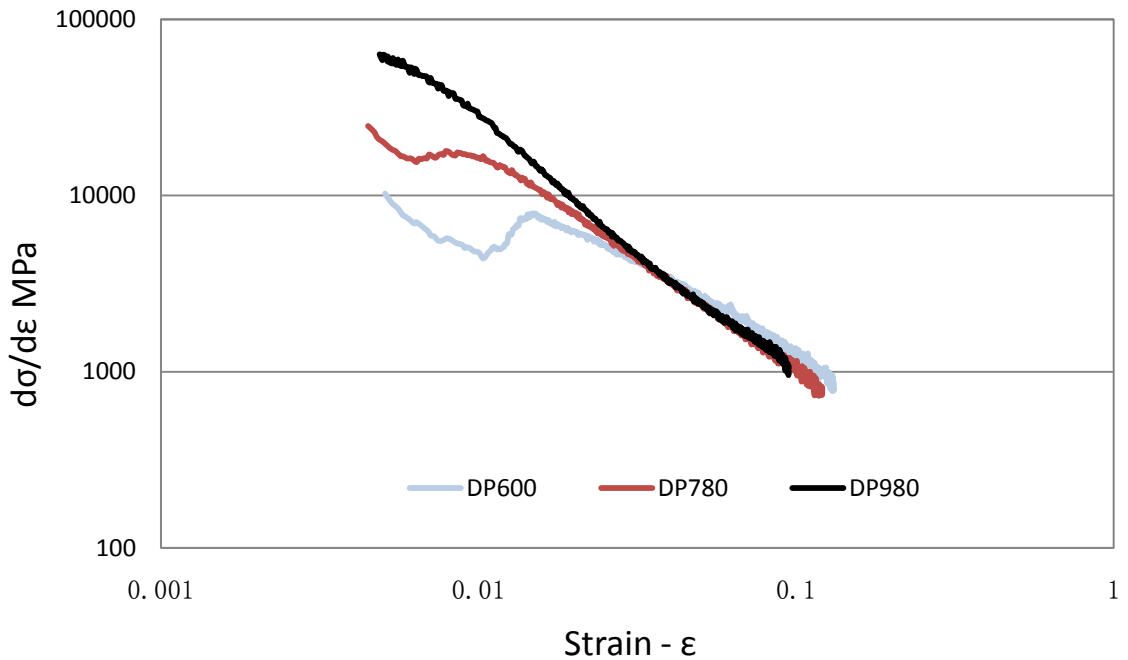


Figure 57: Ludwik relation  $\ln(d\sigma/d\epsilon)$  vs.  $\ln\epsilon$

In summary, the analysis of the stress-strain curve shows that the work hardening behaviour of DP steels cannot be described by a single equation due to microstructural interactions between phases. Therefore, it may be useful to analyze the deformation behaviour of each of the phases.

#### 4.4.2 Ferrite and martensite deformation behaviour

The macro-strain of DP steels results from the accumulated ferrite and martensite micro-strains. Thus, it is necessary to discuss the tendency of strain distribution between martensite and ferrite. As mentioned in Section 3.3.3.3, the ferrite and martensite strains of the three DP materials were estimated from various bent tubes obtained with different bend ratios (see Table 9 on page 52).

As shown in Figure 58, the ferrite deformation of DP600 steel is greater than DP780 and DP980 steels since the lower martensite volume fraction in DP600 requires that more deformation occur in the ferrite. The martensite deformation in DP600 and DP780 steels are almost the same and the martensite in the DP980 exhibits slightly more deformation compared with that in the DP600 and DP780 steels because of the lower carbon content in the martensite (Table 7 on page 48). Comparing the strains in the martensite and in the ferrite for the three C-Mn DP steels, the ferrite clearly undergoes more strain during the bending process. The micro-strain data in Figure 58 confirms that, during the deformation of DP steels, the softer ferrite is largely responsible for the formability.

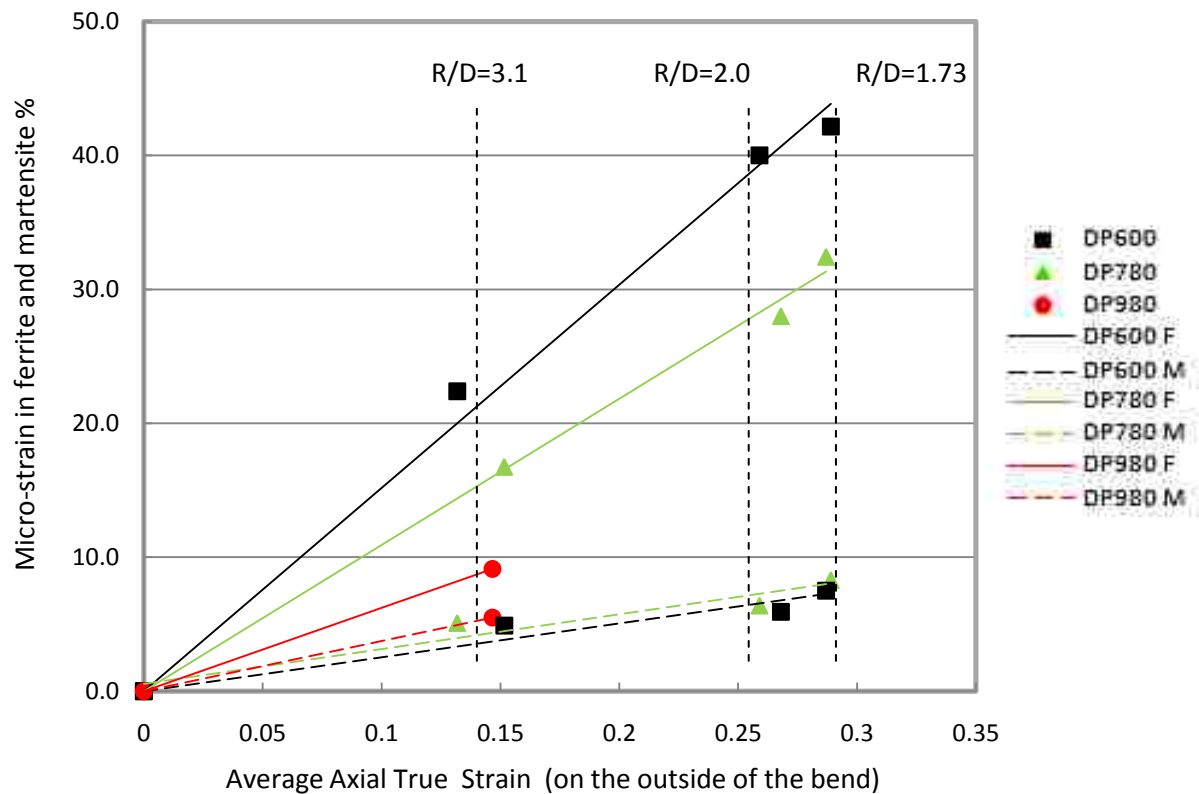


Figure 58: Martensite and ferrite strains

Figure 59 shows how the martensite volume fraction influences the deformation behaviour of each phase and highlights the issue of strain compatibility between phases. As shown in Figure 59, in the same bending test (bend ratio = 3.1), the strain difference between the martensite and the ferrite decreases as the martensite volume fraction increases. This is primarily due to the increasing volume of ferrite that is constrained by martensite, and also because of the decrease in carbon content in the martensite. In addition, the ferrite strains decrease with the increase in martensite volume fraction but the martensite strains only increase very slightly. Therefore, the martensite volume fraction (Table 7) is one of the most important factors that determine the deformation of each phase and the strain distribution in C-Mn DP steels. Concurrently, the deformation of the martensite mainly depends on the carbon content in the martensite which in turn greatly influences the compatibility between the phases. These observations are consistent with the earlier research in Section 4.3.2.4.

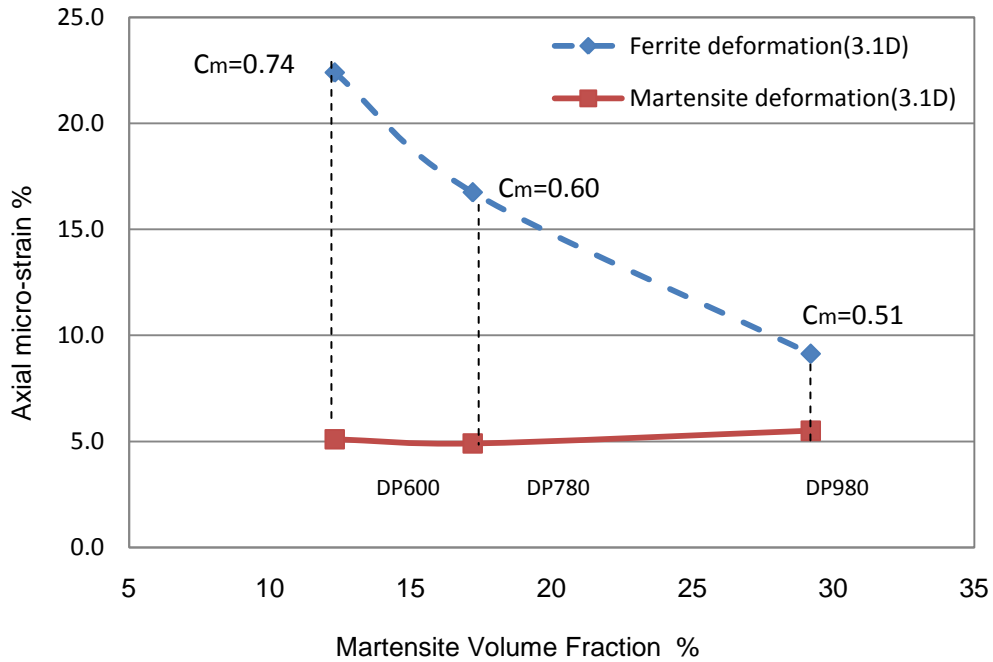


Figure 59: Axial strain in each phase vs. martensite volume fraction for a 3.1 bend ratio.

According to many investigations [8,9,97,98], the microstructural deformation behaviour of DP steels can be divided into three stages. In the first stage, the deformation of the ferrite and the martensite is elastic. In the second stage, with increasing strain, the ferrite is plastically deformed while the martensite continues to deform elastically. In the last stage, due to increased load being transferred to the martensite through the martensite-ferrite interface, both phases deform plastically. Failures may occur in the second or third stage depending on the mechanical properties and microstructural features of the DP steel under consideration.

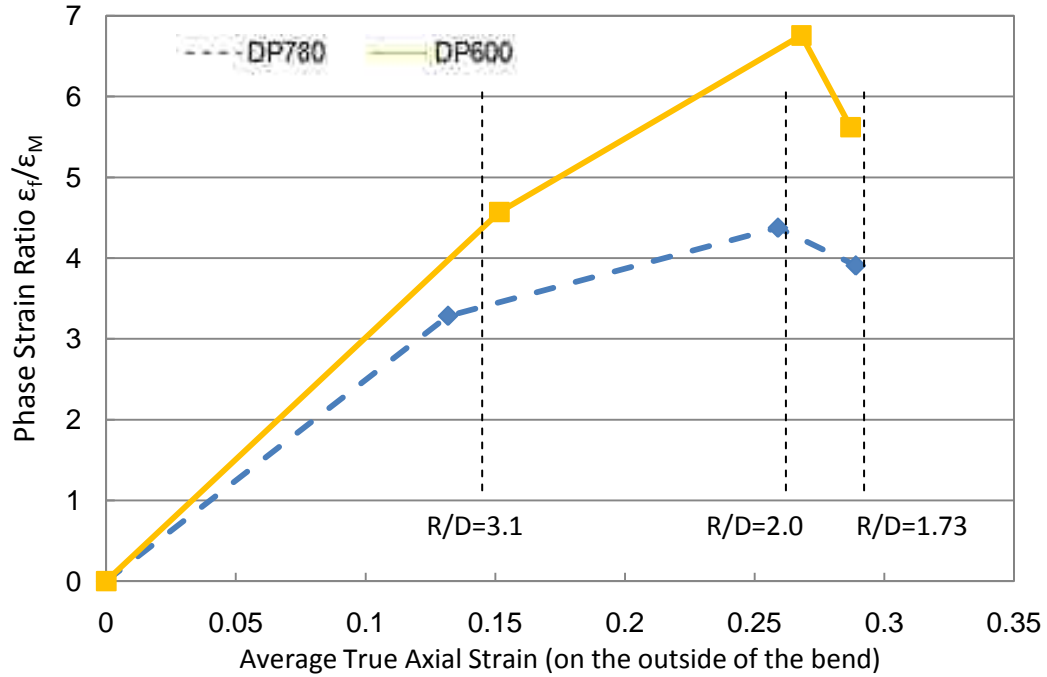


Figure 60: Evolution of the ratio of ferrite to martensite strain ( $\epsilon_F/\epsilon_M$ ) with bending strain

In order to describe the change in strain distribution between the two phases as a function of the average axial strain along the outside of the bend of C-Mn DP steel tubes, the ratio of ferrite to martensite strains was plotted as shown in Figure 60. Since the martensite in the DP600 steel is harder than that in the DP780 steel as mentioned earlier in this section, the ratio of ferrite to martensite strains ( $\epsilon_F/\epsilon_M$ ) in DP600 steel is greater than that in the DP780 steel. However, as shown in Figure 60, the variation in the  $\epsilon_F/\epsilon_M$  ratio with bending strain exhibits the same trend for both DP600 and DP780 steels. It can be seen that in the less severe bending tests ( $R/D= 3.1$  and  $2.0$ ), the  $\epsilon_F/\epsilon_M$  ratio increases with an increase in axial strain. But for more severe bend ratios ( $R/D < 2.0$ ), the  $\epsilon_F/\epsilon_M$  ratio decreases with an increase in axial strain. This would indicate that the martensite

contributes more to the overall deformation after an axial strain of about 0.28 ( $R/D=2.0$ ). Nevertheless, Figure 58 shows that in the most severe bending test ( $R/D=1.73$ ), the strains in the martensite after yielding are only slightly higher than the strains in the least severe bending test ( $R/D=3.1$ ), because of the low formability of the martensite.

Therefore, the iso-strain model [99] and the simple rule of mixtures based on the long fibre (section 2.1.3), which were established to delineate the whole deformation behaviour of DP steels, appear to be too simplistic.

## CHAPTER 5

### CONCLUSIONS

Based on this investigation, the following conclusions can be drawn:

1. Martensite banding, which is primarily affected by the manganese content of the steel, has almost no effect on strength, but it appears to have some effect on elongation. Martensite banding is just one of the microstructural features which can influence the anisotropic deformation behaviour of C-Mn DP steels. The steel casting and rolling process are critical operations which have an influence on the initiation of martensite banding.
2. Non-metallic inclusions play a very important role in the onset of failures during the bending process. In this study, ductile sulfide inclusions (deformed) and hard oxide inclusions (undeformed) were observed. The steel making and casting processes are critical to control and reduce the amount of non-metallic inclusions.
3. The three DP steels considered in this investigation mainly displayed ductile fracture and DP980 steel showed a kind of quasi-cleavage fracture.
4. In terms of the microstructure and statistical analysis, void area fraction is mainly influenced by carbon content of martensite and manganese content of C-Mn DP steels. A linear regression equation was established to characterize this correlation. For C-Mn DP steels, the post-uniform elongation, which determines the stretchability, is greatly affected by void area fraction.

5. An empirical equation was established to predict and estimate the critical effective strain and minimum bend ratio of C-Mn DP steels in terms of the carbon content of martensite and the total elongation, which are easy to calculate and measure. The predicted values of effective strain and minimum bend ratio are in good agreement with the experimental values.
6. The martensite volume fraction is one of the most important factors that determine the strain distribution in each phase of C-Mn DP steels. The strain in the martensite depends somewhat on the carbon content of the martensite which greatly influences the compatibility of strain between the two phases.
7. The iso-strain model and the simple rule of mixtures based on the long fibre, which were established to delineate the whole deformation behaviour of DP steels, appear to be too simplistic, due to the strain distribution between martensite and ferrite.



## CHAPTER 6

### RECOMMENDATIONS FOR FUTURE WORK

Based on the experimental results and the microstructural analyses carried out in this study, it would be helpful and useful to further understand the deformation behaviour of C-Mn DP steels in the following additional recommended investigations.

1. The effect of martensite banding on impact tests of C-Mn DP steels could be further studied in order to characterize and analyze how the martensite banding affects the crashworthiness of vehicles made with a significant proportion of structural parts made from DP steel.
2. Low post-uniform elongation of DP steels results in low stretchability compared with HSLA steels. In the automobile industry, local deformation is required in some cases. Therefore, a new grade of DP steel could be designed to particularly satisfy the requirement of stretchability without sacrificing the strength and formability of common DP steels.
3. In this study, ferrite and martensite strains were measured in order to analyze the microstructural deformation behaviour of C-Mn DP steels. The hardness of martensite and ferrite could also be measured in order to further understand the deformation behaviour of DP steel. Thus, additional nano-indentation tests could be carried out. Combined with the martensite and ferrite strains and hardness, the deformation behaviour of DP steel in bending may be better understood. An analytical model may be found to

describe the deformation behaviour correlated with strain distribution and microstructure of C-Mn DP steels.

## REFERENCES

1. McFarlan, W. H. (1968): *US Patent*, No. 3378360.
2. Hayami, S., Furukawa, T. (1977): *Microalloying 75*, Union Carbide Corp., New York, 311.
3. "Advanced High Strength Steel (AHSS) Application Guidelines Version 4.0." *World Steel Association*, March 2009
4. Davenport, A. T., ed. (1979): *Formable HSLA and DP Steels*, TMS-AIME, Warrendale, Pennsylvania.
5. Coldren, A. P., Tither, G. J. (1976): "Development of a Mn-Si-Cr-Mo as-rolled DP steel." *J. Met.*, 28(5), 5-10.
6. Kot, R. A., Morris, J. W., ed. (1979): *Structure and properties of DP steels*, TMS-AIME, Warrendale, Pennsylvania.
7. Kot, R. A., Bramfit, B. L., ed. (1981): *Fundamentals of DP Steels*, TMS-AIME, Warrendale, Pennsylvania.
8. Ma, M., Wu, B. (2009): *DP steels – physical and mechanics metallurgy*, Metallurgical Industry Press, Beijing.
9. Rashid, M. S. (1981): "DP Steels." *Ann. Rev. Mater. Sci.*, 11, 245-266.
10. Lei, T., Shen, X. (1982): "Research of SX20 steel." *Acta Metallurgica Sinica*, 18, 75-83.
11. Doane, D. V., Kirkaldy, J. S., ed. (1978): *Hardenability concepts with applications to steel*, Met. Soc. of AIME, Warrendale.
12. Dinda, S., Dicello, J. A., Kasper, A. S. (1975): *Micro-alloying 75*, Union Carbide Corp., Washington, 33.
13. Shaw, J. (2009): "ULSAB-AVC-On the Road Today." *Great Designs in Steel Seminar*, American Iron and Steel Institute.

14. Khodayari, G., Worswick, M. (2003): "Examining the effects of push assist on the formability of aluminum tubes." *Tube & Pipe Journal*, 7-11.
15. Koc, M., Cora, O. N. (2008): "Introduction and state of the art of hydroforming." *Hydroforming for advanced manufacturing*, Koc, M., ed., CRC, NewYork, 1-28.
16. Fallahi, A. (2002): "Microstructure-Properties correlation of DP steels produces by controlled rolling process." *J.Mater.Sci.Technol.*, 18(5). 451-454.
17. Chakraborti, P. C., Mitra, M. K. (2007): "Microstructure and Tensile Properties of High Strength Duplex Ferrite-Martensite(DFM) Steels." *Materials Science and Engineering A*, 466, 123-133.
18. Irie, T, Satoh, S. Hashiguchi, K. (1981): "Metallurgical Factors Affecting the Formability of Cold-rolled High Strength Steel Sheets." *Tran. ISIJ*, 21, 793-801.
19. Degarmo, E., Paul, E., Black, J. T., Ronald, A. (2003): *Materials and Processes in Manufacturing (9th ed.)*, Wiley.
20. Lopez-Baltazr, A., Salinas-Rodriguez, A., Nava, E. (2007): "Austenite-Ferrite transformation in hot rolled Mn-Cr-Mo DP steels." *Materials Science Forum*, 560, 79-84.
21. Wu, J., Ye, W. (1994): "Current status and trend of development in Research and application of DP steel." *Research on Iron & Steel*, 77(2), 51-58.
22. Zhu, X., Wang, L. (2003): "Effect of continuous annealing parameters on the mechanical properties of cold rolled Si-Mn DP steel." *Special Steel*, 684-688.
23. Mould, P. R. (1982): "Overview of continuous-annealing technology for steel sheet products." *Journal of Metals*, 34, 18-28.

24. Zhang, Z., Song, R. (2008): "Effect of continuous annealing process and alloy element on microstructure and mechanical properties of 800MPa cold rolling DP steel." *Material & Heat Treatment*, 37(6), 27-33.
25. Yu, E., Wang, M. (1992): "Formability evaluation of batch annealing DP steel." *Angang Technology*, 201(3), 37-42.
26. Repas, P. (1979): "Physical metallurgy of DP steels." *Mech. Working and Steel Processing Conf. XVII*, AIME, NY, 277-305.
27. Huang, J. (2004): "Microstructure evolution during processing of DP and trip steels." PhD Dissertation, University of British Columbia, Vancouver, BC.
28. Dou, T., Kang, Y., Yu, H. (2008): "Microstructural evolution of cold rolled DP steel during initial stages of continuous annealing." *Metal Heat Treatment*, 33(3), 31-35.
29. Mi, Z.: "DP steel and TRIP steel." *CITIC Metal*,  
<<http://www.metal.citic.com/iwcm/UserFiles/img/cd/jszl/jszl0403-004.pdf>>  
(Nov. 25, 2008).
30. Wycliffe, P. A. (1981): "Austenite growth in the intercritical annealing of ternary and quaternary DP steels." PhD Dissertation, McMaster University, Hamilton, ON.
31. Jiang, J. (2007): "Water quenching and tempering technology research of 1000MPa ultra high strength DP steel." MAsC thesis, University of Shanghai Jiaotong, Shanghai.
32. Kuang, S., Kang, Y., Yu, H. (2008): "Simulation of intercritical austenization of a C-Mn cold rolled DP steel." *Materials Science Forum*, 575, 1062-1069.
33. Xu, Z. (1999): *Martensite and martensitic transformation (2nd ed.)*, Science Press, Beijing.
34. Dieter, G. (1988): *Mechanical Metallurgy*, McGraw - Hill Book Company, NY.

35. Ma, M., Wang, D., Wu, B. (1981): "Study of deformation characteristics of Mn-V DP steel." *Gnangtie*, 10, 52-60.
36. Ramos, L. F., Matlock, D. K., Krauss, G., Huppi, G. S. (1979): "On the deformation behaviour of DP steels." *Metall. Trans. A*, 10, 259-261.
37. Zhou, Y., Liu, Y. (1986): "The regression analysis of structure parameters and behaviours of DP steel." *Journal of Xian Jiaotong University*, 20(2), 111-118.
38. Li, Z., Luo, J., Wang, Y. (1987): "Influence of ferrite-martensite microstructure on stress and strain distribution in two phases for 12CrMo steel analyzed with finite element method." *ACTA Metallurgica Sinica*, 23(2), 111-117.
39. Al-Abbasi, F. M., Nemes, J. A. (2003): "Micromechanical modeling of DP steels." *International Journal of Mechanical Sciences*, 45, 1449-1465.
40. Liu, X. (1991): "Phase strain distribution and work hardening behaviour of DP steel." *Journal of Tsinghua University*, 31(2), 101-107.
41. Ostrom, P. (1981): "Deformation models for two-phase materials." *Metall. Trans. A*, 12A, 335-357.
42. Xu, Z., Liu, X. (1988): "A study of the relationship between strength and plasticity of low carbon alloy dual phase steel." *Journal of Shanghai Jiaotong University*, 22(1), 87-96.
43. Krauss, G. (1978): *Hardenability concepts with application to steel*, Doane, D. V., Kirkaldy, J. S., ed., AIME, Warrendale, 229.
44. Koo, J. Y., Young, M. J., Thomas, G. (1980): "On the law of mixtures in DP steels." *Metall. Trans.*, 11A, 852-854.
45. Davies, R. G. (1978): "Influence of martensite composition and content on the properties of DP steels." *Metallurgical Tran. A*, 9(5), 671-679.

46. Emi, T. (2000): *The Brimacombe Memorial Symp.*, Canadian Institute of Mining, Metallurgy and Petroleum, Montreal, 23-28.
47. Krauss, G. (2003): "Solidification, segregation, and banding in carbon and alloy steels." *Meta. Trans. B*, 34B, 781-792.
48. Francisca, G. (2006): "Evolution of microstructural banding during the manufacturing process of DP steels." *Materials Trans.*, 47(9), 2269-2276.
49. Xu, W., Rivera, P. E. J. (2006): "Ferrite/Pearlite band prevention in DP and trip steels model development." *ISIJ International*, 45(3), 380-387.
50. Bastien, P. G. (1957): "Mechanism of formation of banded structures -- Tenth Hatfield Memorial Lecture." *Journal of iron steel inst.*, 281-291.
51. Flemings, M. C. (1974): *Solidification processing*, McGraw-Hill, Inc., New York.
52. Fisher, R. M., Speich, G. R., Cuddy, L. J., Hu, H. (1976): "Physical Chemistry in Metallurgy." *Proc. Darken Conf.*, US Steel, Monroeville, PA, 463-488.
53. Gensamer, M. (1952): "General survey of the problem of fatigue and fracture." *Fatigue, and Fracture of Metals*, John Wiley & Sons, Inc., New York.
54. Colangelo, V. J., Heiser, F. A. (1987): *Analysis of Metallurgical Failures*, John Wiley&Sons,Inc., NewYork, 105.
55. Eliezer, D. (1981): "High-temperature hydrogen attack of carbon steel." *Journal of Materials Science*, 16 (11), 2962-2966.
56. Mahoney, M. W., Paton, N. E. (1973): "The effect of oxygen, nitrogen, and hydrogen on the mechanical properties of Cb-752." *5th Spring Meeting of Metallurgical Society of AIME*, 103.
57. Liao, C., Sun, F., Lan, F. (1979): "An investigation of quasi-cleavage fracture in steel." *ACTA Metallurgica Sinica*, 15(2), 259-265.

58. Singh, H. (2003): *Fundamentals of Hydroforming*, Society of Manufacturing Engineers,
59. Katsumi, M., Yutaka, N. (2006): "Manufacturing process and products of steel pipes and tubes in JFE Steel" *JFE Technical Report*, 1-6.
60. Green, D. E. (2008): "Formability analysis for tubular hydroformed parts." *Hydroforming for Advanced manufacturing*, Koc, M., ed., CRC, NewYork, 93-117.
61. Li, J., Feng, Z. (2006): "Pipe traverse tensile properties affected by longitudinal welded pipe procedure." *Welded Tube and Pipe*, 29(5), 25-30.
62. Olsson, K. (1988): *Processing microstructure and properties of HSLA steels*, TMS, Pittsburgh, PA, 331-334.
63. Khodayari, G. (2008): "Pre-forming: tube rotary draw bending and pre-flattening/crushing in hydroforming." *Hydroforming for Advanced manufacturing*, Koc, M., ed., CRC, NewYork, 181-202.
64. Bardelcik, A. (2006): "Effect of pre-bending and hydroforming parameters on the formability of advanced high strength steel tube." MAS Thesis, University of Waterloo, Waterloo, ON.
65. Zhao, J. (2004): "Numeric simulation analysis for pre-bending process of automotive subframe hydroforming." Master Thesis, Jilin University, Changchun, China.
66. Li, H., Yang, H., Zhan, M., Kou, Y. L. (2010): "Deformation behaviors of thin-walled tube in rotary draw bending under push assistant loading conditions." *J. Materials Processing Tech.*, 210(1), 143-158.
67. Gholipour, J., Worswick, M. J., Oliveira, D. A., Khodayari, G. (2004): "Severity of the bend and its effect on the subsequent hydroforming process



- for aluminum alloy tube." *Materials Processing and Design: NUMIFORM2004*, 712, 1089-1094.
68. Inoue, K., Mellor, P. B. (1978): "Radial-draw bending of stainless steel tube." *Journal of Mechanical Working Technology*, 168, 327-335.
69. Khodayari, G. (2003): "Hydroforming of pre-bend aluminum tubes." *International Conference on Accuracy in Forming Technology (ICAFIT)*, Chemnitz, Germany, 149-161.
70. Sheng, Z., Xie, S., Pan, C. (1989): *Probability and statistic*, High Education Press, Beijing.
71. Rummel, R. J. (2002): "Understanding correlation."  
<<http://www.hawaii.edu/powerkills/UC.HTM#C4>> (June 25, 2009).
72. Lin, D., Shen, L. (1999): "Quantitative analysis of banded structure in 16Mn steel plate." *Physics Examination and Testing*, 23-25.
73. Anon, (1991): "Effect of pearlite banding on mechanical properties of hot-rolled steel plate." *ISIJ Int.*, 31, 1445-1446.
74. Zhang, G., Tian, C., Wu, J., Wang, G., Wang, Y. (1994): "The effects of Si, Mn and rolling processing on microstructure and property of as-hot-rolled non-stamping DP steels." *Journal of University of Science and Technology Beijing*, 2, 148-153.
75. Lin, D., Shen, L. (2000): "Determination and calculation of critical cooling rate eliminating banded structure of 16Mn steel plate." *Iron and Steel*, 35, 40-43.
76. Majka, T. F., Matlock, D. K., Krauss, G. (2002): "Development of microstructural banding in low-alloy steel with simulated Mn segregation." *Metallurgical and Materials Tran. A*, 34A, 1627-1637

77. Liu, Y. (2000): "Reason of formation harmful effect and removal of band structure in low carbon alloy steel." *Heat Treatment of Metals*, 12, 1-3.
78. Liu, R., Yin, X., Shi, X., Huang, D. (2005): "Effect of hot rolling banded microstructures on microstructure and mechanical properties of hot dip galvanized DP steels (DP600)." *Automobile Technology & Material*, 11, 27-28.
79. Wang, Y., Xu, Z. (2004): "Comparative investigation of solidification quality between thin slab and conventional slab." *Casting Slab Quality*, 4, 39-41.
80. Ray, A., Paul, S. K., Jha, S. (1995): "Effect of inclusions and microstructural characteristics on the mechanical properties and fracture behavior of a high-strength low-alloy steel." *J. Mater. Eng.*, 4(12), 679-688.
81. Wang, X., Wen, T., Fu, G. (2008): "Practice of reducing inclusion in cold rolled sheet steel." *Angang Technology*, 2, 53-55.
82. Giampietro, T., Domenico, S., Silvio, R. (2007): "Routine qualitative analysis of inclusions in steel." *Metallurgical Analysis*, 27(4), 1-6.
83. Dai, Y., Cai, X., Guo, Z. (1997): "Non-metallic inclusions in continuous cast strand." *Iron Steel Vanadium Titanium*, 18(3), 34-40.
84. Mazinani, M. (2006): "Deformation and fracture behaviour of a low-carbon DP steel." PhD Dissertation, University of British Columbia, Vancouver, BC.
85. Shen, X., Lei, T., Liu, J. (1985): "The SEM in situ observation of tensile fracture process in plain carbon DP steels." *Acta Metallurgica Sinica*, 21, A228-233.
86. Zhang, Z., Liu, M., Su, H., Xu, Y. (1985): "Deformation and fracture of low carbon Martensite-Ferrite DP steel." *Acta Metallurgica Sinica*, 21, A384-387.

87. Zhong, Q., Zhao, Z., Zhang, Z. (2005): "Development of "fractography" and research of fracture micromechanism." *Journal of Mechanical Strength*, 27, 358-370.
88. Avramovic-Cingara, G., Ososkov, Y., Jain, M. K., Wilkinson, D. S. (2009): "Effect of martensite distribution on damage behaviour in DP600 DP steels." *Materials Science and Engineering A*, 516, 7-16.
89. Keeler, S. P., Brazier, W. G. (1977): "Relationship between laboratory material characterization and press-shop formability." *Microalloying* 75, 517-530.
90. Khodayari, G. (2009): "Bending limit curve for rotary draw bending of tubular components in automotive hydroforming applications." *SAE International*, 841-848.
91. Miura, M., Nakaya, M., Mukai, Y. (2008): "Cold-rolled 980MPa grade steel-sheets with excellent elongation and stretch-flangeability." *Kobelco Technology Review*, 28(10), 8-12.
92. Tetsuya, M., Kohei, H., Hidetaka, K. (2004): "Ultra high-strength steel sheets for bodies, reinforcement parts, and seat frame parts of automobile." *JFE Technical Report*, 4(11), 38-43.
93. Crussard, C. (1953): "Relation between exact form of tensile curves of metals and accompanying changes in their structure." *Revue de Metallurgie*, 50(10), 697-710.
94. Ramos, L. F., Metlock, D. K., Krauss, G. (1979): "Communications on the deformation behavior of DP steels." *Metallurgical Transactions A*, 10A, 259-261.

95. Matlock, D. K., Krauss, G., Ramos, L. F. (1979): "A correlation of processing variables with deformation behavior of DP steels." *Structure and properties of dual-phase steels*, The metallurgical society of AIME, 62-90.
96. Lawson, R. D., Matlock, D. K., Krauss, G. (1981): "The effect of microstructure on the deformation behaviour and mechanical properties of a DP steel." *Fundamentals of DP steels*, The metallurgical society of AIME, 347-381.
97. Tomota, Y., Kuroki, K., Mori, T., Tamura, I. (1976): "Tensile deformation of two-ductile-phase alloys: flow curves of alpha-gamma Fe-Cr-Ni alloys." *Materials Science and Engineering*, 24, 85-94.
98. Speich, G.R., Miller, R.L. (1979): "Mechanical properties of ferrite-martensite steels." *Structure and properties of DP steels*, The Metallurgical Society of AIME, Warrendale, Pennsylvania, 145-182.
99. Marder, A. R. (1982): "Deformation characteristics of DP steels." *Metall. Trans.*, 13A, 85-92.

## **APPENDIX A**

### **EFFECTIVE STRAIN CALCULATION**

In order to evaluate and predict the maximum strain of a bent tube, it is necessary to derive the equations of the effective strain. It can be assumed that a state of plane stress exists in a thin-walled tube. In addition, in terms of the measurement value after bending, hoop strain ( $\epsilon_2$ ) is much less than axial strain ( $\epsilon_1$ ) and thickness strain ( $\epsilon_3$ ). Therefore, hoop strain of bent tube is assumed to be neglected for calculating effective strain. The strain and stress state of a bent tube is shown in Figure A1.



Figure A1: Strain and stress state in a tube bending

In terms of the assumed stress and strain state in bending tube:

$$\varepsilon_2 = 0, \sigma_3 = 0$$

According to Hencky – Iliushin deformation theory, the strain and stress relationship is established:

$$\varepsilon_1 = \frac{\varepsilon_e}{\sigma_e} \left( \sigma_1 - \frac{1}{2} \sigma_2 \right) \quad (\text{A-1})$$

$$\varepsilon_2 = \frac{\varepsilon_e}{\sigma_e} \left( \sigma_2 - \frac{1}{2} \sigma_1 \right) \quad (\text{A-2})$$

Substituting  $\varepsilon_2 = 0$  into equations A-2:

$$\sigma_2 = \frac{1}{2} \sigma_1 \quad (\text{A-3})$$

Hence the effective stress is:

$$\sigma_e = \sqrt{\sigma_1^2 - \sigma_1 \sigma_2 + \sigma_2^2} = \frac{\sqrt{3}}{2} \sigma_1 \quad (\text{A-4})$$

Since the volume remains constant:

$$\varepsilon_1 + \varepsilon_2 + \varepsilon_3 = 0 \quad (\text{A-5})$$

Substituting  $\varepsilon_2 = 0$ :

$$\varepsilon_3 = -\varepsilon_1 \quad (\text{A-6})$$

The effective strain is:

$$\varepsilon_e = \frac{2}{\sqrt{3}} \varepsilon_1 \quad (\text{A-7})$$

If the hoop strain  $\varepsilon_2 \neq 0$  is considered, the effective strain can be calculated with the following equation:

$$\varepsilon = \sqrt{\frac{r+1}{2r+1} [(r+1)(\varepsilon_1^2 + \varepsilon_2^2) + 2r\varepsilon_1\varepsilon_2]} \quad (\text{A-8})$$



## VITA AUCTORIS

NAME: Chongzhi Chang  
PLACE OF BIRTH: Baotou, China  
YEAR OF BIRTH: 1974  
EDUCATION: Inner Mongolia Science and  
Technology University, Baotou, China  
1992-1996 B. Eng.  
University of Windsor, Windsor, Canada  
2007-2010 M.A.Sc.